Carrier transport properties in $BaSi_2$ and structure design of $BaSi_2$ solar cells

Deng Tianguo

February 2019

Carrier transport properties in $BaSi_2$ and structure design of $BaSi_2$ solar cells

Deng Tianguo

Doctoral Program in Nano-Science and Nano-Technology

Submitted to the Graduate School of

Pure and Applied Sciences

in Partial Fulfillment of the Requirements

for the Degree of Doctor of Philosophy in

Engineering

at the

University of Tsukuba

Abstract

Thin-film solar cell materials such as CdTe, CIGS, and organic-inorganic perovskite are attracting increasing attention owing to their high energy conversion efficiency η. However, many of these materials contain rare and/or toxic elements. Thus, exploring thin-film solar cell materials that are environmentally friendly is of great significance. Among such materials, we focus on semiconducting barium disilicide $BaSi_2$, owing to its safe, stable, and abundant element and superior fabrication processes. $BaSi_2$ is a new kind of semiconducting material for thin-film solar cell applications, which has a lot of advantages over other solar cell materials. $BaSi_2$ has a suitable band gap E_g of 1.3 eV, matching the solar spectrum, and a high optical absorption coefficient α of 3×10^4 cm^{-1} at 1.5 eV, which is comparable to CIGS. A long minority-carrier lifetime τ of approximately 10 μs results in a large minority-carrier diffusion length L of approximately 10 μm, which is much larger than the grain size of $BaSi_2$ because of inactive grain boundaries. Moreover, $BaSi_2$ can be grown epitaxially both on Si(111) and Si(001) substrates by molecular beam epitaxy due to the small lattice mismatch. The unique feature of $BaSi_2$ is that large α and L can be utilized simultaneously, indicating great potential of $BaSi_2$ as a light absorber layer for thin-film solar cell applications. This thesis aims to clarify the transport properties of electron and hole in $BaSi_2$ films and structure design of $BaSi_2$ solar cells. These results will benefit the future improvement of $BaSi_2$-based solar cells.

There are some investigations devoted to the study of $BaSi_2$ basic electronic and optical properties. However, at the same time, there is almost the lack of information on its transport properties, which is very important for us to get a deeper understanding of $BaSi_2$. Owing to this reason, temperature dependence of electron mobility in undoped n-$BaSi_2$ and hole mobility in B-doped p-$BaSi_2$ have been systematically studied both experimentally and theoretically. The experimentally obtained temperature dependence of electron mobility in the range of 160−300 K was found to have a maximum value of 1230 cm^2/Vs at 218 K, while it dropped down to 816 cm^2/Vs at room temperature RT. This behavior is determined by the delicate balance between intergrain boundary scattering and scattering on the phonons, the latter defines the high temperature part. The value of 816 cm^2/Vs at RT is larger than in the other semiconducting silicides. The analysis of the experimental temperature dependence of the mobility in the $BaSi_2$ films shows that the hole mobility in p-$BaSi_2$ at RT is about one order or four times smaller with respect to the electron mobility in n-$BaSi_2$. The hole mobility versus temperature behavior is mainly defined by scattering on phonons and partly by scattering on neutral impurity centers. For device applications, where higher hole mobility values are desirable, we can suggest using $BaSi_2$ grown on Si(001) substrates rather than Si(111) ones.

We have achieved p-$BaSi_2$/n-Si heterojunction solar cells on Si(111) substrate, wherein photogenerated carriers can be separated effectively according to the band alignment. Associated with the result that p-$BaSi_2$ films on Si(001) possess better transport properties than that on Si(111), so we try to use Si(001) substrate to explore the potential of p-$BaSi_2$/n-Si(001) heterojunction solar cells. Meanwhile, Si(001) substrates are far more abundant than Si(111) ones. To attain the favorable features of Si(001) substrates, we first adopted a textured Si(001) substrate with {111} facets to server for p-$BaSi_2$/n-Si(001) heterojunction solar cells. The reflectance of $BaSi_2$ on the textured substrate was lower than that on the flat substrate, indicating that light-trapping took place. After confirming this, p-$BaSi_2$/n-Si heterojunction solar cells were fabricated with varying $BaSi_2$ layer thickness d and hole concentration p. These cells exhibited a maximum η of 4.6% with an open-circuit voltage V_{OC} of 0.3 V and a short-circuit current density J_{SC} of 27.6 mA/cm^2 when the p-$BaSi_2$ layer was 75 nm-thick. The values of V_{OC} and J_{SC} were approximately half of those observed for the devices fabricated on the flat Si(111) substrate, which indicated that the $BaSi_2$/Si interfaces was defective. By

performing the high-resolution transmission electron microscopy, dislocations were observed, which may form defective centers for minority-carriers. So improved etching technique will be necessary to avoid such defects.

Next, we used a flat n-Si(001) substrate to investigate the potential of Si(001) substrates for the p-$BaSi_2$/n-Si heterojunction solar cells because of recent achievements in systems of $BaSi_2$ on Si(001). We examined the influence of d and p on the solar cells properties. The p-$BaSi_2$ films were found to be under compressive strain in the normal direction and compressive stress in the in-plane direction when d < 60 nm. The η reached a maximum value of 9.8% with a J_{SC} of 37.0 mA/cm^2, a V_{OC} of 0.44V, and a FF of 59.7% with d = 40 nm and a p of 1.1×10^{18} cm^{-3} for p-$BaSi_2$. These values were comparable to those obtained for devices fabricated on Si(111), indicating that Si(001) substrates can also be used for $BaSi_2$ solar cells.

Our goal is the fabrication of high-η $BaSi_2$/c-Si tandem solar cells. Prior to the formation of a $BaSi_2$/c-Si tandem solar cell, we aimed to form a p^+-$BaSi_2$/p^+-Si tunnel junction (TJ), which is necessary to make the electrical contact between $BaSi_2$ and c-Si solar cells sufficiently small. The tunnel properties of the p^+-$BaSi_2$/p^+-Si junction were confirmed, and the tunnel current density reached 18.3 A/cm^2 at a V_{bias} = 1.0 V, indicating a sufficient small tunnel resistance. Large photoresponsivity reaching 0.35 A/W at 850 nm at V_{bias} = 1.0 V, which corresponds to an EQE value of 54%, show great promise of $BaSi_2$ on TJ for use in $BaSi_2$-homojunction and Si-based tandem solar cells.

As device simulation software helps us understand and depict the physical processes, and make reliable predictions of the device behavior. In order to explore the potential of $BaSi_2$ for solar cell applications, n^+pp^+-$BaSi_2$ homojunction and BaC_xSi_{2-x}/c-Si tandem solar cells were proposed and simulated using a 2-dimensional Silvaco Atlas simulation package. We first present the architecture of the solar cells, afterwards, set the d of p-$BaSi_2$ light absorber in a homojunction structure between 0.2 and 10 μm to investigate its effect on the solar cell performance. The η almost saturated when $d \geq 2$ μm, with a value of 23.3%. When the E_g of BaC_xSi_{2-x} was increased up to 1.7 eV, the tandem solar cell showed a maximum η of 30.3% with a large V_{OC} of 1.94 V.

Table of Contents

Abstract ..... **I**

Chapter 1 Introduction **1**

1.1 Introduction of solar cells **1**

1.1.1 Application of solar cells 1

1.1.2 Solar cell conversion efficiency 2

1.1.3 Solar cell materials 3

1.2 Introduction of $BaSi_2$ **8**

1.2.1 Fundamental properties of $BaSi_2$ 8

1.2.2 Growth methods of $BaSi_2$ 12

1.2.3 Research progress of $BaSi_2$-based solar cells 14

1.3 Aim of this thesis **16**

Chapter 2 Transport properties of $BaSi_2$ **19**

2.1 Scattering mechanisms in semiconductors **19**

2.2 Experiments **20**

2.3 Results and discussions **21**

2.4 Calculation **26**

2.4.1 Calculation of the electron mobility in n-$BaSi_2$ films 27

2.4.2 Calculation of the hole mobility in p-$BaSi_2$ films 29

2.5 Conclusion **33**

Chapter 3 p-$BaSi_2$/n-Si solar cells on textured n-Si(001) with a pyramid structure consisting of {111} facets **35**

3.1 Influence of textured structure **35**

3.2 Experiments **36**

3.3 Results and discussions **37**

3.4 Conclusion **42**

Chapter 4 p-$BaSi_2$/n-Si solar cells on flat n-Si(001) substrate **45**

4.1 Background **45**

4.2 Experiments **45**

4.3 Results and discussions **46**

4.4 Conclusion **52**

Chapter 5 Characterization of $BaSi_2$ films on a p^+-$BaSi_2$/p^+-Si tunnel junction **53**

5.1 Background **53**

5.2 Experiments **53**

5.3 Results and discussions **54**

5.4 Conclusion **59**

Chapter 6 Simulation of $BaSi_2$-based homojunction and tandem solar cells **61**

6.1 Background **61**

6.2 Introduction to Silvaco-Atlas **62**

6.3 Simulation method **63**
6.4 Results and discussion **65**
6.4.1 Top-cell simulation 65
6.4.2 Bottom-cell simulation 68
6.4.3 Tandem-cell simulation 68
6.5 Conclusion **71**
Chapter 7 Summaries **73**
Appendix A. Input codes for simulating $BaSi_2$-based solar cells **75**
Appendix B. Correspondence table between sample number and sample name. **82**
References **83**
Acknowledge **89**
Award **91**
List of publications **93**
List of conferences **95**

Chapter 1 Introduction

1.1 Introduction of solar cells

1.1.1 Application of solar cells

To meet the continuous increase of human's energy demand, exploring renewable energy sources, such as solar, wind, biomass, hydropower, tides, and geothermal energies, alternative to commonly used fossil fuels, is of great importance.[1] Fossil fuels not only constitute a limited energy source, but are also the main reason of increased air pollution and global warming. Photovoltaic (PV) technology, which is known for converting solar energy into electricity through a semiconducting material, plays a key component of decarbonizing electricity.

The first solar cell, which was created by Charles Fritts in 1883, achieved a power conversion efficiency η of 1–2% by covering selenium with a thin layer of gold. In 1954, physicists at Bell Laboratories discovered that crystalline silicon c-Si is more efficient than selenium, and created the first practical solar cell with improved η of 6%.[2] This discovery led to solar cells capable of powering electrical equipment. After that, the PV market is rapidly increasing, especially in recent years. Figure 1.1 presents the global installed capacity of solar PV system from 2007 to 2017. In 2017, the total PV global capacity increased to over 400 GW, rose by almost 33% compared with the year 2016. The market expansion was mainly due to the increasing competitiveness of solar PV combined with the rising demand for electricity in developing countries, as well as to the increasing awareness of solar PV's potential to alleviate pollution, reduce CO_2 emissions and provide energy access.[3]

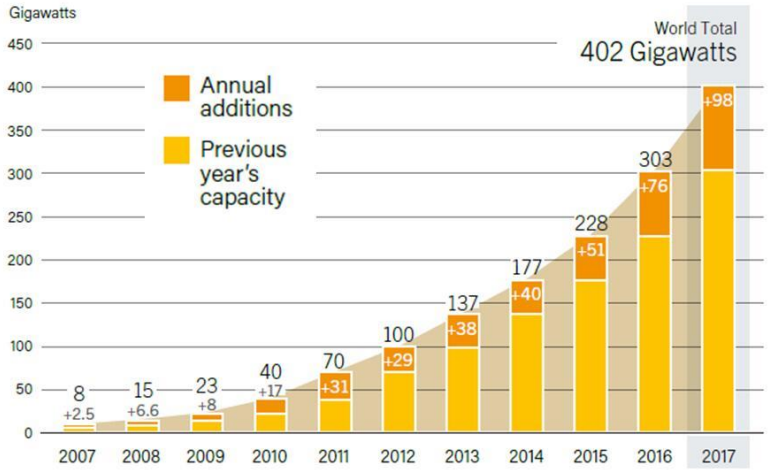

Fig. 1.1 Global renewable power capacity, 2007-2017.[3]

Si PV modules, consisting of monocrystalline silicon (mono-Si) and polycrystalline silicon (poly-Si) technologies, share over 90% of the total commercial market from the satellites to the resident families. The rest of the market are composed of the third generation PV technologies which use advanced thin-film solar cells modules including cadmium-telluride (CdTe) modules, amorphous Silicon (a-Si) modules, and copper indium gallium selenide sulfide $Cu(In,Ga)(S,Se)_2$ (CIGS) modules.[4] They produce a relatively high-η for a low cost compared to other solar technologies. However, some of them consist of toxic and/or rare elements.

So exploring environmental friendly light absorber materials is very essential. There are many researches in the field of solar PVs in universities, companies, and research agencies all over the world, who focus on making current technology PVs cheaper and more efficient, developing new technologies based on new solar cell architectural designs, and exploring new materials for light absorbing.

1.1.2 Solar cell conversion efficiency

Solar cell efficiency refers to the portion of energy in the form of sunlight that can be converted via PVs into electricity. The η of a solar cell is considered the most important criterion when assessing a solar cell's quality. The most efficient commercially available solar PV module on the market has an η of 22.5%, whereas the majority are from 15% to 17% efficiency rating. Most relevant for solar energy conversion is the terrestrial solar spectral irradiance on the surface that differs from the extraterrestrial irradiation (AM0) due to the effect of filtering by the atmosphere. Air Mass 1.5 Global (AM1.5G) describes the radiation arriving at earth's surface after passing through 1.5 times a standard air mass, with the sun at 48.2° from zenith with integrated power density of 100 mW/cm^2, including both direct and diffuse radiation. This is the power density that is usually referred to as "one sun". The AM also depends on the position of the sun and can be defined as follows:

$$\mathrm{AM} = \frac{1}{\cos(\theta)} \tag{1.1}$$

where θ is the elevation angle of the Sun as shown in Fig. 1.2.[5] AM1.5G is used as the standard spectral distribution of light to measure a solar cell's efficiency. Generally, 99% of the light that reaches the Earth's surface is at wavelengths of less than 2500 nm in the AM1.5G spectrum, and 88% is less than 1350 nm. To be efficient, a solar cell should be able to absorb the largest number of photons possible. Figure 1.3 compares the AM0 and AM1.5G spectra.[6]

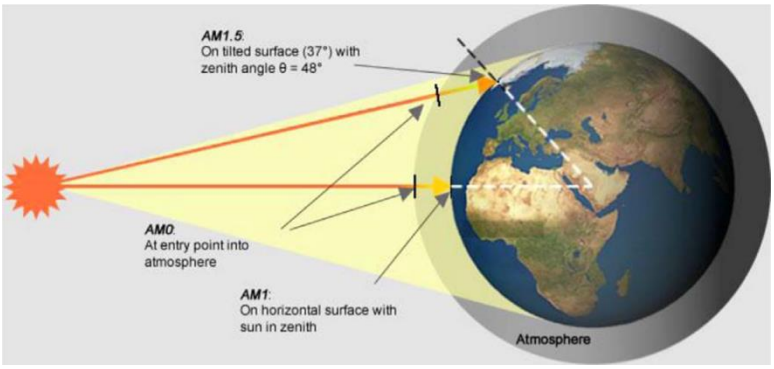

Fig. 1.2 Illustration of the air mass concept.[6]

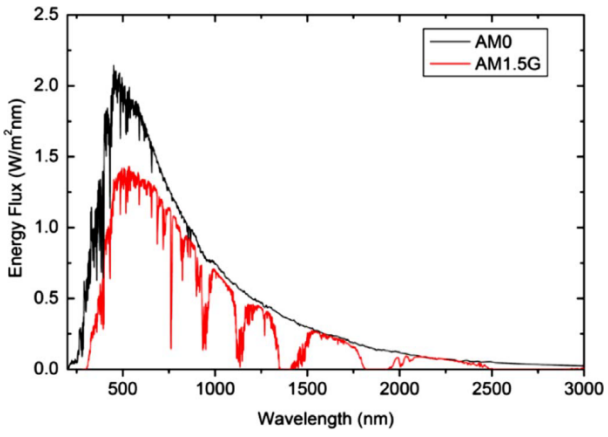

Fig. 1.3 AM0 and AM1.5G solar irradiance spectra.

Figure 1.4 shows recent best research-cell efficiencies in the world, measured under standard AM1.5G illumination, which is summarized by national renewable energy laboratory (NREL). Single gallium arsenide (GaAs) junction solar cells (η = 28.9%) are approaching the theoretical limiting power efficiency of 33.7%, noted as the Shockley-Queisser limit.[7] The maximum η of single c-Si solar cells is 27.6% with concentrated area. As for thin-film solar cells, CIGS solar cells reach a maximum η of 23.3%, showing great potential compared with c-Si solar cells. Besides, organic-inorganic hybrid perovskite $CH_3NH_3PbI_3$ solar cell is a rising star in solar cell family. Its efficiency increased dramatically from 3.8% to 23.3% in a few years, catching up with CIGS solar cells.

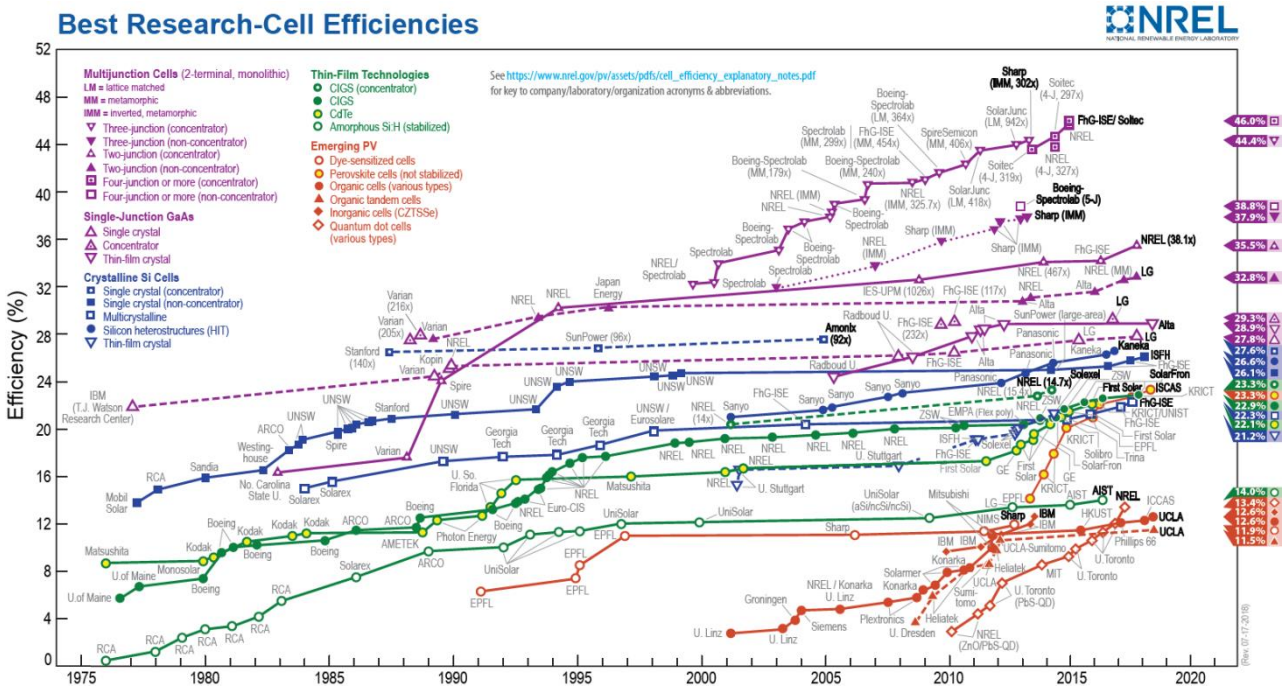

Fig. 1.4 Recent best research-cell efficiencies in the world.

1.1.3 Solar cell materials

Many solar cell materials show varying efficiencies and costs. Materials that are widely investigated for solar cell applications include silicon (mono-Si, and poly-Si), CdTe, CIGS, a-Si, GaAs, perovskite, and organic materials. Each of them has its own merits, so it is important to make their properties clear.

a) c-Si solar cells

c-Si has an indirect band gap of 1.12 eV with an absorption coefficient (α) of ~ 10^3 cm^{-1} at 1.5 eV.[8] The minority-carrier diffusion length (L) is over 100 μm in intrinsic Si wafer. Since the first c-Si panel was created in 1954 with an η of 6%, it became the most popular material for solar cell applications. According to the type of wafer, it can be divided into mono-Si and poly-Si solar cells. Mono-Si is often made through Czochralski process, and the solar cells possess higher efficiency associated with higher cost. Poly-Si is made from cast square ingots, which are made from large molten silicon with carefully cooled and solidified. Poly-Si solar cells are cheaper than mono-Si solar cells, but less efficient.

As shown in Fig. 1.5, the structure of c-Si solar cells developed from simple Si-homojunction to more efficient structures such as tunnel oxide passivated contact (TOPCon), interdigitated back contact (IBC), interdigitated back contact silicon heterojunction (IBC-SHJ), and passivated emitter and rear cell (PERC). Recently, an η of 26.3% IBC-SHJ c-Si solar cell was obtained by Kaneka corporation, Japan.[9] In this structure, Si heterojunctions rather than homojunctions at back side were used for effectively extracting

photogenerated carriers. Meanwhile, carrier recombination was maximally avoided and minority-carrier lifetime (τ) of Si wafer was preserved. This result confirms strong potential of silicon PVs to exceed 27%.[10]

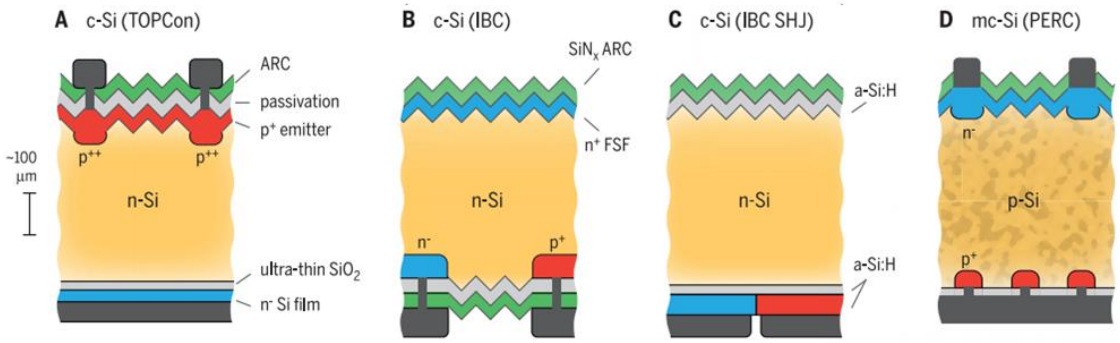

Fig 1.5. Structures of (A) TOPCon c-Si, (B) IBC c-Si, (C) IBC-SHJ c-Si, and (D) PERC mc-Si solar cells.[10]

b) CdTe solar cells

CdTe is a binary semiconductor with a cubic zinc blende crystal structure and a near-ideal E_g of 1.43 eV that the steep absorption coefficient versus energy enables very good light collection.[11] It is a stable compound material that can be produced from a wide variety of methods, including evaporation, sputtering, closed-space sublimation and so on. A thin-film of CdTe is adequate for producing high efficiency cells if both bulk and surface recombination are curbed. The structure of a conventional CdTe solar cell is shown in Fig. 1.6. Cells are typically grown in a superstrate configuration starting from a glass substrate coated with fluorine-doped tin oxide (FTO). The subsequent layer stack usually consists of chemical bath deposited cadmium sulfide (CdS), followed by evaporated 2–3 µm-thick CdTe and a metal back contact such as Al or Ti, in some cases with a copper zinc telluride (CuZnTe) interfacial layer between the metal and the CdTe.

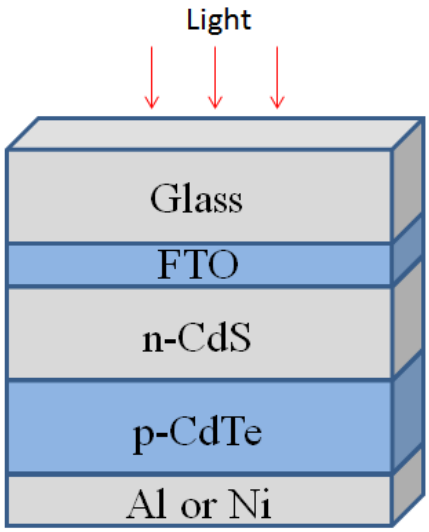

Fig. 1.6 Typical structure of a CdTe solar cell.

The first significant laboratory CdTe solar cell was reported in 1972 by Bonnet and Rabnehorst who developed a thin-film graded gap CdTe-CdS p-n heterojunction solar cell with 6% efficiency. This cell was

created in a three-step process including high temperature vapor phase deposition of CdTe and high vacuum evaporation of CdS.[12] By inserting a cadmium sulfur telluride (CdSTe) film between CdTe and metal contact and controlling the growth condition of CdTe films with an effective acceptor doping concentration of 10^{17} cm^{-3}, the interface recombination velocity was significantly minimized. In 2016, the highest reported certified efficiency for CdTe reached 22.1%, fabricated by First Solar Inc.[13,14]

CdTe solar panel is the first thin-film PV technology to exceed c-Si PVs in cheapness. There are some advantages over conventional c-Si technology, including an ideal band gap for light absorbing and easier fabrication process on glass. CdTe absorbs light close to the ideal wavelength, capturing energy at shorter wavelength. And the α of CdTe is greater than c-Si. CdTe solar panel can be fabricated through a continuous manufacturing process, creating a complete solar module in less than 2.5 h. Certainly, attention should be paid to its drawbacks. CdTe solar cells have comparatively low open-circuit voltage (V_{OC}) (maximum of 0.9 V) compared with its band gap. Recombination losses in the crystal grains and at the interfaces result in high voltage loss of about 37%.[15] In addition, the use of the toxic element Cd and the scarcity of Te is also a concern. So recycling systems should be set up for commercial CdTe modules.

c) CIGS solar cells

CIGS is a compound semiconductor with a chalcopyrite structure and tunable band gaps between 1.0 to 2.4 eV by varying the In/Ga and Se/S ratios. The adjustable E_g of 1.4~1.6 eV is suitable for light absorbing. CIGS is one of the three mainstream thin-film PV technologies associated with CdTe, and a-Si PVs. The direct E_g and the large α reaching about 10^4 cm^{-1} at 1.5 eV make it much thinner for solar cell applications compared with c-Si solar cells.[16] So it is thin enough to be flexible, allowing it to be deposited on flexible substrates. The other attractive feature is that the polycrystalline films of CIGS have the same optical properties with the single crystal ones, and higher η can be obtained, where grain boundaries (GBs) are self-passivated by considering the segregation of an insulating material that prevents the recombination of the photogenerated carriers in CIGS.[17] In general, GBs act as recombination centers for polycrystalline materials, however, the recombination of minority-carriers at the GBs in CIGS is not strong.[18] This property makes the voltage loss of 16% for record-CIGS solar cell which is the minimum among various solar cells.

An η of 4.5% was achieved for the first thin-film CIGS solar cells by L. Kazmerski.[19] The structure is given in Fig. 1.7. Polycrystalline CIGS films were formed by sputtering or evaporation from the constituent elements and were typically deposited onto a molybdenum (Mo) film which was sputtered on a soda lime glass substrate. The typical active layer thickness d was about 2–3 μm. Sodium diffusing from the glass substrate into the CIGS layer has been found to play a key role in passivating defects in the CIGS layer.[20] Then it was covered by a chemical-bath deposition of CdS film to form a heterojunction, followed by an intrinsic ZnO buffer layer, and a transparent ZnO:Al conducting layer. In some recent high-η devices, the CdS layer was replaced by the more transparent ZnO_xS_{1-x} layer.[21] The record η has steadily increased over the past decade, with the present record value of 22.9%.[22]

The tunable band gap makes CIGS an interesting candidate for tandem solar cells, acting as top-cell in CIGS/c-Si tandem solar cell or bottom-cell in perovskite/CIGS tandem solar cells.[23,24] However, large band gap (Ga-rich) CIGS solar cells have not yielded sufficient efficiency for a CIGS/Si tandem solar cell to beat the record c-Si solar cell. The composition of rare metals In and Ga limits the utilization of CIGS. And substituting In and Ga by abundant Zn and Sn, respectively, for $Cu(Zn,Sn)(S,Se)_2$ (CZTS) solar cells is a hot research topic with the highest η of 12.6%.[25]

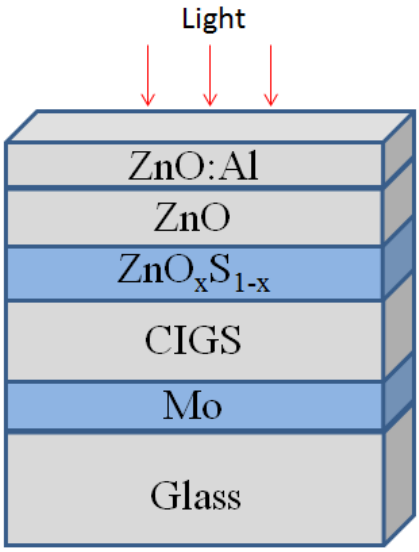

Fig. 1.7 Typical structure of a CIGS solar cell.

d) a-Si solar cells

An a-Si solar cell is made of amorphous or microcrystalline Si and its basic electronic structure is the p-i-n junction. One of the attractive features of a-Si is that it has a direct E_g with a value of 1.7 eV, which allows a significant fraction of sunlight to be absorbed within a thin layer of a few micrometers.[11] One disadvantage of a-Si is the short orders and the dangling bonds, which result in short L, limiting the performance of solar cell. The role of hydrogen in reducing dangling bonds by several orders of magnitude was verified by W. Paul in 1980s.[26] Due to the improved properties of a-Si:H, it is widely used for solar cells.

The first a-Si:H solar cell, with an η of 2.4%, was fabricated by Clarlson and Wronski in 1976 at RCA laboratory.[27] After introducing a-Si:H and light trapping features, the achievement of 9.3% efficiency was confirmed in 1982.[28] In the early of 1990s, researchers placed efforts on the development of multi-junction cells and modules, that solar spectrum can be used as much as possible. The most successful one for a-Si solar cells is the heterojunction with intrinsic thin-layer (HIT) solar cell fabricated by Sanyo Electric Co., Ltd, with an η of 25.6%. Figure 1.8 shows the structure of HIT solar cells. An intrinsic a-Si layer, a doped a-Si layer, and a TCO layer are deposited on both sides of a mono-Si substrate. After that, metal grid electrodes are fabricated using a screen printing method on both sides of the doped a-Si layer. By inserting the high-quality intrinsic a-Si layer, the defects on the c-Si surface can be effectively passivated, resulting in a low voltage loss.

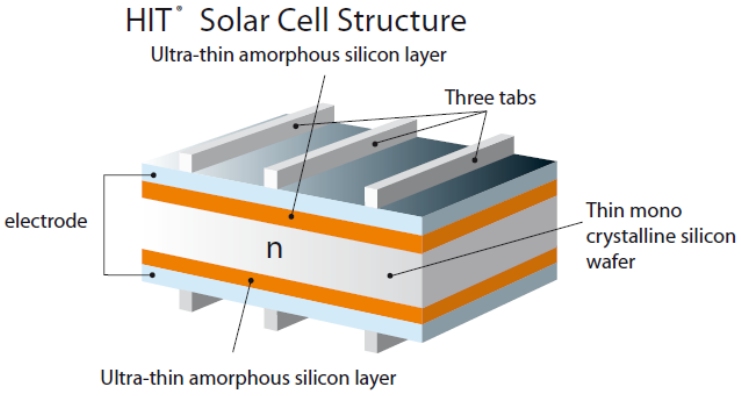

Fig. 1.8 Structure of HIT solar cells made by Sanyo.

e) GaAs solar cells

GaAs has a small charge carrier effective mass and a direct E_g of 1.42 eV, close to the optimum value for solar cell applications. Because of the large α, the cell thickness can be kept relatively small (~2 μm) to harvest the solar spectrum up to the band gap.[29] The wide E_g and low-defect crystal structure also result in a lower leakage current and more rapid voltage buildup under illumination.[30]

The first known operational use of GaAs solar cells in space was for the Venera 3 mission, launched in 1965. The GaAs solar cells, manufactured by Kvant, were chosen because of their higher performance in high temperature environments. New technologies have led to improvements in the solar cell structure parameters. In the 1990s, GaAs solar cells took over from c-Si as the cell type most commonly used for photovoltaic arrays for satellite applications. Later, dual- and triple-junction solar cells based on GaAs with germanium and indium gallium phosphide layers were developed as the basis of a triple-junction solar cell, which held a record η of over 32% and can operate also with light as concentrated as 2,000 suns.[31] The record η of 28.9% for a single-junction solar cell under standard AM1.5G illumination has been achieved, with a n-GaAs/p-$Al_{0.3}Ga_{0.7}As$ junction geometry with large-E_g window layers that serve to retain minority carriers in the GaAs active layer as shown in Fig. 1.9.[10,14] The GaAs heterostructure is epitaxially grown using chemical vapor deposition (CVD), which is a relatively energy-intensive process. The V_{OC} of the record-efficiency cell is very high.[10]

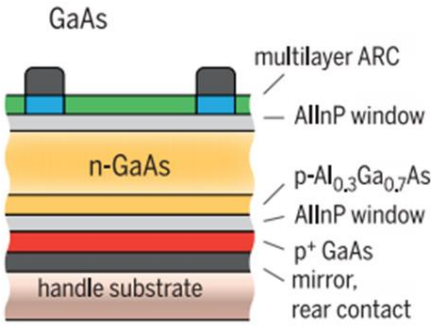

Fig. 1.9 Structure of state-of-the-art GaAs solar cells.[10]

Whereas III-V solar cells have traditionally been used in niche markets requiring high efficiency on a small area, such as space technology, the newly developed layer-transfer technology enables fabrication of large-area flexible GaAs technology at reduced cost for a much broader range of applications. Encapsulation and recycling of commercial GaAs modules is very important because of the use of the toxic element As.[32]

f) Perovskite solar cells

Perovskite solar cell is a rising star in PV family and it is a type of solar cell including a perovskite structured compound, most commonly a hybrid organic-inorganic lead halide-based material, as the light-harvesting active layer.[33] These materials have the general formula ABX_3, where A is an organic cation (most often methylammonium, CH_3NH_3), B is an inorganic cation (usually Pb), and X is a halide (typically I, often with a small fraction of Cl or Br: $CH_3NH_3Pb(I,Cl,Br)_3$). Depending on the halide used, the band gap can be continuously tuned from 1.5 eV (pure I) to 3.2 eV (pure Cl), with the smaller-E_g materials providing better solar cell efficiencies.[10] This material also displays a diffusion length for both holes and electrons of over 1 μm.[34] The long diffusion length means that these materials can function effectively in a thin-film structure, and that charges can transport in the perovskite itself over long distances. It has recently been reported that charges are predominantly present as free electrons and holes, rather than as bound excitons, since the exciton

binding energy is low enough to enable charge separation at room temperature (RT).[35,36]

First attempt of perovskite solar cell led to an η of 3.8% with a thin layer of perovskite on mesoporous TiO_2 as electron-collector.[37] Because a liquid corrosive electrolyte was used, the cell was only stable for a matter of minutes. Park *et al.* improved upon this in 2011, using the same dye-sensitized concept, achieving an η of 6.5%.[38] In 2017, Seok *et al.* showed that the introduction of additional iodide ions into the organic cation solution, which is used to form the perovskite layers through an intramolecular exchanging process, decreases the concentration of deep-level defects. The defect-engineered thin perovskite layers enable the fabrication of perovskite solar cells with a certified η of 22.1% in small cells and 19.7% in 1 cm^2 cells.[39]

Despite their excellent performance, perovskite solar cells are known to degrade within a few hours to days under standard operating conditions. At present this is the greatest obstacle for commercial applications. Besides, measurements of the current-voltage characteristics can suffer from hysteresis, making efficiency analysis complex. The origin of this hysteresis is still unclear, but the leading hypothesis involves ion or vacancy migration under operating conditions.[40] The perovskite salts are partially soluble in water, so the cells are sensitive to humidity. Because of Pb toxicity, encapsulation and recycling is important for this technology to become viable for large-scale application. The toxicity challenge is greater for this material than for CdTe and GaAs because the much higher water solubility and lower vaporization temperature make environmental exposure during module encapsulation failure more dangerous.[41]

1.2 Introduction of $BaSi_2$

1.2.1 Fundamental properties of $BaSi_2$

As discussed above, although c-Si PV technology is dominant in PV market, thin-film solar cells are gradually increasing their share in recent years. However, the application of CdTe and CIGS is limited due to the toxic and/or rare elements associated with the high cost and poor long-term stability. So exploring suitable material for thin-film solar cells is very important.

In this thesis, we focus on orthorhombic semiconducting material barium disilicide ($BaSi_2$), which possesses a lot of advantages over other materials. $BaSi_2$ has an orthorhombic structure as shown in Fig. 1.10, which contains 16 Si atoms and 8 barium atoms, and every 4 Si atoms compose to a small tetrahedral structure. The length of three axis are 0.892 nm, 0.680 nm, 1.158 nm, respectively. It is composed with earth abundant elements Ba and Si, making the cost of $BaSi_2$ cheaper than CIGS and CdTe. The band structure of $BaSi_2$ is shown in Fig. 1.11 (a). $BaSi_2$ has an indirect band gap and both large E_g and L can be expected due to its unique band structure.[42] The atomically resolved and orbital projected density of states (DOS) of $BaSi_2$ is displayed in Fig. 1.11 (b).[42] The valance band (VB) of $BaSi_2$ is dominated by the Si-p states, which is derived mainly from the Si tetrahedra, whereas the conduction band (CB) mainly consists of localized Ba-d states. One can observe, from the band structure and the DOS, that the topmost VB has a flat energy dispersion. Also, the band curvature of the lowest CB is flat because of the localized Ba-d states. These flat energy dispersions imply high optical activity in $BaSi_2$.[43] The experimental absorption spectrum of $BaSi_2$ was performed using a silicon-on-insulator (SOI) substrate, on which a $BaSi_2$ film was grown. The result is shown in Fig. 1.12, that $BaSi_2$ has a E_g of 1.3 eV and α reaches 3×10^4 cm^{-1} at 1.5 eV, which is roughly 40 times larger than that of c-Si.[44] The ideal E_g for single junction solar cell applications is 1.4 to 1.6 eV. By replacing some Ba atoms with Sr atoms to form $Ba_{1-x}Sr_xSi_2$, the E_g can be enlarged to 1.4 eV.[45] Meanwhile, by substituting part of Si with isoelectric C, the E_g of $BaSi_{2-x}C_x$ can be continuously increased from 1.3 to 3.0 eV.[46] Figures 1.13(a) and 1.13(b) show calculated absorption spectra of several solar cell materials such as $BaSi_2$, Si, CIGS, CZTS and GaAs. The absorption spectrum of $BaSi_2$ rises more steeply than that of the other materials. As a result, $BaSi_2$ has a much stronger absorption than other materials at the same photon energy. Hence, the results

confirm the experimental finding that α of $BaSi_2$ reaches 3×10^4 cm^{-1} at 1.5 eV.[43] According to the calculation based on the absorption spectrum of $BaSi_2$, 95% of the solar spectrum can be absorbed within a 4 μm-thick $BaSi_2$ absorber layer. These results demonstrate that $BaSi_2$ has a large α even though it is an indirect band gap semiconductor.

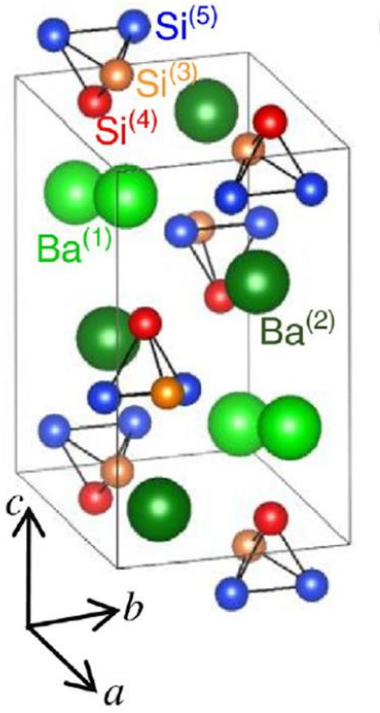

Fig. 1.10 Cell structure of $BaSi_2$.[47]

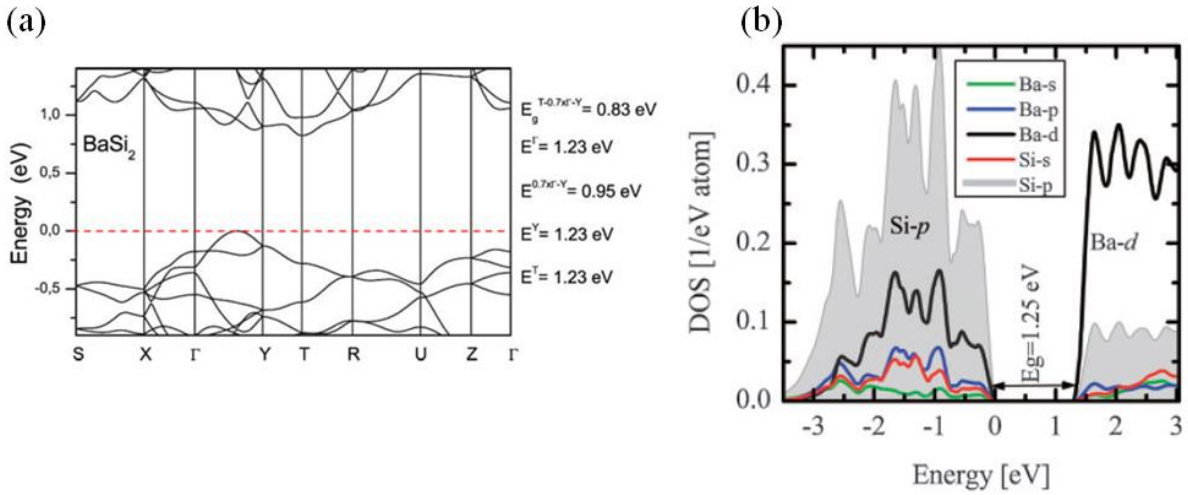

Fig. 1.11 (a) Band structure [42] and (b) atomical resolved and orbital projected DOS of $BaSi_2$.[43]

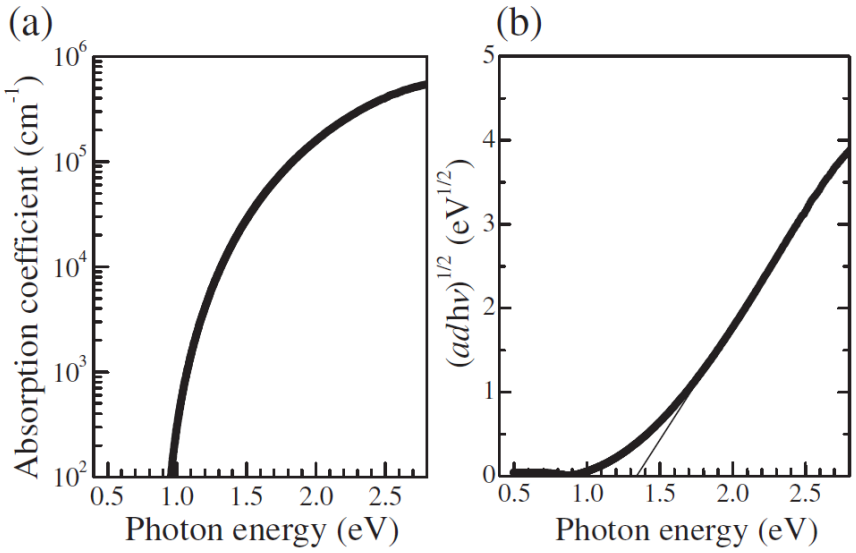

Fig. 1.12 (a) Absorption spectrum and (b) $(\alpha d h\nu)^{1/2}$ versus photon energy plotted for $BaSi_2$.[44]

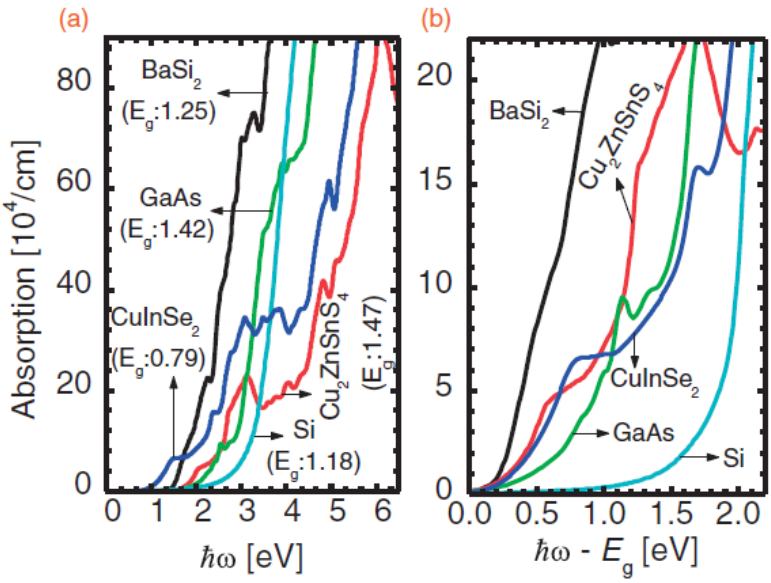

Fig. 1.13 (a) and (b) absorption coefficient of several solar cell materials.[43]

Another promising feature of $BaSi_2$ is its excellent minority carrier properties. For the formation of solar cells, material should have not only suitable E_g and large α, but also large L and τ. Undoped-$BaSi_2$ shows n-type conductivity with an electron concentration (n) of about 10^{16} cm^{-3}. Figures 1.14(a)(b) and 1.14(c)(d) show secondary-electron (SE) and electron beam induced current (EBIC) results, respectively, with acceleration voltage V_{ac} = 5 kV. Front-side Schottky contacts were formed with Al on the $BaSi_2$ surface via wire bonding, and the back-side ohmic contact was made with sputtered Al. In the EBIC method, carriers generated within the diffusion length in the n-type $BaSi_2$ are collected by the electric field under the Al contact and sensed as a current in the external circuit. In Figs. 1.14(c) and 1.14(d), the brighter regions show higher collection of electron-beam-induced carriers in the $BaSi_2$. Figure 1.14(e) shows the EBIC line-scan data along dotted line AA' in Fig. 1.14 (c). The EBIC profile shows an exponential dependence of the distance from the Al contact. The L was roughly estimated to be approximately 10 μm, assuming that the EBIC profile varies as $\exp(-x/L)$, where x is the distance from the Al edge (point A) along the dotted line, and L is the diffusion length

of holes for $BaSi_2$. The obtained L is much larger than the grain size of the $BaSi_2$, implying that the GBs do not work as defect centers for minority carriers in undoped n-$BaSi_2$.[48,49] Moreover, τ of undoped n-$BaSi_2$ was measured using microwave detected photoconductive decay (μ-PCD), where carriers were generated by a 5 ns laser pulse with a wavelength of 349 nm. Photoconductivity decay was monitored by the reflectivity of microwave with the frequency of 26 GHz. High-sensitivity measurement was realized by the differential detection of the reflected microwave intensity between the areas with and without laser irradiation. Then, τ can be calculated by analyzing the photoconductivity decay curves. Figure 1.15 shows film-thickness dependence of lifetime in undoped n-$BaSi_2$. The bulk lifetime is 14 μs, which is long enough for thin-film solar cell applications. Hence, both large L and τ were confirmed in $BaSi_2$, demonstrating its great potential for solar cell applications.[50,51]

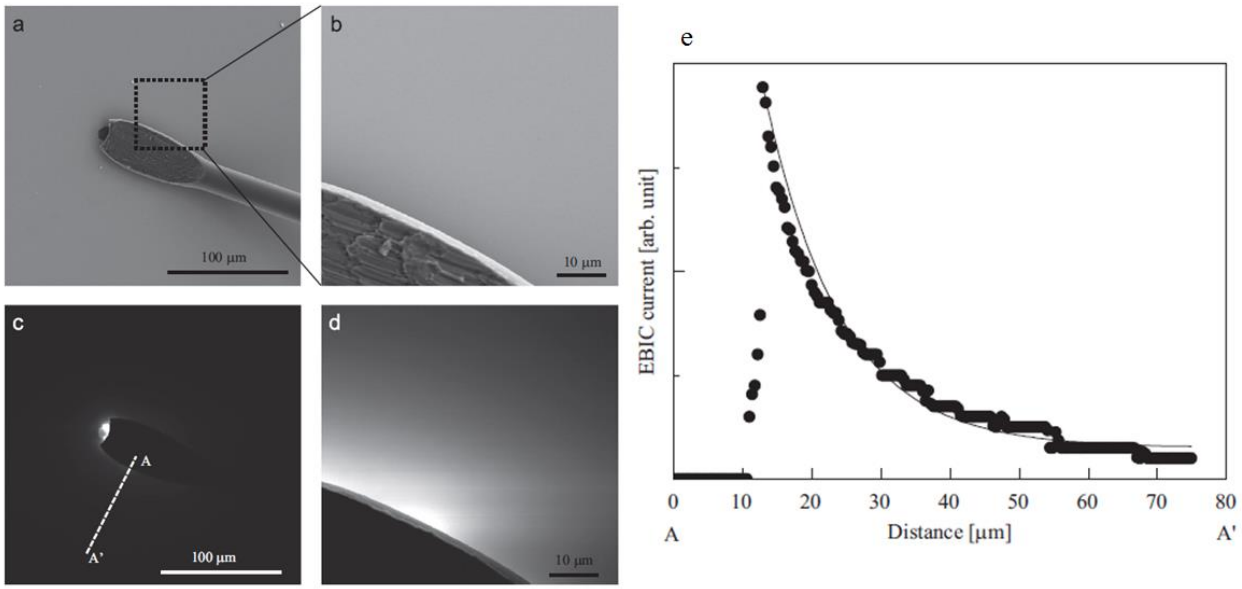

Fig. 1.14 (a), (b) SE and (c), (d) EBIC images around Al contact. (e) EBIC line-scan data along dotted line AA'.[48]

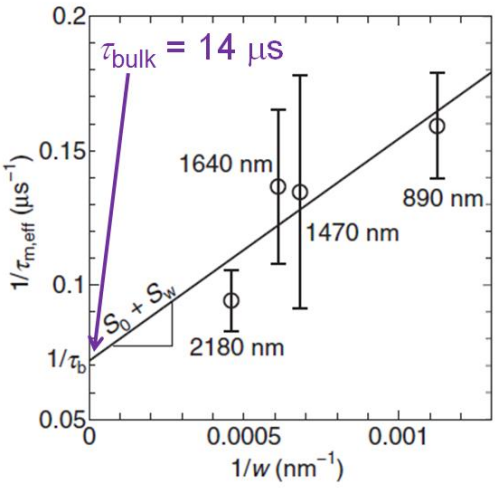

Fig. 1.15 Film-thickness dependence of lifetime in undoped n-$BaSi_2$.[50]

Our goal is the fabrication of high-η $BaSi_2$ homojunction solar cells which consist of a p-n or p-i-n

configuration. So control of the conduction type and carrier concentration is of great importance. The valence band of $BaSi_2$ is mainly composed of Si 3*s*, 3*p* orbital, indicating that Si site is much easier to be substituted than Ba site.[42,52] Based on this result, the conduction type of $BaSi_2$ is similar to that of Si, where p-type can be achieved by group-Ⅲ atoms doping, and n-type can be obtained through group-V atoms doping. Table 1.1 lists the conduction types and carrier concentrations by different dopants in $BaSi_2$. In particular, B-doped $BaSi_2$ shows p-type conductivity, and the hole concentration *p* can be continuously controlled in the range of 10^{16}~10^{20} cm^{-3}. Also, Sb-doped $BaSi_2$ shows n-type conductivity with *n* controlled between 10^{16} and 10^{20} cm^{-3}. Therefore, by utilizing these two dopants, the $BaSi_2$ homojunction diode can be formed.

Table 1.1 Conduction types and carrier concentrations by different dopants in $BaSi_2$.

Dopant	Conduction type	Carrier concentration [cm^{-3}]	Notes	Reference
undoped	n or p	10^{16}	Strongly depend on R_{Ba}/R_{Si}.	[53]
B	p	10^{16}~10^{20}	Continuously control up to p^+.	[54]
Al	p	10^{16}~10^{17}	Diffusion is too strong.	[55]
Ga	n	10^{15}, 10^{20}	Can't be controlled properly.	[56]
In	p	10^{16}~10^{17}	Can't be up to p^+.	[56]
N	p	10^{16}~10^{17}	Plasma source.	[57]
P	n	10^{16}~10^{18}	GaP source.	[58]
As	n	~10^{19}	As ion implantation.	[59]
Sb	n	10^{16}~10^{20}	Continuously control up to n^+.	[60]

1.2.2 Growth methods of $BaSi_2$

There are three main methods for the growth of $BaSi_2$: molecular beam epitaxy (MBE), magnetron sputtering, and vacuum evaporation.

$BaSi_2$ can be grown epitaxially on Si (111) and Si (001) substrates by MBE.[61-64] The growth processes are as follows. First, the Si substrate, which is cleaned by RCA process, is heated to 900 ℃ for thermal cleaning for 30 min so that a very clean Si 7×7 surface reconstruction reflection high-energy electron diffraction (RHEED) patter can be observed. Afterwards, substrate temperature decreases to 500 ℃, and Ba atoms are deposited on the hot Si substrate for reactive deposition epitaxy (RDE) to form a 5 nm-thick $BaSi_2$ template layer. This template layer is used for controlling the crystal orientation of the subsequent $BaSi_2$ epitaxial layers. After RDE, Ba and Si atoms associated with dopants are co-evaporated to the substrate at 500~650 ℃ for MBE growth. Both after RDE and MBE growth, streaky RHEED patterns can be observed, indicating the good surface condition of the epitaxial $BaSi_2$ films. Then, a 3 nm-thick a-Si layer is grown to passivate $BaSi_2$ films. Figures 1.16(a) and 1.16(b) show the epitaxial relationship of $BaSi_2$ on Si(111) and Si(001), respectively. It has a three-fold symmetric domain rotated to 120 °on Si (111), and it forms a twice symmetric domain rotated to 90 °on Si (001). These domains are randomly formed on the Si substrate.[62-64] As a result, $BaSi_2$ is not a uniform film like a single crystal, but epitaxially grown while forming crystal grains. Therefore, there are many GBs in the $BaSi_2$ film as shown in Fig. 1.17, which list electron backscatter diffraction (EBSD) maps of $BaSi_2$ films on Si(111) and Si(001) substrates, respectively. Different from the $BaSi_2$ grown on Si(111) substrate, the grain size of $BaSi_2$ grown on Si(001) substrate seems to be much larger than that on Si(111) substrate.

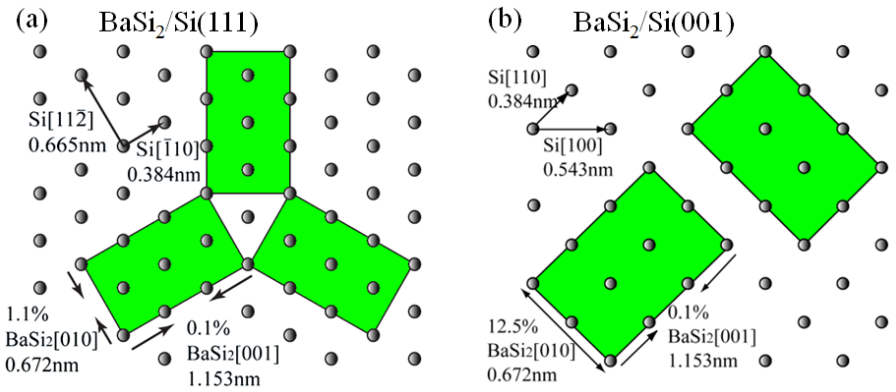

Fig. 1.16 Epitaxial relationship of $BaSi_2$ on (a) Si(111) and (b) Si(001).[63,64]

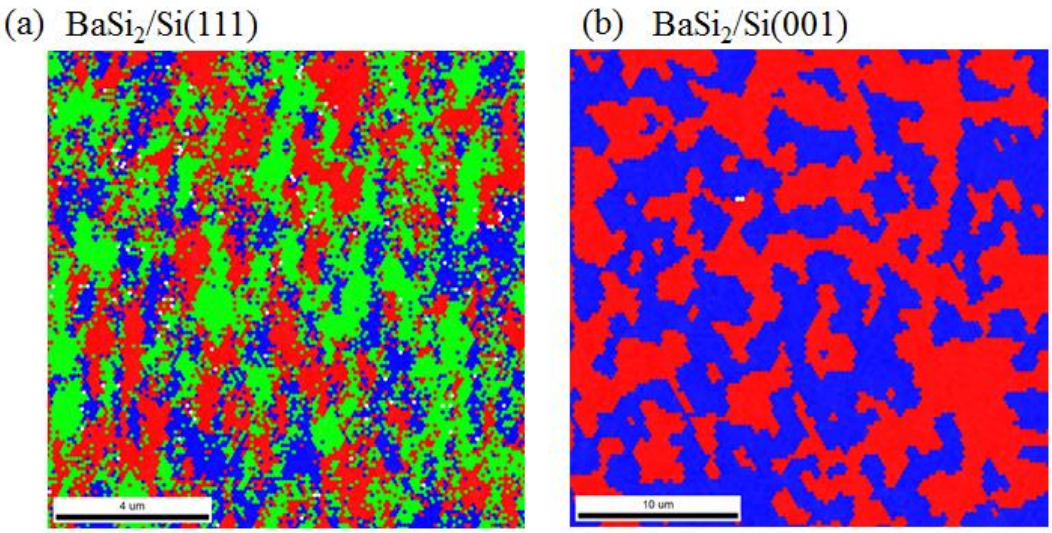

Fig. 1.17 EBSD maps of $BaSi_2$ films on (a) Si(111) and (b) Si(001).[64,65]

Another way to fabricate $BaSi_2$ film is magnetron sputtering, which is a practical method to form large area devices. In 2013, we employed a $BaSi_2$ sputtering target with a diameter of 2 inches, and fabricated 600 nm-thick $BaSi_2$ films by radio-frequency (RF) magnetron sputtering at RT and subsequent post-annealing at 600 ℃ in an ultrahigh vacuum (UHV). However, the photoresponsivity of the $BaSi_2$ film was as small as 0.5 mA/W at a photon energy of 1.5 eV when the bias voltage V_{bias} was 0.5 V, corresponding to an external quantum efficiency (*EQE*) value of approximately 0.08%. The grown layer exhibited n-type conductivity with a large electron concentration of $n = 7 \times 10^{19}$ cm^{-3}.[66] Recently, Matsuno *et al.* formed single phase polycrystalline $BaSi_2$ films on Si(111) by helicon-wave excited plasma (HWP) sputtering, using a stoichiometric $BaSi_2$ target.[67] As the HWP has a higher plasma density, uniform in a large volume,[68] and lower ion energy than those of usual capacitive-coupled plasmas, substrate damage can be greatly reduced. A typical value of $n = 2 \times 10^{16}$ cm^{-3} was obtained at RT. The photoresponsivity rapidly increased for photon energies larger than the band gap of $BaSi_2$, and reached 0.19A/W at a photon energy of 2.0 eV and V_{bias} = −0.5V applied to the indium-tin-oxide (ITO) electrode with respect to the Al electrode. This value was larger by more than two orders of magnitude than that reported previously.[67] However, the crystalline quality of sputtered $BaSi_2$ film is not so good compared with the one grown by MBE.

Vacuum evaporation is another feasible method than MBE. An UHV is not a prerequisite; therefore, the equipment can be simple and inexpensive. Trinh *et al.* used $BaSi_2$ granules to form $BaSi_2$ films by vacuum

evaporation, and achieved a large τ of 4.8 μs in the films grown at 500 °C. Evaporated undoped-$BaSi_2$ films show n-type conductivity with n varies from 10^{17} to 10^{22} cm^{-3} at different substrate temperature. The maximum value of photocurrent was obtained at a photon energy of 1.9 eV, corresponding to an *EQE* of 22% at a reverse applied voltage of 2.0 V.[69] One problem of the evaporated films is cracking due to the mismatch in thermal expansion coefficient between $BaSi_2$ and c-Si. Moreover, the grown films contained metallic phases such as Ba_2Si and Ba_5Si_3.[70,71] In addition, a chemical reaction between the source and boat materials may take place. Both these issues would lead to an inhomogeneous vaporization, and thin-films resulting from such an inhomogeneous vapor are not necessarily comprised of the same compound as the source material. The possible chemical processes during the deposition of $BaSi_2$ on Si by vacuum evaporation using a $BaSi_2$ source are illustrated in Fig. 1.18.[72]

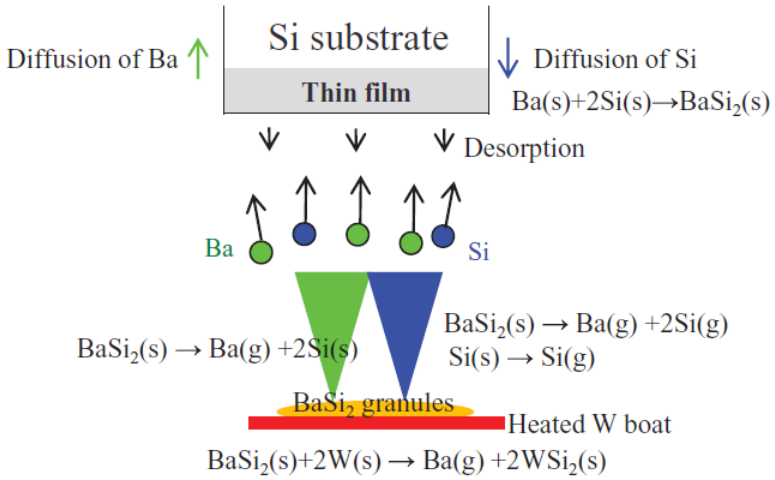

Fig. 1.18 Possible chemical reactions during the deposition process of $BaSi_2$ on Si by vacuum evaporation of $BaSi_2$ granules.[72]

1.2.3 Research progress of $BaSi_2$-based solar cells

The attracting features suggest that $BaSi_2$ is a very promising material for thin-film solar cell applications. $BaSi_2$ can be epitaxially grown on Si substrates and the electron affinity is 3.2 eV,[73] which is about 0.8 eV smaller than that of c-Si (4.05 eV). Design of $BaSi_2$ solar cells on Si and the transport of photogenerated carriers will not be blocked are very important. Some investigations have already been performed towards high efficient $BaSi_2$ solar cells. Here, we discuss about several structures of $BaSi_2$-based solar cells.

(a) n-$BaSi_2$/p-Si heterojunction

Figures 1.19(a) and 1.19(b) show the band alignment of $BaSi_2$ and Si with respect to the vacuum level and Sb-doped n^+-$BaSi_2$ (300 nm, $n = 1 \times 10^{19}$ cm^{-3})/p-Si (resistivity $\rho > 0.1$ Ωcm) diode, respectively. Due to the small electron affinity of $BaSi_2$, band offsets exist at the $BaSi_2$/Si interface, that is, 0.8 eV for CB, and 0.6 eV for VB. These band offsets block the photocurrent flowing across the $BaSi_2$/Si interface. Figures 1.19(c) and 1.19(d) show typical examples of rectifying current–density versus voltage *J–V* characteristics under AM1.5G illumination and internal quantum efficiency (*IQE*) spectrum for the n^+-$BaSi_2$/p-Si diode. A short-circuit current density J_{SC} of 11.8mA/cm^2, V_{OC} = 0.22 V, and η = 1.5% were obtained. These values are much smaller than those obtained in B-doped p-$BaSi_2$/n-Si heterojunction solar cell.[74] This is because the band offsets at the n^+-$BaSi_2$/p-Si interface hinder the transport of photogenerated carriers, promoting the recombination of accumulated electrons and holes via defects at the heterointerface. In Fig. 1.19(d), the *IQE* values were high in the wavelength λ range between 600 and 1200 nm. The λ of approximately 1200 nm is close to the band gap of Si. This means that the *IQE* spectrum was ascribed to the photogenerated carriers originating from the p-Si substrate. On the other hand, the *IQE* was negligibly small at λ < 600 nm, showing that the photogenerated

holes in the 300-nm-thick n^+-$BaSi_2$ did not contribute to the photocurrent.[75,76]

(b) p-$BaSi_2$/n-Si heterojunction

Figure 1.20(a) shows the expected band alignment of a p-$BaSi_2$/n-Si(111) junction diode when p is 2.2×10^{18} cm^{-3} for p-$BaSi_2$ and n is 2.0×10^{15} cm^{-3} for n-Si. Hence, the depletion region stretches into the n-Si region. There is a CB offset $\Delta E_C = 4.05 - 3.2 \approx 0.9$ eV and a VB offset $\Delta E_V = (4.05 + 1.1) - (3.2 + 1.3) \approx 0.7$ eV at the heterointerface. The band offsets ΔE_C and ΔE_V in Fig. 1.20(a) promote the separation of photogenerated electrons and holes in p-$BaSi_2$, as well as those in n-Si, leading to the operation of a solar cell. η of approaching 10% are achieved based on this structure.[74,77] Figure 1.20(b) shows J–V curves of the samples with different p-$BaSi_2$ layer thickness under AM1.5G illumination. All the samples performed as solar cells. This result clearly demonstrates that the p-$BaSi_2$/n-Si heterointerface does not hinder the transport of photogenerated electrons in p-$BaSi_2$ to the n-Si side, and photogenerated holes in n-Si migrate to the p-$BaSi_2$ side, as expected in Fig. 1.20(a). The J_{SC} reaches a maximum of 36.2 mA/cm^2, and V_{OC} increases with the thickness of p-$BaSi_2$ and reaches a maximum of 0.47 V at 20 nm.[78]

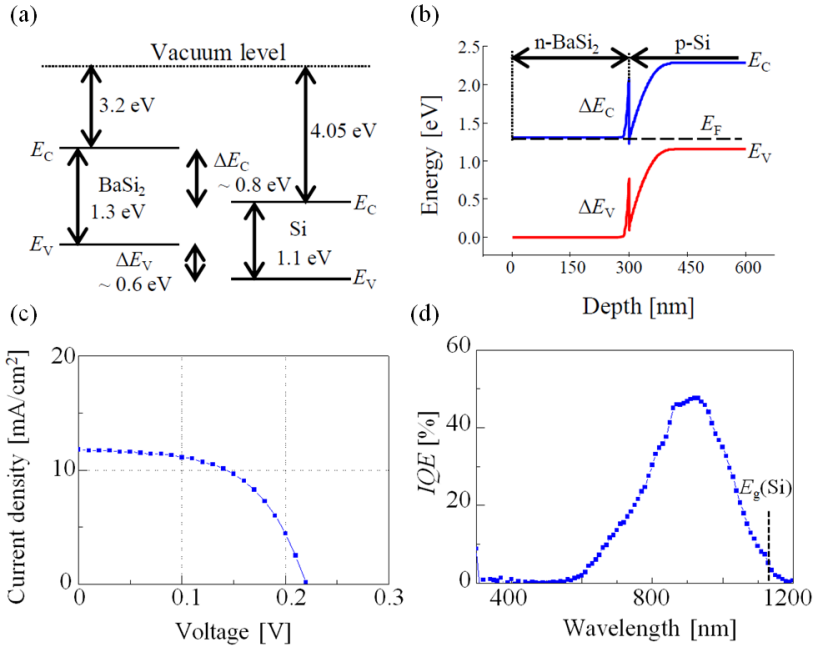

Fig. 1.19 Band alignment of (a) $BaSi_2$ and Si with respect to the vacuum level. (b) n^+-$BaSi_2$/p-Si diode. (c) J–V characteristics under AM1.5G illumination and (d) IQE spectrum for n^+-$BaSi_2$/p-Si diode.[76]

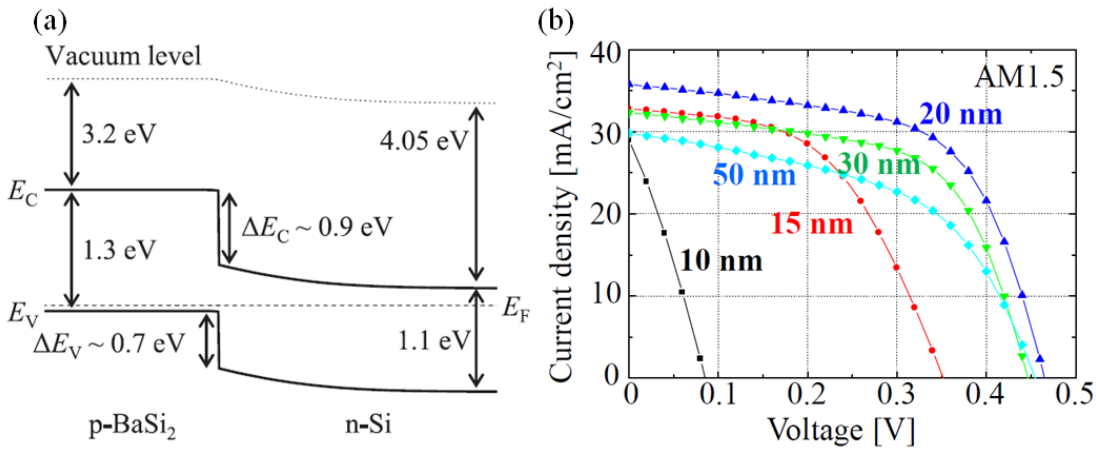

Fig. 1.20 (a) Band alignment and (b) J–V characteristics of p-$BaSi_2$/n-Si heterojunction solar cell.[77,78]

(c) $BaSi_2$ homojunction on a tunnel junction

Due to large conduction and valence band discontinuities at the $BaSi_2$/Si heterointerface, forming a tunnel junction (TJ) is necessary to assist current flow in a $BaSi_2$ pn junction diode on a Si substrate. In the previous work, an Sb-doped n^+-$BaSi_2$/p^+-Si TJ and clear photoresponsivities in undoped n-$BaSi_2$ overlayers formed on the TJ were achieved.[79-81] In 2012, Du *et al.* formed 400 nm thick undoped n-type $BaSi_2$ epitaxial layers on a n^+-$BaSi_2$/p^+-Si junction on Si(111) by MBE. The photoresponsivity reached a maximum value at 1.55 eV. The photoresponsivity (*IQE*) was increased from 0.17 A/W (33%) to 0.37 A/W (71%) at 1.55 eV when V_{bias} was increased from 0.5 to 2.0 V. These values are the highest ever reported for semiconducting silicides at that time, owing to the effective suppression of Sb atom diffusion by the intermediate c-Si layer grown using the solid phase epitaxy (SPE) technique.[82] Recently, Kodama *et al.* first demonstrated the operation of $BaSi_2$ homojunction solar cells. Figure 1.21(a) shows the band alignment of proposed n^+-$BaSi_2$ (20 nm, $n = 1 \times 10^{19}$ cm^{-3})/p-$BaSi_2$ (500 nm, $p = 1 \times 10^{17}$ cm^{-3})/p^+-$BaSi_2$ (50 nm, $p = 1 \times 10^{19}$ cm^{-3})/p^+-Si(111) ($\rho < 0.01\Omega$cm) diodes. The influence of a large ΔE_V at the p^+-$BaSi_2$/p^+-Si interface was diminished by using the heavily doped p^+-Si substrate. Figures 1.21(b) and 1.21(c) are *J*–*V* characteristics under AM1.5G illumination and *IQE* spectra for the n^+-$BaSi_2$ (20 nm)/p-$BaSi_2$ (500 nm)/p^+-$BaSi_2$ (50 nm) diodes. The *J*–*V* curve in Fig. 1.21(b) is for the sample with $p = 1 \times 10^{16}$ cm^{-3}. As shown in the figure, leakage current was large in the homojunction diode as expected. The *IQE* became pronounced at $\lambda < 800$ nm in Fig. 1.21(c), while the *IQE* was very small at $\lambda > 800$ nm because the photogenerated electrons in the p^+-Si recombined with holes before reaching the built-in field region. On the other hand, the *IQE* exceeded 30% at $\lambda = 500$ nm. Considering that the absorption length ($3/\alpha$) at $\lambda = 500$ nm is approximately 100 nm in $BaSi_2$,[44] so the *IQE* spectrum in Fig. 1.21(c) was attributed to the photogenerated carriers originating from the p-$BaSi_2$ layer and then they were separated by the built-in electric field in the $BaSi_2$ pn junction diode. The *IQE* value distinctly increased as the *p* of the p-$BaSi_2$ layer decreased from 1×10^{17} to 1×10^{16} cm^{-3}, while the J_{SC} values were 1.3 and 3.6 mA/cm^2, respectively. On the basis of these results, the operation of a $BaSi_2$ homojunction solar cell was achieved for the first time.[76] η is as small as ~0.1% because of large leakage currents caused by defects resulting from step bunching at the p^+-$BaSi_2$/p^+-Si interface.[83]

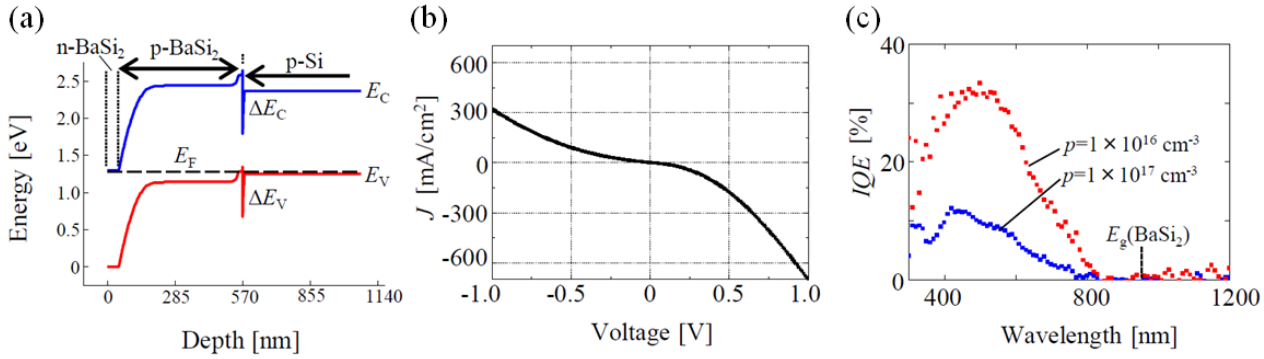

Fig. 1.21 (a) Band alignment; (b) *J*–*V* characteristics under AM1.5G illumination and (c) *IQE* spectrum for n^+-$BaSi_2$/p-$BaSi_2$/p^+-$BaSi_2$/p^+-Si diodes.[76]

1.3 Aim of this thesis

As we discussed above, $BaSi_2$ has great potential as a new material for thin-film solar cell applications. On our way to the fabrication of high-η $BaSi_2$/c-Si tandem solar cells, a lot of research items need to be done to clarify the physical properties of n- and p-type $BaSi_2$ films, and optimal structure of $BaSi_2$-based solar cells. The aims of this thesis are list as follows:

1) Clarifying the transport properties of n- and p-type $BaSi_2$ films. There are some investigations devoted to the study of $BaSi_2$ basic electronic and optical properties, but at the same time there is almost the lack of information on its transport properties. So in chapter 2, we formed undoped n-$BaSi_2$ and B-doped p-$BaSi_2$ films, and presented extended experimental data on the mobility of electrons and holes in n- and p-$BaSi_2$ films in the temperature range of 50–300 K along with their theoretical interpretation.

2) Investigation of p-$BaSi_2$/n-Si solar cells formed on textured n-Si(001) with a pyramid structure consisting of {111} facets. In chapter 3, in order to improve solar cell performance of p-$BaSi_2$/n-Si heterojunction solar cells, a Si(001) substrate is textured with Si{111} facets by etching. These textured structures have been used to trap incident light, which improves solar cell performance.

3) Fabrication of p-$BaSi_2$/n-Si solar cells on flat Si(001). In chapter 4, we investigate the potential of Si(001) substrates for p-$BaSi_2$/n-Si heterojunction and $BaSi_2$ homojunction solar cells. We formed p-$BaSi_2$ films on Si(001) substrates with thicknesses in the range of 20–60 nm and found its effects on the solar cell performances.

4) Exploring the potential of $BaSi_2$ homojunction solar cells on a p^+-$BaSi_2$/p^+-Si TJ. In chapter 5, to explore the potential of a Si(001) surface for $BaSi_2$/c-Si tandem solar cells, we fabricated p^+-$BaSi_2$/p^+-Si TJ serving for $BaSi_2$ homojunction solar cells.

5) Simulation of $BaSi_2$ homojunction and BaC_xSi_{2-x}/c-Si tandem solar cells. In chapter 6, some simulations and theoretical calculations have been done using Silvaco Atlas simulation package to point out the best parameters of the solar cell, so as to guide the experiment.

Chapter 2 Transport properties of $BaSi_2$

2.1 Scattering mechanisms in semiconductors

There are several standard and well-known scattering mechanisms such as ionized impurity, polar optical phonon, non-polar optical phonon, acoustic phonon, neutral impurity, and GB scatterings, that affect the carrier mobility of materials. Many investigations have been done to make carriers' transport properties clear. For poly-Si films, the electrical properties have been interpreted in terms of two distinct models: the segregation theory, according to which impurity atoms tend to segregate at the GB where they are electrically inactive,[84] and the GB trapping theory assuming the presence of a large amount of trapping states at the grain boundary able to capture, and therefore immobilize free carriers. As a result, the mobility of the carriers is restricted, affecting the performance of devices based on poly-Si films.[85,86] GaAs is a polar semiconductor, which is widely used as PVs in space. The theoretical and experimental result of temperature dependent mobility is shown in Fig. 2.1. It can be seen that at low, intermediate, and higher temperatures, the mobility is dominated by ionized impurity, piezoelectric, and polar optical scattering, respectively.[87]

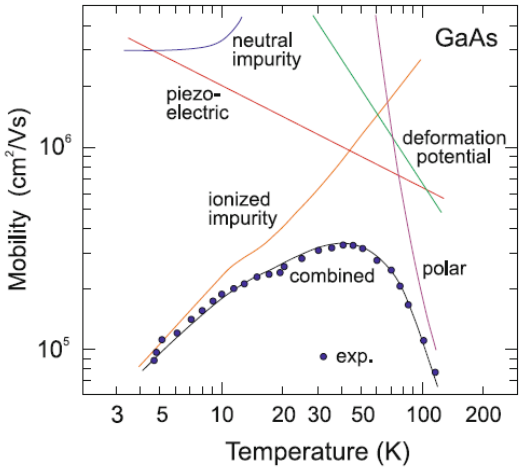

Fig. 2.1 Temperature dependent mobility of n-type GaAs.[88]

β-$FeSi_2$, another semiconducting silicide, has been attracting significant attention due to its large absorption coefficient of over 10^5 cm^{-1} at 1 eV.[89] Reports on light-emitting diodes operating at the wavelength corresponding to optical fiber communication have renewed interest in β-$FeSi_2$.[90] Therefore, β-$FeSi_2$ is considered to be promising as an infrared light emitter and a detector on Si substrates. However, the scattering mechanisms affecting the measured mobility of β-$FeSi_2$ have not been clarified. Furthermore, the highest mobility that could be obtained in β-$FeSi_2$ at RT, which is very important for device applications, has not been clarified. In 2005, K. Takakura et al. found that for undoped p-type β-$FeSi_2$ thin-films, the hole mobility increased to approximately 450 cm^2/Vs at RT with increasing annealing temperature and time. The observed hole mobility was analyzed by considering various carrier scatterings such as acoustic-phonon and polar-optical-phonon scatterings, intervalley scattering, ionized impurity scattering, and GB scattering. The nice fit of the mobility to the experimental results reveals that the polar-optical-phonon scattering determines the hole mobility at RT.[91]

As we discussed in chapter 1, $BaSi_2$ is attractive for solar cell applications, and there are some

investigations devoted to the study of $BaSi_2$ basic electronic and optical properties.[42,92] However, at the same time, there is almost the lack of information on its transport properties, which is very important for us to get a deeper understanding of $BaSi_2$. In this chapter, electron and hole mobilities versus temperature in semiconducting $BaSi_2$ have been systematically studied both experimentally and theoretically. The experiments were performed with undoped 250 nm-thick $BaSi_2$ polycrystalline films grown by MBE. The grain size of films ranged from 0.2 to 5 μm with the n of 5.0×10^{15} cm^{-3}. To investigate the hole mobility, B-doped p-$BaSi_2$ films with various dopant concentrations were fabricated and studied.

2.2 Experiments

In this experiment, 11 samples have been formed. For the fabrication of undoped n-$BaSi_2$ films, an SOI substrate with a 1 μm-thick n-Si(111) topmost layer (ρ > 1000 Ωcm) was used. This substrate was formed by bonding 500 μm-thick high resistive floating-zone (FZ) n-Si(111) and SiO_2-capped Si(001) handle wafers. Then, the FZ-Si wafer was mechanically ground and polished by chemical mechanical polishing down to about 1 μm thickness. On the other hand, for B-doped p-$BaSi_2$ films, we used 500 μm-thick high-resistivity (ρ > 1000 Ωcm) FZ n-Si(111) and n-Si(001) substrates. For all the samples, after cleaning the substrate by heating at 900 ℃ for 30 min in ultrahigh vacuum, a 5 nm-thick $BaSi_2$ template layer was grown on the Si substrate synthesized by RDE at 500 ℃ using only the Ba source. This template layer works as a kind of seed crystals for the subsequent $BaSi_2$ layer. Then a 250 nm-thick undoped $BaSi_2$ film was formed on top of the template at 600 ℃ in the MBE mode using both Ba and Si sources. For B-doped p-$BaSi_2$ films, Ba, Si, and B were evaporated on the template layer at 600 ℃. The B concentration was controlled by the crucible temperature of the B K-cell (T_B) which was varied as 1000, 1100, 1170, 1230, and 1300 ℃. Afterwards, a 3 nm-thick a-Si layer was deposited to prevent oxidation of the $BaSi_2$ films. The deposition rates of Si and Ba were controlled using an electron impact emission spectroscopy (EIES; INFICON) feedback system. The growth conditions were summarized in Table 2.1.

Table 2.1 Growth conditions of samples.

Sample No.	Substrate	RDE			MBE					
		T_{sub} [°C]	R_{Ba} [nm/min]	Time [min]	T_{sub} [°C]	R_{Ba} [nm/min]	R_{Si} [nm/min]	T_B [°C]	Time [min]	Thickness [nm]
A	SOI	500	1	20	600	2.0	1.2	-	120	250
B1	FZ n-Si(111) ρ > 1000Ωcm	500	1	5	600	2.56	0.9	1000	240	320
B2								1100	240	340
B3								1170	390	600
B4								1230	300	580
B5								1300	360	700
C1	FZ n-Si(001) ρ > 1000Ωcm	500	1	5	600	2.2	0.9	1000	300	450
C2								1100		490
C3								1170		440
C4								1230		460
C5								1300		440

The crystal structure of the films was characterized by X-ray diffraction (XRD) using Cu Kα radiation and plan-view transmission electron microscopy (TEM) in TOPCON EM-002 device operated at 120 kV. EBSD analyses were performed to analyze the grain size of $BaSi_2$. Concentration and mobility of electrons and holes,

which were main charge carriers in the fabricated undoped and B-doped films, respectively, were measured by the Hall technique at temperatures between 50 and 300 K using a closed-cycle He cryostat on the van der Pauw structures with ohmic contacts made by sputtered Al. The applied magnetic field was 0.2 T. The measurement temperature was limited down to 145 K for undoped n-$BaSi_2$, because of the difficulty in assuring ohmic contacts at such low temperatures.

2.3 Results and discussions

The n of undoped $BaSi_2$ extracted from the Hall measurements occurred to be 5.0×10^{15} cm^{-3} at RT. This value has been cross-checked by another method using the slope of the $1/C^2$ versus voltage plot, where C is the capacitance.[75] The activation energy of donor levels was approximately 30 meV, and the electron concentration did not change a lot in the measurement temperature range of 150−300 K.[93] The p of B-doped p-$BaSi_2$ on Si(111) also did not show any significant change in the measurement temperature range of 50−300 K, but depended on T_B thereby the B concentration and it was varied from 5.0×10^{16} to 5.3×10^{18} cm^{-3} at RT. The activation energy of acceptor levels was in the range between 20 and 30 meV.[94] The fact that the $BaSi_2$ is a semiconducting material in the above temperature range has been confirmed by the temperature dependence of spectral response.[95] B concentration (N_B) was determined by secondary ion mass spectrometry (SIMS) using C_S ions. Figure 2.2 shows Arrhenius plots of N_B in B-doped $BaSi_2$ films. SIMS measurements revealed that as T_B increases, N_B increases exponentially with an activation energy of 6.2 eV.

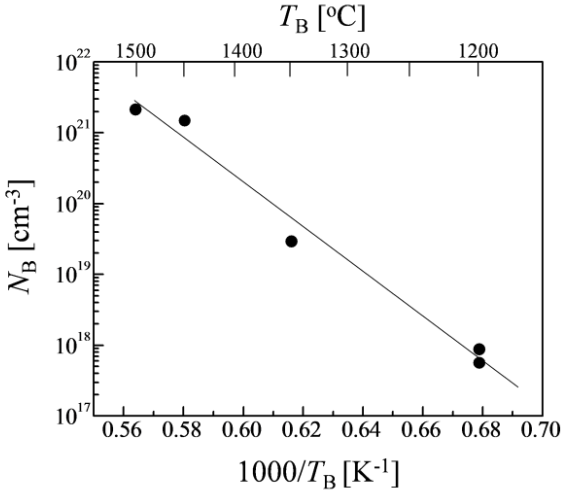

Fig. 2.2 Arrhenius plot of B concentration N_B.

Figure 2.3 shows examples of θ-2θ XRD patterns, taken for samples B3 and C3. Their RHEED patterns of p-$BaSi_2$ films, observed along the Si[11-2] azimuth on Si(111) and Si[1-10] azimuth on Si(001) are also presented. As shown in Fig. 2.3, intense (100)-oriented diffraction peaks in the XRD patterns and sharp streaky RHEED patterns can be observed. These results indicate the epitaxial growth of B-doped $BaSi_2$ films on both Si(111) and Si(001) substrates. Similar a-axis-oriented $BaSi_2$ films were obtained for all the samples regardless of B concentration and substrate orientation. (*) indicate in the figures correspond to the diffraction peak attributed from Si substrate.

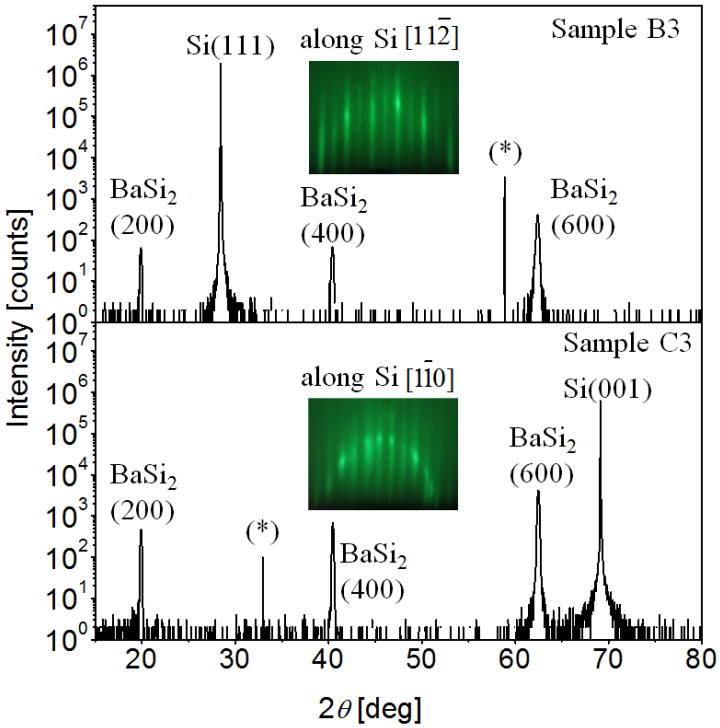

Fig. 2.3 θ-2θ XRD and RHEED patterns of sample B3 and C3. (*) represent the diffraction peak attributed from Si substrate.

Figures 2.4(a) and 2.4 (b) show typical examples of bright-field (BF) and dark-field (DF) TEM images, respectively, along the $BaSi_2$ [100] azimuth for sample A. The incident electron beam was slightly tilted for the GBs to be seen clearly. The dark-field image was taken under a two-beam diffraction condition to clarify the grain size of $BaSi_2$. The *a*-axis-oriented $BaSi_2$ epitaxial layer has grains with three $BaSi_2$ epitaxial variants rotated by 120 deg to each other in the surface normal direction related to the three fold symmetry of Si(111).[63] One of them is bright in Fig. 2.4 (b). The grain size of sample A was distributed in the range of 0.2–5 μm in the lateral dimensions with the simple orthorhombic crystal structure. The average diameter is approximately 2.7 μm as shown later. The grain size in the MBE-grown $BaSi_2$ is dependent on the RDE growth conditions and can be varied from approximately 0.2 to more than 4 μm on Si(111).[65,96]

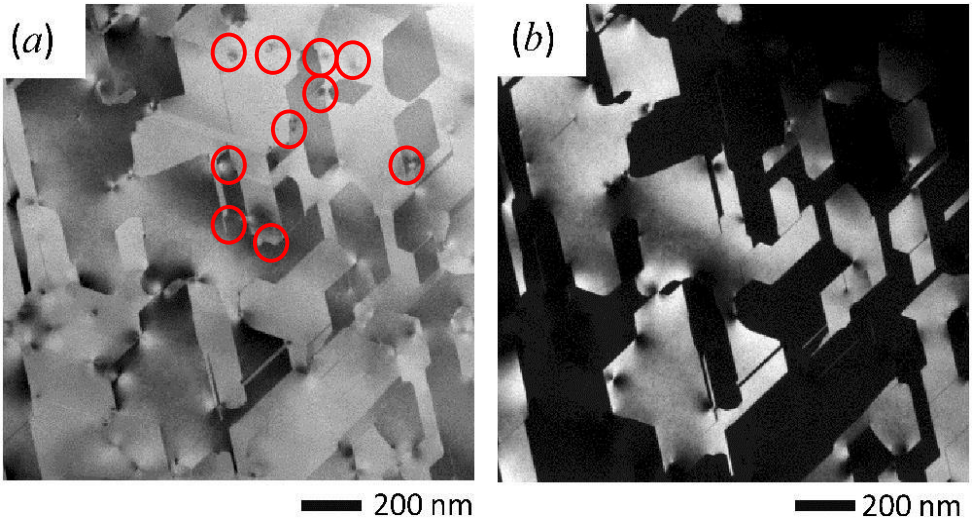

Fig. 2.4 (a) Bright-field and (b) dark-field plan-view TEM images of sample A observed along $BaSi_2$ [100].

Figures 2.5(a) and 2.5(b) are the counterparts of Figs. 2.4(a) and 2.4(b), respectively, for B-doped p-$BaSi_2$ film grown at T_B=1100 ℃ (sample B2). In comparison with the undoped $BaSi_2$ film in Figs. 2.4(a) and 2.4(b), the grain size of B-doped $BaSi_2$ decreased and the GBs became a little dim and roundish, indicating the crystalline quality was degraded with doping. The decrease in the grain size of B-doped $BaSi_2$ is probably attributed to the suppressed migration of Ba and Si atoms during MBE. The dislocations, shown by small red circles, apparently observed in the TEM images of Figs. 2.4(a) and 2.5(a) are characterized by the density of about 3.5×10^9 cm^{-2} in undoped $BaSi_2$ (sample A) and of 5.4×10^9 cm^{-2} in B-doped p-$BaSi_2$ at T_B=1100 ℃ (sample B2), indicating that the dislocation concentration increased by the doping of B. These values can be underestimated. Hence, more dislocations are likely to be present in the grown films. With increasing B concentration, B atoms tend to precipitate in $BaSi_2$,[94] and hence those precipitates may act as nuclei for dislocations.

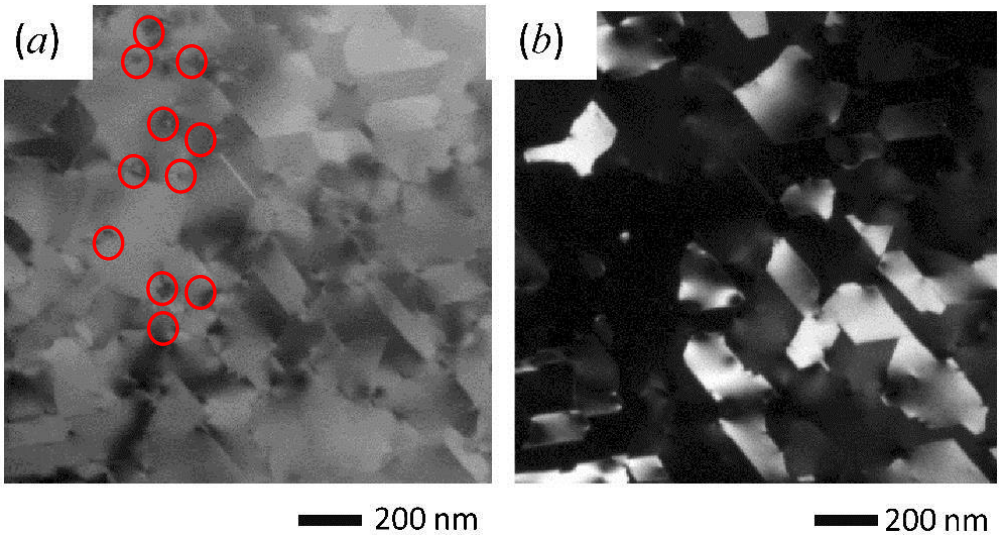

Fig. 2.5 (a) BF and (b) DF plan-view TEM images of sample B2 with T_B=1100 ℃, observed along $BaSi_2$ [100].

To provide an overview of how the grain size of $BaSi_2$ film depends on N_B, we have conducted EBSD measurements. Figures 2.6(a)–2.6(g) show EBSD crystal orientation maps of $BaSi_2$ epitaxial films and distribution histograms of $BaSi_2$ grain size for samples (a) undoped n-$BaSi_2$ (sample A), with T_B = (b) 1000 ℃ (sample B1), (c) 1170 ℃ (sample B3), and (d) 1300 ℃ (sample B5) on Si(111), and with T_B = (e) 1000 ℃ (sample C1), (f) 1170 ℃ (sample C3), and (g) 1300 ℃ (sample C5) on Si(001). Three colors in the orientation maps in Figs. 2.6(a)–2.6(d), those are red, green, and blue, denote three epitaxial variants in the *a*-axis-oriented $BaSi_2$ films on Si(111) substrate. While in Figs. 2.6(e)–2.6(g), the colors are red and blue, denote two epitaxial variants in the *a*-axis-oriented $BaSi_2$ films on Si(001) substrate. The calculated average sizes of grains are also presented. Although the precise grain size can be obtained by plan-view TEM as presented in Figs. 2.4 and 2.5, the EBSD results revealed that the grain size of $BaSi_2$ decreased with N_B. Completely the same analysis was performed for the $BaSi_2$ epitaxial films on Si(001) substrates and the average grain sizes calculated from the histograms was estimated to be 7.8, 5.7 and 4.7 μm for the appropriate samples, respectively. Note that the grain size of $BaSi_2$ films on Si(001) was much larger than that on Si(111), and also decreased when N_B was increased.

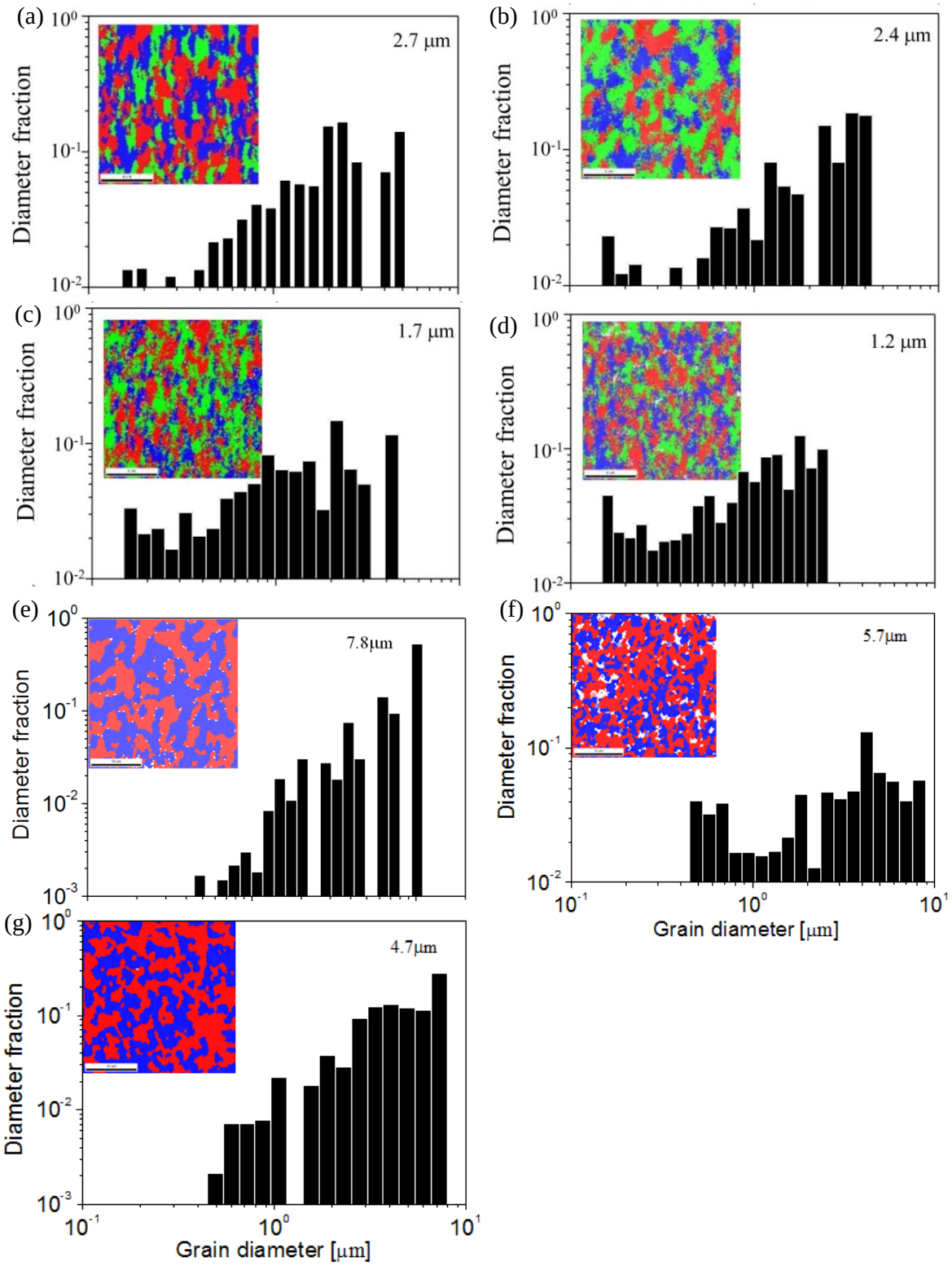

Fig. 2.6 EBSD crystal orientation maps of $BaSi_2$ epitaxial films and distribution histograms of $BaSi_2$ grain size for samples (a) undoped n-$BaSi_2$ (sample A), with T_B = (b) 1000 ℃ (sample B1), (c) 1170 ℃ (sample B3), and (d) 1300 ℃ (sample B5) on Si(111), and with T_B = (e) 1000 ℃ (sample C1), (f) 1170 ℃ (sample C3), and (g) 1300 ℃ (sample C5) on Si(001).

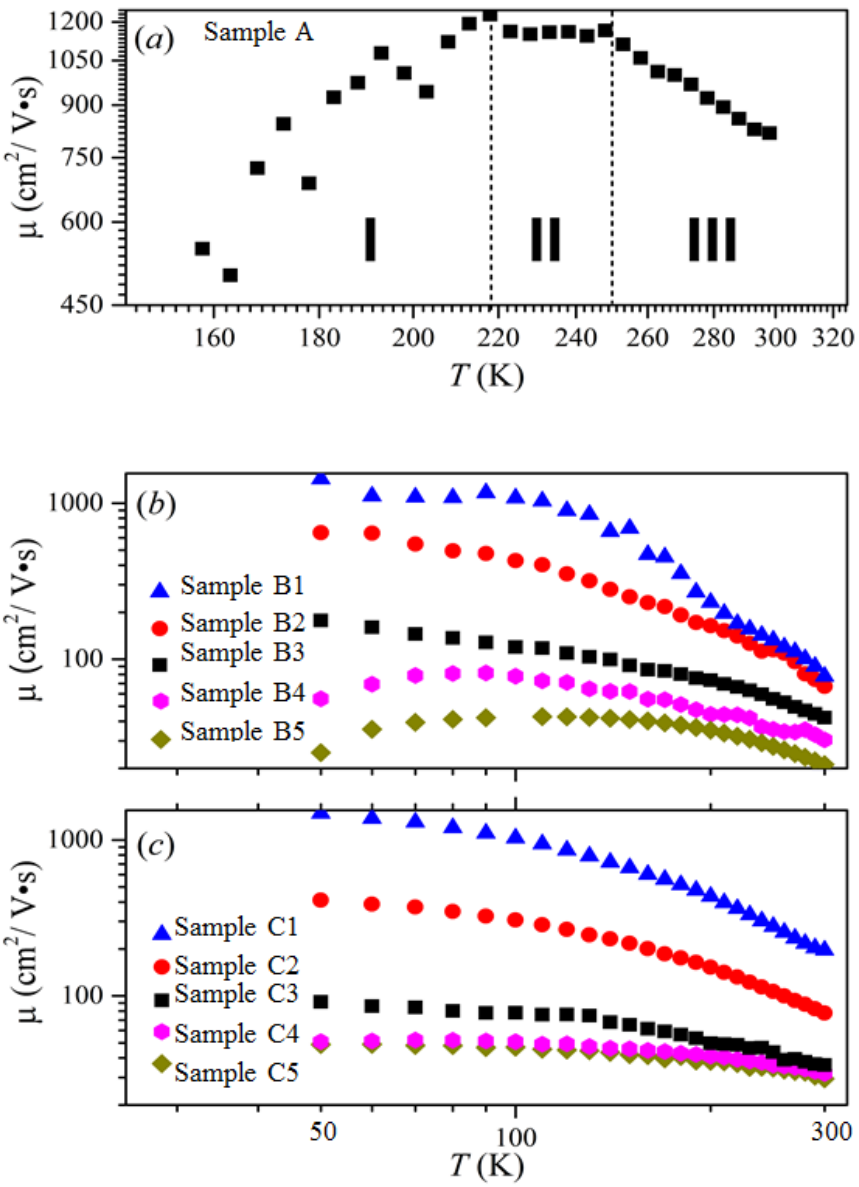

Fig. 2.7 The experimentally measured carrier mobility versus temperature in $BaSi_2$ films: (a) Hall mobility of electrons in sample A; (b) and (c) mobility of holes in p-doped films grown on Si(111) and Si(001) substrates, respectively.

The electron mobility of sample A measured as a function of temperature is shown in Fig. 2.7(a) and such dependence can be conventionally divided into three main regions. The region I ($160 \leq T \leq 218$ K) displays a sharp mobility raise with temperature till it reaches the maximum. The main scattering mechanism here is possibly defined by electron scattering on charge centers since the slope of the mobility curve closely follows the $T^{3/2}$ law.[72] The region II ($218 \leq T \leq 243$ K) represents the region of the mobility maximum, while the region III ($243 \leq T \leq 298$ K) is characterized by the fast mobility drop due to electron scattering on phonons with the almost $T^{-3/2}$ dependence. In addition to that the position of the mobility maximum (1230 $cm^2/V{\cdot}s$ at 218 K) is shifted to the high temperature region as compared to other semiconducting silicides as well as the mobility itself has rather high values.[97-101] Meanwhile, the mobility decreases to 816 $cm^2/V{\cdot}s$ at RT.

Hole mobility in B-doped p-$BaSi_2$ measured as a function of temperature is shown in Figs. 2.7 (b) and (c). The following features can easily be traced: (1) The mobility (in p-$BaSi_2$) at RT is about one order or four times smaller than the electron mobility (in n-$BaSi_2$) for the films grown on (111) or (001) Si substrates,

respectively. Also the hole mobility at appropriate temperatures has a tendency to decrease considerably from sample to sample when the dopant concentration increases. (2) The effect of scattering on charge centers or at the GBs was traced only at low temperatures (at T < 100 K) for the two cases (samples B4 and B5 in Fig. 2.7 (b)) with the highest dopant concentrations (and also for the smallest average grain sizes). That means such an effect should be noticeable within a more extended temperature range in films with grains smaller than 1 μm. (3) Contrary to n-$BaSi_2$ (Fig. 2.7 (a)), the mobility maximum is located at temperatures lower than 100 K and for all the cases of p-$BaSi_2$ (Figs. 2.7 (b) and (c)) at T > 100 K the charge carrier mobility is defined mainly by scattering on phonons plus possible contribution by scattering on neutral impurity centers (as far the latter to be temperature independent).

2.4 Calculation

Several standard and well-known scattering mechanisms are usually considered in semiconductors.[88,102] Each mechanism can be described by the complex function of meaningful physical values which can be treated as an appropriate set of parameters. In our case if one accounts for all the possible scattering mechanisms the resulting relaxation time according to the Mathiessen's formula is

$$1/\tau = 1/\tau_{AC} + 1/\tau_{NPO} + 1/\tau_{PO} + 1/\tau_{CIC} + 1/\tau_{NIC}, \quad (2.1)$$

where τ_{AC}, τ_{NPO}, τ_{PO}, τ_{CIC}, τ_{NIC}, are partial relaxation times defined by carrier scattering on acoustic phonons, nonpolar and polar optical phonons, and charge and neutral impurity centers, respectively. Previously this approach was used for a number of semiconducting silicides.[97-101]

In the case of parabolic bands and nondegenerate charge carriers for each separate mechanism one has [88,102]

$$1/\mu_i = \left[\frac{4q}{3m^*(kT)^{5/2}\sqrt{\pi}} \int_0^\infty E^{\frac{3}{2}}\tau_i \exp\left(-\frac{E}{kT}\right) dE\right]^{-1}, \quad (2.2)$$

where m^* is the carrier effective mass (for electrons in bulk $BaSi_2$ it is 0.42 with m_{xx}=0.6; m_{yy}=0.37; m_{zz}=0.3 and for holes it is 0.57 since m_{xx}=0.31; m_{yy}=0.73; m_{zz}=0.67 in units of free-electron mass[42]), q is the electron charge, T is the absolute temperature, k is the Boltzmann constant, and τ_i is the momentum relaxation time of the i-th mechanism.

For acoustic phonon scattering, the relaxation time is [88,102]

$$1/\tau_{AC} = \frac{\sqrt{2m^{*3}E}D^2kT}{\pi\hbar^4q^2\rho v_s^2}, \quad (2.3)$$

where ħ is the reduced Plank constant, ρ is the material density (3.66 g/cm^3 for $BaSi_2$ [97]), v_s is the mean longitudinal sound velocity (4.1×10^5 cm/s for $BaSi_2$ [103]) , and D is a constant defined by the components of the deformation potential tensor. Usually it varies from 5 to 15 eV in semiconductors.[88,102]

For optical nonpolar phonon scattering, the relaxation time is [88,102]

$$1/\tau_{NPO} = 1/\tau_{AC}\left[C\left(1+\frac{kT_0}{E}\right)^{\frac{1}{2}} + \exp\left(\frac{T_0}{T}\right)\left(1-\frac{kT_0}{E}\right)^{\frac{1}{2}}\right], \quad (2.4)$$

where T_0 is the Debye temperature, $C = \eta/2\left(\frac{T_0}{T}\right)\left(\exp\left(\frac{T_0}{T}\right)-1\right)^{-1}$, and $\eta = (D_{NPO}/D_{AC})^2$. The latter ratio of the nonpolar optical deformation potential to the acoustic one is a parameter of the model.

Recently the thermoelectric properties of $BaSi_2$ were studied as well as the longitudinal sound velocity

was experimentally measured and the Debye temperature was estimated to be as low as 260 K for the acoustical mode of the phonon spectrum.[103] On the other hand, the lattice dynamic properties were estimated from the first principal calculations pointing out from the presented phonon band structure that there are several optical modes and the highest frequency of the optical modes is 493 cm^{-1} which corresponds to the Debye temperature to be about 700 K.[104] Moreover it should be noted that for acoustic phonons the Debye temperature has been estimated to be 240 K which correlates well with experimental data.[103]

The momentum relaxation time due to polar optical phonon scattering is [88,102]

$$1/\tau_{\mathrm{PO}} = \sqrt{\frac{m^*}{2^5 E}}\frac{kT_0 q^2}{\pi\hbar^2\varepsilon_p}\left\{ n(\omega_0)\left(1 + \frac{kT_0}{E}\right)^{\frac{1}{2}} + [n(\omega_0)+1]\left(1 - \frac{kT_0}{E}\right)^{\frac{1}{2}} + \frac{kT_0}{E}\left[(n(\omega_0)+1)\,\mathrm{arcsinh}\left(\frac{E}{kT_0} - 1\right)^{\frac{1}{2}} - n(\omega_0)\,\mathrm{arcsinh}\left(\frac{E}{kT_0}\right)^{\frac{1}{2}}\right]\right\}, \tag{2.5}$$

where ω_0 is the optical phonon frequency ($\omega_0 = kT/\hbar$), $n(\omega_0)=(\exp(\hbar\omega_0/kT) - 1)^{-1}$, $\varepsilon_p = (1/\varepsilon_{in} - 1/\varepsilon_0)^{-1}$, ε_{in} and ε_0 are the high-frequency and the static dielectric constants (ε_0 = 14.6 and ε_{in} = 3.2 for $BaSi_2$ [42]), respectively.

Currently, there are some models describing scattering by charge centers, such as the Brooks–Herring or Conwell–Weisskopf models [88,102] or recently proposed modified model by N. A. Poklonski *et al*.[105] However, they all give qualitatively the same results. For the scattering by charge centers, the relaxation time is given by [88,102]

$$1/\tau_{\mathrm{CIC}} = \frac{\pi N_{\mathrm{i}} Z^2 q^4}{\varepsilon_0^2 E^{\frac{3}{2}}\sqrt{2m^*}}\left[\ln(1+x) - \frac{x}{1+x}\right], \tag{2.6}$$

where N_{i} is the charge centers concentration, Z is the charge value of the center, $x = 8mEr_0^2/\hbar^2$, $r_0 = (\varepsilon_0 kT/4\pi nq^2)^{1/2}$ is the Debye screening radius, n is the self-carrier concentration ($n = 5.0 \times 10^{15}$ cm^{-3} for $BaSi_2$). And finally the Erginsoy's formula can be used [88,102] for the neutral impurity scattering mechanism

$$1/\tau_{\mathrm{NIC}} = \frac{20\varepsilon_0 N_0 \hbar^3}{m^{*2} q^2}, \tag{2.7}$$

where N_0 is the neutral center concentration.

Summarizing for the theoretical simulation we accounted for carrier scattering by the different kinds of phonons and by charge and neutral impurity centers. Generally, there are other possible scattering mechanisms,[88,102] but they do not play a noticeable role for our particular cases. As far as the dislocation density was estimated to be of the order of less than 10^{10} cm^{-2} in all our studied samples of $BaSi_2$ and the mentioned mechanism would influence the resulted mobility for the density to be at least of the order of 10^{11} cm^{-2}, we have excluded the carrier scattering by the dislocations from the analysis. Thus, in our theoretical modeling we have only 4 unknown parameters: D (constant defined by the components of the deformation potential tensor), η (ratio of polar optical phonons to acoustic phonons deformation potential tensors) and the charge (N_i) and neutral (N_0) impurity center concentrations as far as we know nothing *a* priori or from the experimental data about their possible values. All the other parameters for the scattering mechanisms considered were experimentally measured or reliably estimated.

2.4.1 Calculation of the electron mobility in n-$BaSi_2$ films

All the above mentioned mechanisms of electron scattering represented by formula (2.3) through (2.7) were accounted for the numerical simulation of the electron mobility in $BaSi_2$ as a function of temperature. The main results are shown in Fig. 2.8. We have found a lot of reasonable sets of realistic parameters to reproduce only the region I or III of the experimental curve in addition to a few reasonable sets of realistic parameters to reproduce at least qualitatively *e.g*. the regions II and III of the experimental curve simultaneously as shown in

Fig. 2.8(a). The latter results were obtained for the following set of parameters: D = 4 eV; η = 5; N_i = 2.0 ×10^{16} cm^{-3} and N_0 = 5.0 ×10^{15} cm^{-3} or less. Also we need to emphasize that the Debye temperature is one of the key parameters to reproduce the experimental data correctly. In our case the Debye temperature of 850–900 K is considerably higher than the possible experimental one of 700 K. And finally we stress out that one can correctly reproduce either the mobility rise with temperature due to scattering on charge impurity centers as well as the presence of the mobility maximum (to be about 1230 cm^2/V s) at the appropriate temperature (at 218 K) or the mobility drop with temperature due to scattering on phonons along with the correct position of the mobility maximum. But there is no any reasonable set of realistic parameters that allows one to reproduce, at the same time, all the regions of the experimental mobility data within the standard theoretical approach. In fact, in the theoretical modeling the region II is always rather broad as clearly seen in Fig. 2.8(a).

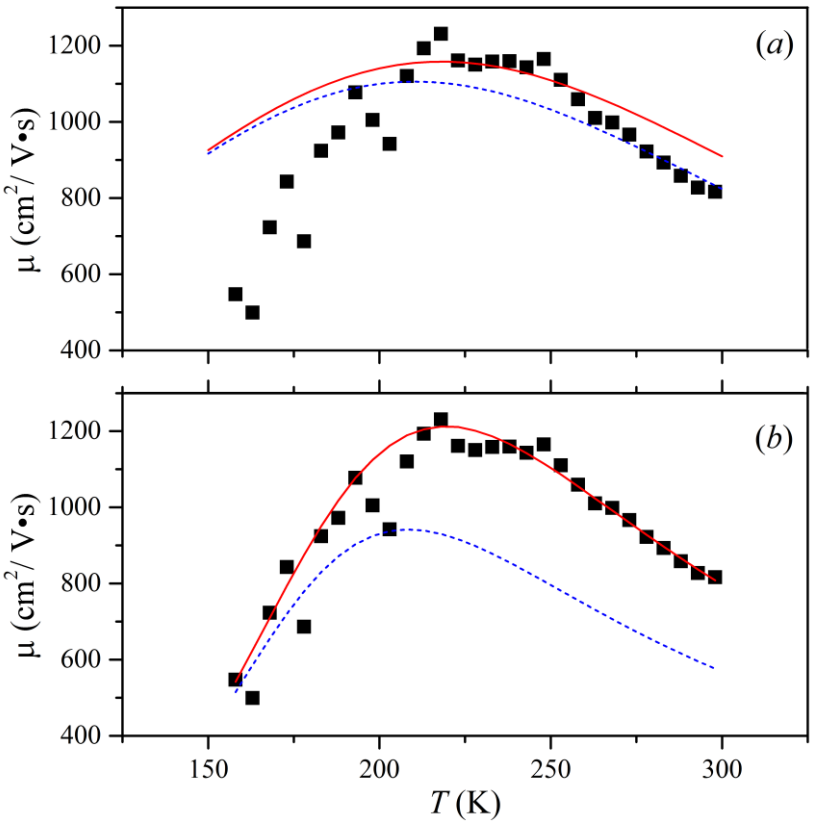

Fig. 2.8 Electron mobility versus temperature in n-$BaSi_2$ films: (a) comparison of the experimental data and theoretical results within the standard approach (experiment–black squares, simulation–solid and dashed curves: the upper solid curve at T_0 = 900 K and lower dashed one at T_0 = 850 K); (b) comparison of the experimental data and theoretical results within the modified model (experiment–black squares, simulation–solid and dashed curves: the upper solid curve at T_0 = 700 K and the lower dashed one at T_0 = 540 K).

It is evident that for an adequate description of the observed experimental data the theoretical approach requires some modifications. We make the following assumptions. The first one is the grained nature of the studied samples. Thus, the intergrain boundaries can be treated as small potential barriers preventing charge carriers to escape from a grain at low temperatures and specific activation energy is necessary to overcome the barrier. And the second assumption takes into consideration the fact that in general experimentally obtained Hall mobility is 1.13 or 1.98 times larger than the drift one, depending on the scattering mechanism.[102] Thus the resulting mobility can be written as $\mu^* = \gamma\,\mu\,\exp(-E_{GB}/kT)$, where E_{GB} is the potential barrier height at GBs and γ is the Hall factor. Figure 2.8(b) represents the results of the simulation by implementing this modified

approach with the following set of parameters: D = 4 eV; η = 2; $N_i = 8 \times 10^{15}$ cm^{-3}, $N_0 = 5.0 \times 10^{15}$ cm^{-3} or less and E_{GB} = 62 meV; γ = 1.8 and 1.2 for scatterings on charge centers and phonons, respectively. Here we note that the obtained value of the barrier height correlates well with the experimentally estimated one of 50 meV,[106] while the relative lowering of the Debye temperature results in nonadequate reproducing of the experimental data. However, it is also important to account for scattering on the charge impurity centers even at their relatively low concentrations (N_i of order of 10^{16} cm^{-3}). Moreover, recently it was proposed that Si vacancies in $BaSi_2$ are responsible for the presence of such centers [107] and their estimated concentration is in very good agreement with the results of our study. Such a simple approach allows one to understand the physics of the processes as well as it shows the importance to include the carrier tunneling through the intergrain potential barriers into consideration.

Another possible more strict and rigorous approach is to include directly in Eq. (2.1) one additional term which describes charge carrier scattering by the GBs,[88] namely

$$\mu_{GB} = \frac{qL_D}{\sqrt{8m^*\pi kT}} \exp\left(-\frac{E_{GB}}{kT}\right), \quad (2.8)$$

where L_D is the average grain size. Practically the same results as presented in Fig. 2.8(b) was reproduced by using this approach with the following set of parameters which summarized in Table 2.2 (the other parameter values were used as mentioned above) for the structures with three various grain size values. Here we emphasize that the most crucial parameter is the intergrain potential barrier height. The more the average grain size, the higher the intergrain barrier. For the structures with large grains the barrier height value could be twice or even more higher than that preliminary estimated from the experiment.[106] Also note that the concentration of the charge centers should be also substantially higher than 10^{16} cm^{-3} which was estimated before.[107] So the adequate values of the intergrain potential barrier height as well as the concentrations and the nature of various point defects in the material need to be investigated more thoroughly both from the experimental and theoretical point of view.

Table 2.2 Parameters used in the simulation of carrier mobility: D (constant defined by the components of the deformation potential tensor), N_i (charged impurity center concentration), E_{GB} (potential barrier height) and L_D (average grain size).

L_D [μm]	E_{GB} [meV]	N_i [cm^{-3}]	D [eV]
0.25	100	9×10^{15}	4
2.5	131	$10 - 12 \times 10^{16}$	3.5
5.0	141	$14 - 15 \times 10^{16}$	3.4

2.4.2 Calculation of the hole mobility in p-$BaSi_2$ films

We have also performed the theoretical simulation (hole scattering mechanisms represented by Eq. (2.3) through (2.8)) of the hole mobility according to the experimental data for B-doped $BaSi_2$ grown on Si(111) and our best theoretical fits are presented in Fig. 2.9. The data on the parameter values used in calculations are summarized in Table 2.3. To correctly reproduce the main features in the experimental temperature dependence of the hole mobility one should assume first of all that the D parameter value (which is characterized by the strength of the carrier-phonon interaction) is significantly different for the n- and p-type $BaSi_2$. This is due to the fact that in spite of the effective masses of electrons and holes are of the same order, the energy band extrema for the corresponding carriers are located in different ***k***-points of the Brillouine zone, where the maximum of the valence band is in the 0.7 × Γ-Y point, and the minimum of the conduction band is in the T point.[42] It results in different values of the deformation potential tensors (as

shown for some other materials such as Si, Ge, Bi [108]). Thus, the specific features of electron-phonon and hole-phonon coupling are mainly responsible for such a great difference in the corresponding values of electron and hole mobilities.

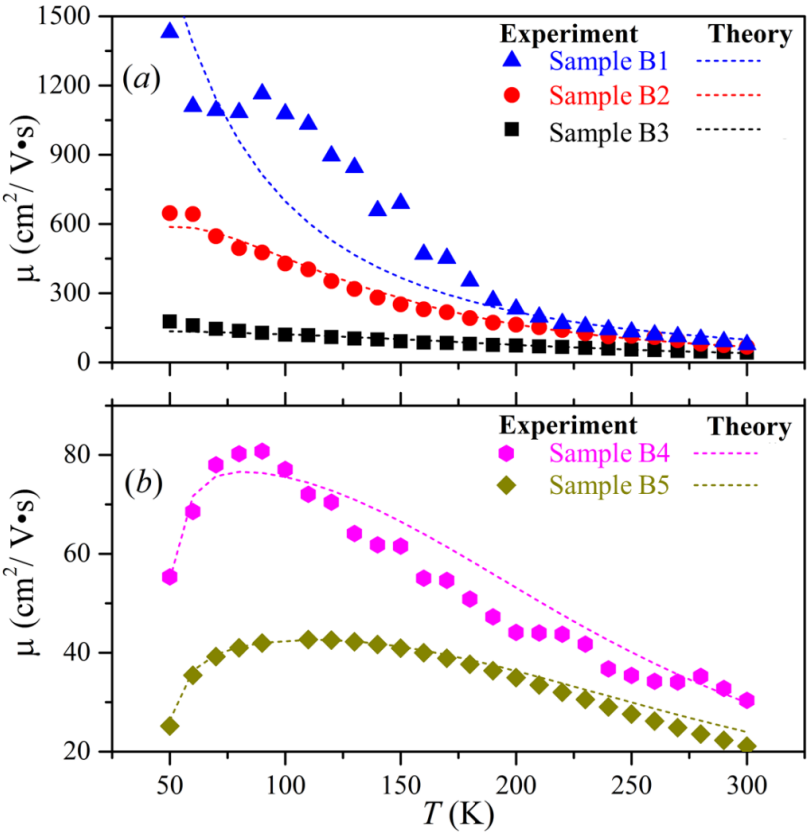

Fig. 2.9 Hole mobility versus temperature in p-$BaSi_2$ films on Si(111): (a) comparison of the experimental data and theoretical results for samples B1–B3; (b) comparison of the experimental data and theoretical results for the samples B4–B5.

Then it should be emphasized that the grain effect in mobility properties is negligible for the samples B1–B3 with the average grain size of more than 1.5 μm (Fig. 2.9(a)). In this case one should assume the appropriate intergrain potential barrier height to be less than 10 meV. Also it is interesting to note that for an adequate description of low temperatures behavior of hole mobility (at $T < 100$ K) for the rest of the samples B4–B5 with the highest dopant concentration (Fig. 2.9(b)), more pronounced potential barrier associated with the GBs should be introduced. Our estimates of the barrier heights to be 45 to 48 meV are consistent with the experimental data, that the barrier heights at the GBs in p-$BaSi_2$ were estimated to be a few tens of meV.[109] Also it should be emphasized here that the value of the intergrain potential barrier is rather different for the electron and the hole subsystems. On the whole it can be treated as an analogous of different band offset for the conduction and valence bands in heterojunctions. Moreover, there is one more feature for B-doped p-$BaSi_2$, namely, scattering on the neutral impurity centers has a great influence on the carrier mobility versus temperature behavior. One could note a strong increase of the concentration of neutral impurity centers with the dopant concentration. We think that this issue can be originated from the formation of a relatively deep donor/acceptor + vacancy level, which is initially in a charged state while after thermal activation it becomes neutral. The same tendency is valid for the charge impurity center concentration. Also it is interesting to note that MBE-grown $BaSi_2$ films can contain rather high concentration of oxygen

atoms.[110] In more detail, the possible mechanisms contributing to the Hall concentration, the concentration of neutral and charged centers are considered below.

Table 2.3 Parameters used in the simulation of carrier mobility: D (constant defined by the components of the deformation potential tensor), η (ratio of polar optical phonons to acoustic phonons deformation potential tensors), the charged (N_i) and neutral (N_0) impurity center concentrations, E_{GB} (potential barrier height) and L_D (average grain size).

	N_i [cm^{-3}]	N_0 [cm^{-3}]	D [eV]	η	E_{GB} [meV]	L_D [μm]
Si(111)						
n-type Sample A	8×10^{15} or higher	5×10^{15} or less	4	2	62 or higher	0.25 or higher
p-type Sample B1	1×10^{16}	5×10^{16} or less	12.5	1	10 or less	2.4
Sample B2	4×10^{16}	3.5×10^{17}	12.5	3		2.0
Sample B3	8×10^{16}	3.3×10^{18}	12.5	5		1.7
Sample B4	2×10^{17}	5.5×10^{18}	14	5	45	1.3
Sample B5	8×10^{17}	9.5×10^{18}	14	5	48	1.2
Si(001)						
p-type Sample C1	3×10^{16}	5×10^{16}	9	1	10 or less	7.8
Sample C2	7×10^{16}	7.2×10^{17}	12	3		6.0
Sample C3	7×10^{16}	6×10^{18}	12.5	3		5.7
Sample C4	2×10^{17}	9×10^{18}	12.5	3		5.2
Sample C5	2×10^{17}	1×10^{19}	12.5	3		4.7

One should note that unlike the situation with n-doped or p-doped $BaSi_2$ on Si(111) substrate the grain effect in mobility properties of the samples grown on Si(001) substrates is negligible for all the samples C1–C5 in this case. This is due to the fact that, on one hand, here we deal with the structures that consist of much larger grains and, on the other hand, it seems the appropriate intergrain potential barrier height to be less than 10 meV for such of the grains. All the above mentioned mechanisms of hole scattering represented by formulas (2.3) through (2.7) were accounted for in the numerical simulation of the hole mobility in $BaSi_2$ as a function of temperature. The main results are shown in Fig. 2.10. The data on the parameter values used in calculations are summarized in Table 2.3. On the whole, the experimental results show the mobility values for the samples with low dopant concentration to be noticeably higher in our case as compared to ones obtained for the films fabricated on Si(111) substrates. From our point of view this fact could be connected first of all with the significant difference in the sizes of the grains in the polycrystalline films generated on different Si substrates. And as a consequence this leads to the changes in the values of deformation potential which characterize the intense of the phonon-hole interaction. Thus we can suggest that there is some weak D and η dependence on the reciprocal effective grain size. Generally the same tendency was observed for the p-doped $BaSi_2$ samples on Si(111) substrates as well. Unfortunately, any theoretical quantitative estimates of this function, a priori, could not be done. Moreover any precise empirical attempt to establish such the function is also problematic due to the fact that the grain size distribution in our cases have a non-central character, *i.e.* a whole ensemble of the grains with rather close but different sizes almost equally make contributions to the resulting value of the mobility.

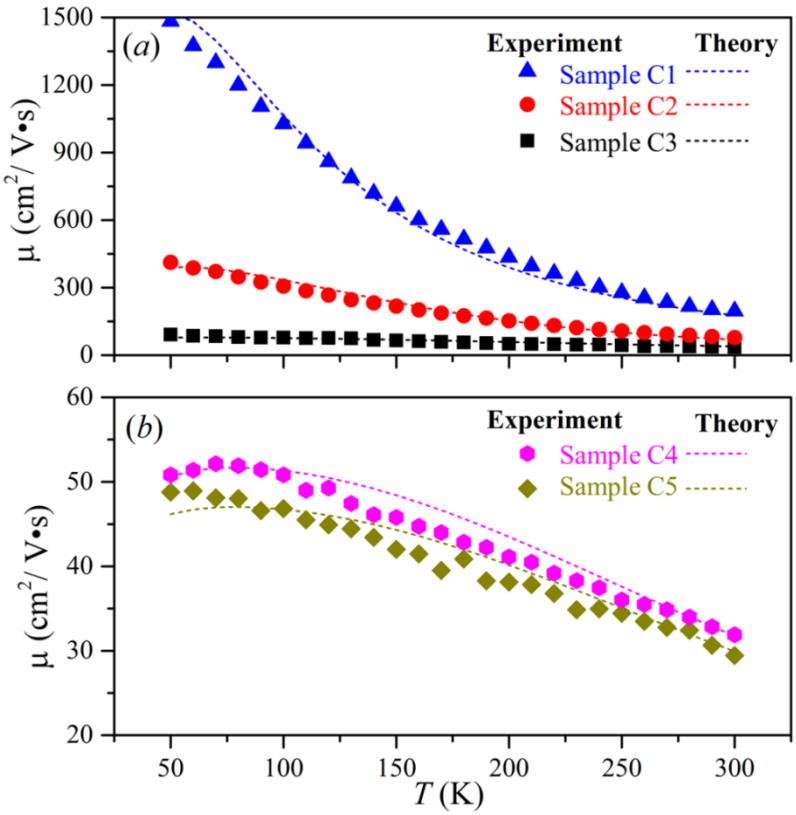

Fig. 2.10 Hole mobility versus temperature in p-$BaSi_2$ films on Si(001): (a) comparison of the experimental data and theoretical results for samples C1–C3; (b) comparison of the experimental data and theoretical results for samples C4–C5.

Like the situation with the B-doped p-$BaSi_2$ films on Si(111) substrates there is one more feature for the films on Si(001) substrates, namely, scattering on the neutral impurity centers has a great influence on the carrier mobility versus temperature behavior. One could note in Table 2.3, a strong increase of the concentration of neutral impurity centers with the dopant concentration (not only non-activated boron atoms contribute to the values but it is known that MBE-grown $BaSi_2$ films can contain rather high concentration of oxygen atoms [110]). Also such the trend can be noticed for the concentration of ionized impurity centers. It is interesting to trace how these values are related to the Hall carrier concentration (Fig. 2.11(a)). As seen, the charged center concentration is significantly less than the Hall carrier concentration whereas the neutral impurity center concentration has higher values as compared with the last one. Moreover the same tendency can be traced for the samples obtained on Si(111) substrates (Fig. 2.11(b)). Accounting for this discrepancy of the values one can conclude there are some other hole activation mechanisms in this compound as compared with the traditional boron activation in silicon. It is known that in complex semiconducting compounds with mixed chemical bonding, there are some carrier activation mechanisms connected with different lattice defects, deep levels, stoichiometry disorder etc.[88] Thus, the additional *p* in the systems under consideration can be defined by the following possible reasons: (1) if there are interstitial boron and/or oxygen atoms in $BaSi_2$ grains and they provide the additional impurity energy levels which are located not far from the top of the valence band;[111] (2) if there are silicon vacancies in $BaSi_2$ grains (*e.g.* it is a common situation for silicon and germanium where such the defects can be treated as acceptor centers); (3) it is interesting to note that the so-called E-centers (boron + vacancy) and A-centers (oxygen + vacancy) can be treated as the accepter centers as well.[111] Moreover after the thermal activation (annealing) such the centers become neutral. But one need to emphasize that to clarify this issue in details the additional

experimental and theoretical investigations should be performed.

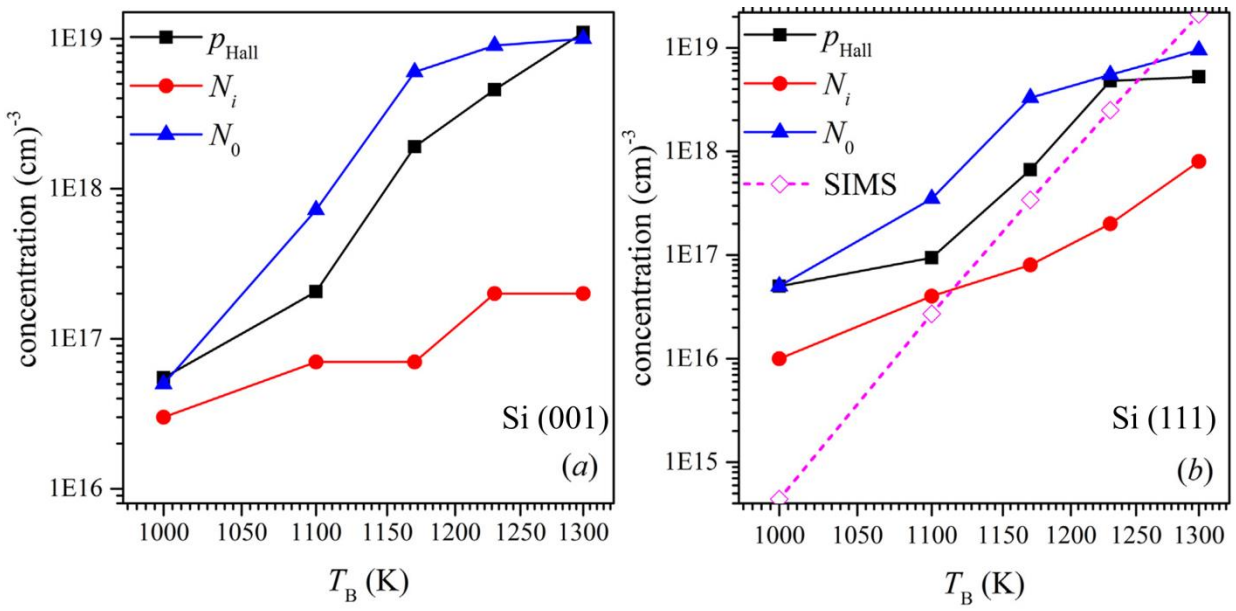

Fig. 2.11 Experimental Hall carrier concentration (P_{Hall}) for different samples of p-$BaSi_2$ films on (a) Si(001) and (b) Si(111) at RT and theoretically estimated both neutral (N_0) and charged (N_i) impurity center concentrations.

Comparison of the data on boron concentration from the SIMS analysis to the data on the charge impurity centers and the Hall carrier concentrations (Fig. 2.11(b)) for the samples B1–B5 indicates two issues. First of all, it is evident that not all the boron atoms are activated in traditional sense of a word and, secondly, there are some additional mechanisms of carrier activation which should be involved to reproduce the general tendency of the Hall carrier concentration increase. For the extremely low value of boron concentration (4.4×10^{14} cm^{-3}, the sample B1), the role of other point defects or defect complexes in $BaSi_2$ for the carrier activation is crucial. For the highest value of boron concentration (2.1×10^{19} cm^{-3}, the sample B5), it seems the effects of significant boron precipitations occur. Moreover, accounting for high oxygen concentration in the material under consideration,[110] the questions connected with preferable oxygen atom distribution (e.g. oxygen precipitations along the intergrain boundaries) also should be studied more in details.

Indeed, the inter-valley scattering can play a definite role in indirect semiconductors. Moreover, for $BaSi_2$ we can count several valleys for the electrons and holes. So some numerical estimations of the significance of the effect for $BaSi_2$ can be made. The relaxation time for the inter-valley carrier scattering is defined as [112]

$$\frac{1}{\tau_{iv}} = \omega_2 \cdot \frac{\left(\sqrt{\frac{E}{kT_i}+1} + \exp\left(\frac{T_i}{T}\right) \cdot \sqrt{\frac{E}{kT_i}-1}\right)}{\exp\left(\frac{T_i}{T}\right) - 1}, \tag{2.9}$$

where $\omega_2 = \omega_1 \cdot x$, x is the number which in a common case is not obligatory an integer number, and ω_1 is expressed by [112]

$$\omega_1 = \frac{1}{l}\left(\frac{2kT_i}{m^*}\right)^{1/2} \cdot \frac{T_i}{T}, \tag{2.10}$$

in its turn T_i defines the inter-valley phonon energy as $E = kT_i$, while l is the mean free path of phonons and expressed by $l = \pi\hbar^2\rho v_s^2/(m^{*2}DkT)$.[112] Usually the T_i value is within the Debye temperature difference for the optical and the acoustic phonon branches. Then we introduce this additional carrier scattering

mechanism to the calculation scheme used in our paper devoted to the $BaSi_2$ mobility calculation. As could be expected the total mobility values was slightly decreased as shown in Figs. 2.12(a) and 2.12(b). But using the reasonable values of the new two parameters one has insignificant changes in the total mobility versus temperature behavior (within about 5%). That means to make qualitative estimations of the mobility for $BaSi_2$, it is not necessary to introduce inter-valley scattering with some new unknown parameters into consideration.

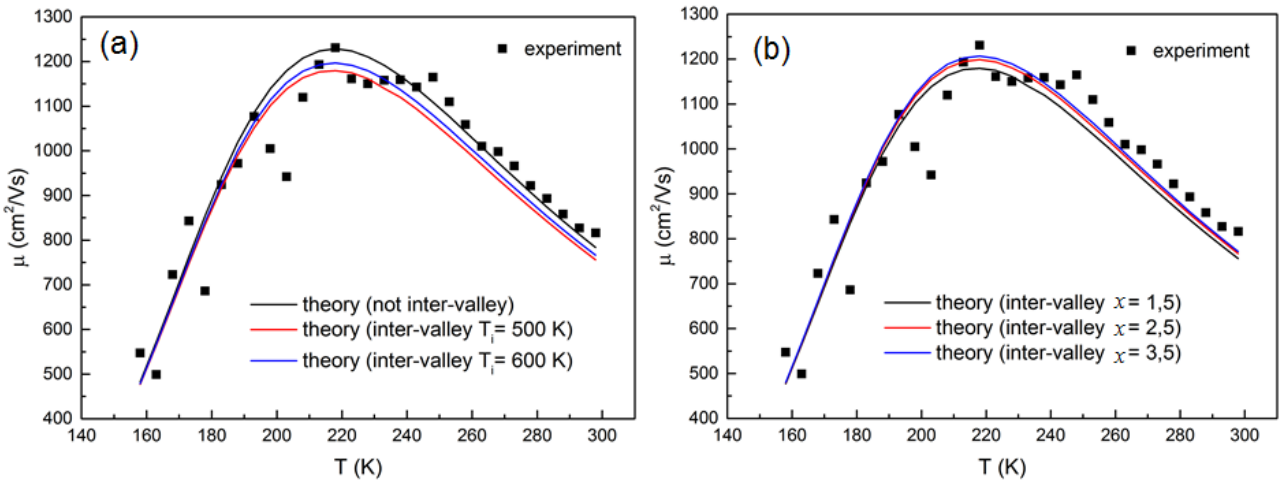

Fig. 2.12 (a) Total mobility versus temperature. Not inter-valley means the corresponding scattering mechanism was not included into consideration. The *x* value was equal to 1.5 for all the subsequent cases. (b) Same as in (a). The T_i value was equal to 500 K for all the subsequent cases.

2.5 Conclusion

The performed analysis of the experimental temperature dependence of the electron mobility in the grained polycrystalline $BaSi_2$ films with very low impurity concentrations (~ 5.0×10^{15} cm^{-3}) shows that the low temperature part *i.e.* the sharp raise of the mobility (the region I in Fig. 2.7(a)) is mainly defined by intergrain boundaries (~ 60 meV or up to twice higher) to be surpassed by the electrons. The delicate balance between intergrain boundary scattering and scattering on the phonons, the latter defines the high temperature part (the region III in Fig. 2.7(a)), results in the narrow electron mobility maximum (the region II in Fig. 2.7(a)) shifted to higher temperatures as compared with the case of monocrystalline $BaSi_2$ (which is associated with the traditional mechanisms), when intergrain boundaries are absent and scattering at low temperatures is solely defined by charge centers (Fig. 2.8(a)). To this end, the electron mobility in polycrystalline $BaSi_2$ at 300 K (to be 816 $cm^2/V{\cdot}s$) is larger than in the other semiconducting silicides. The analysis of the experimental temperature dependence of the mobility in the $BaSi_2$ films shows that the hole mobility in p-$BaSi_2$ at RT is about one order or four times smaller (depending on the Si substrate) with respect to the electron mobility in n-$BaSi_2$. Also the hole mobility values have a tendency to considerably decrease from sample to sample with increasing the dopant concentration. Such a great difference in the corresponding values of electron and hole mobility is primarily due to the specific features of electron-phonon and hole-phonon coupling. On the whole, the hole mobility versus temperature behavior is mainly defined by scattering on phonons and partly by scattering on neutral impurity centers. For device applications, where higher hole mobility values are desirable, we can suggest using $BaSi_2$ grown on Si(001) substrates rather than Si(111) ones.

Chapter 3 p-$BaSi_2$/n-Si solar cells on textured n-Si(001) with a pyramid structure consisting of {111} facets

3.1 Influence of textured structure

Surface texturing, either in combination with an anti-reflection coating or by itself, can be used to minimize reflection. Roughening of the surface reduces reflection by increasing the chances of reflected light bouncing back onto the surface, rather than out to the surrounding air. Surface texturing can be accomplished in a number of ways. A single crystalline substrate can be textured by etching along the faces of the crystal planes. The crystalline structure of silicon results in a surface made up of pyramids if the surface is appropriately aligned with respect to the internal atoms. A scanning electron microscope (SEM) photograph of a textured silicon surface is shown in Fig. 3.1(a). This type of texturing is called "random pyramid" texture, and is commonly used in industry for single crystalline wafers.[113] The textured structures have been used to trap incident light, which improves solar cell performance,[114-116] with reports of their use in thin-film silicon solar cells with a high J_{SC} of 32.9 mA/cm^2 in a single-junction μc-Si:H solar cell.[117]

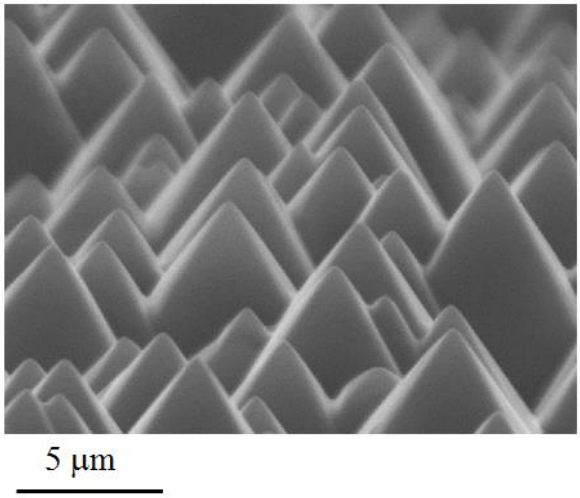

Fig. 3.1 Scanning electron microscope photograph of a textured silicon surface.[113]

We have demonstrated in chapter 1 that $BaSi_2$ shows great potential for solar cell applications. In most cases, $BaSi_2$ are grown on Si(111) substrates because the orientated *a*-axis led to a significantly smaller lattice mismatch (approximately 1%),[61] they have inactive GBs,[47,106] and a much longer *L*.[49] However, Si(001) substrates are more favorable because they are produced much more than Si(111) substrates and higher hole mobility values can be obtained using $BaSi_2$ grown on Si(001) substrates rather than Si(111) ones as we proved in chapter 2. One way to attain the above features of $BaSi_2$ even on a Si(001) substrate is to form a textured structure consisting of Si{111} facets by etching. So in this chapter, we investigated the solar cell performance of p-$BaSi_2$/n-Si heterojunction solar cells on textured n-Si(001) substrate with a pyramid structure consisting of {111} facets.

3.2 Experiments

In this experiment, the samples were prepared as follows: first, the (001) surface of a CZ n-Si(001) substrate (ρ = 1–5 Ωcm) was cleaned by acetone and methanol to eliminate organics, followed by dipping in HF/HNO_3 mixed acid. Then, the substrate was immersed into SUN-X 600 (Wako) at 75 °C for 30 min to form a pyramid structure consisting of {111} facets,[118] and cleaned by sulfuric acid at 120 °C for 15 min. After thermal cleaning of the substrate, Ba was deposited at 500 °C to form a 5 nm-thick $BaSi_2$ epitaxial template by RDE. This template acted as a seed crystal for the growth of the subsequent layer. Then, Ba and Si were co-deposited on the template at 580 °C using MBE to form a $BaSi_2$ epitaxial film that was approximately 400 nm-thick (sample D1). For comparison, another 400 nm-thick $BaSi_2$ epitaxial film was prepared on a flat Si(111) substrate (sample D2). The reflectance spectra of samples D1 and D2 were compared.

B-doped p-$BaSi_2$/n-Si solar cells with d ranging from 20−125 nm were grown with different sets of B K-cell temperature (T_B) and substrate temperature (T_S). (T_B, T_S) were set at (1230 ℃, 600 ℃), (1230 ℃, 650 ℃), and (1300 ℃, 650 ℃). After that, a 3 nm-thick a-Si capping layer was prepared at T_S = 180 ℃ over the $BaSi_2$ layers for all the samples to prevent oxidation of $BaSi_2$. The detailed parameters are shown in Table 3.1.

Table 3.1 Growth conditions of samples.

Sample No.	Substrate	RDE			MBE					
		T_{sub} [°C]	R_{Ba} [nm/min]	Time [min]	T_{sub} [°C]	R_{Ba} [nm/min]	R_{Si} [nm/min]	T_B [°C]	Time [min]	Thickness [nm]
D1	Textured CZ n-Si(001) ρ = 1 – 5 Ωcm	500	1	5	600	2.56	0.9	-	300	400
D2	Flat CZ n-Si(111) ρ = 1 – 5 Ωcm									
E1	Textured CZ n-Si(001) ρ = 1 – 5 Ωcm				600	2.56	0.9	1230	12	20
E2									30	50
E3									45	75
E4									60	100
E5									75	125
E6									300	400
F1					650	2.56	0.9	1230	12	20
F2									30	50
F3									45	75
F4									60	100
F5									75	125
G1					650	2.56	0.9	1300	12	20
G2									30	50
G3									45	75
G4									60	100
G5									75	125

Pole-figure X-ray diffraction (XRD; RIGAKU, Smart Lab) measurements were performed on sample D1 at 2θ = 62.42 ° to determine whether the *a*-axis was normal to the {111} facets. The diffraction angle 2θ = 62.42 ° allowed for the detection of x-ray diffraction caused by a $BaSi_2$ 600 plane. We also derived the *a*-axis lattice constant (*a*) of $BaSi_2$ in sample D2 by using the Nelson-Riely relationship [119] with the angle of the sample surface χ fixed at 54.7 ° with respect to the horizontal plane. The angle χ = 54.7 ° corresponds to the angle between Si(001) and (111) faces. For optical characterizations, 80 nm-thick ITO electrodes with a diameter of 1 mm were sputtered at the front side and 150 nm-thick Al was sputtered at the back side. The *J*–*V* characteristics under standard AM1.5G illumination and the photoresponse spectra were measured using a xenon lamp with a 25-cm focal-length single monochromator (Bunko Keiki, SM-1700A and RU-60N). The reflectance spectra were evaluated using an integrating sphere. Light intensity was calibrated using a pyroelectric sensor (Melles Griot 13PEM001/J). The morphology of undoped-$BaSi_2$ surface was observed by field-emission scanning electron microscopy (FE-SEM; HITACHI). Cross-sectional TEM (FEI, Tecnai Osiris) with an acceleration voltage of 200 kV was used to examine cross sections of $BaSi_2$ layers on the textured substrate. Thin foils for TEM observation were prepared with an ion beam micro-sampling system. The carrier concentrations of the samples were analyzed at RT by Hall measurements using the van der Pauw method.

3.3 Results and discussions

Figure 3.2(a) shows the schematic diagram of textured Si(001) substrate with {111} facets. SEM images of sample D1 before and after the growth of $BaSi_2$ are shown in Figs. 3.2(b)–3.2(d). Four {111} facets were observed in each pyramid (Fig. 3.2(c)), with each pyramid width being approximately 7 μm. The faces of the $BaSi_2$ were very smooth even after growing a 400 nm-thick $BaSi_2$ film (Fig. 3.2(d)). However, the four ridgelines of each pyramid and the boundaries between the pyramids were rough, which may have been caused by the coalescence of $BaSi_2$ grains grown on the adjacent Si{111} facets.

The pole-figure XRD pattern of sample D1 is shown in Fig. 3.3(b). In this measurement, we set 2θ = 62.42 ° so that the $BaSi_2$(600) diffraction can be detected, and performed φ-scan around the Si[111] for different χ values ($-90° \leq \chi \leq 90°$). Here, χ is the angle of the sample surface as shown in Fig. 3.3(a). Four diffraction peaks appear at χ = 54.7 ° as indicated by four dotted circles. This was confirmed by the φ–scan XRD pattern at χ = 54.7 °, as shown in Fig. 3.3(c). These results showed that the *a*-axis of the $BaSi_2$ was oriented normal to the textured {111} surfaces of the Si (001) substrate

The reflection spectra of samples D1 and D2 are shown in Fig. 3.4. The reflectance of sample D1 ($BaSi_2$ film on textured Si(001) substrate) was significantly lower than that of sample D2 ($BaSi_2$ film on flat Si(111) substrate) over a wide wavelength range, which indicated that light trapping was occurring. On the basis of these promising results, we fabricated and characterized a series of p-$BaSi_2$/n-Si heterojunction solar cells.

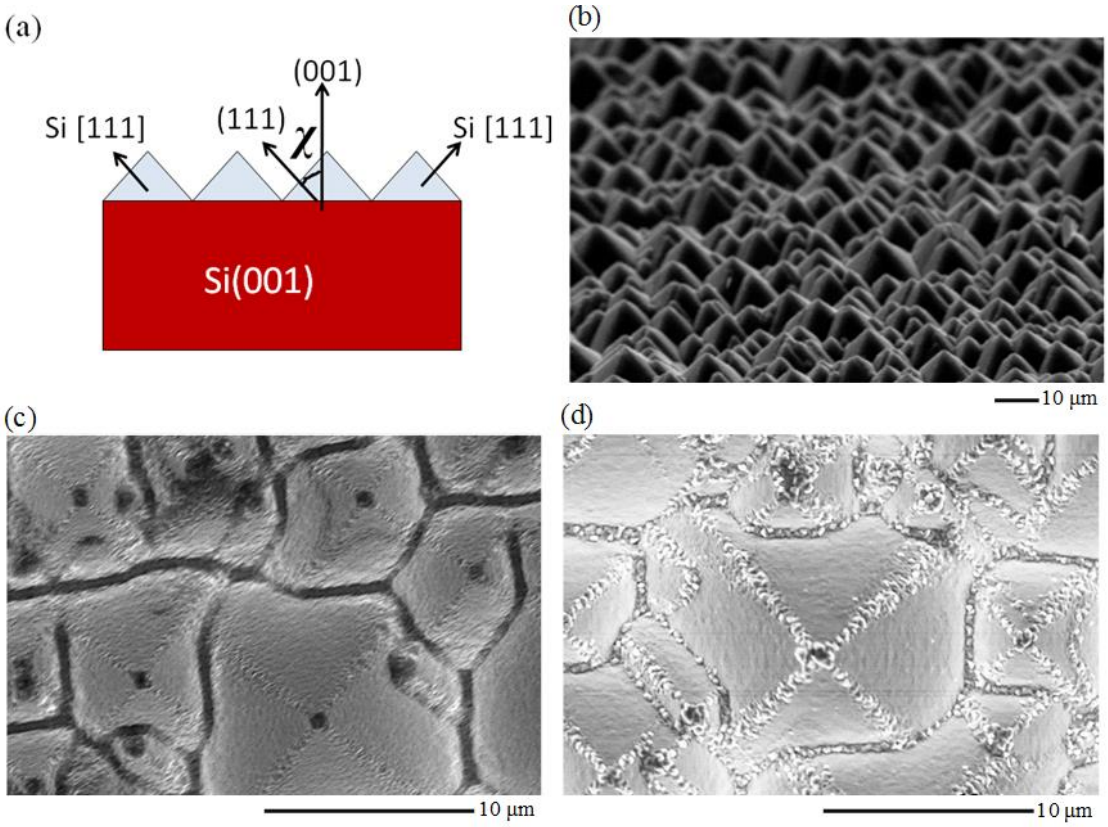

Fig. 3.2 (a) Schematic diagram of textured Si(001) with {111} facets. SEM surface images of sample D1. (b) bird's-eye view substrate, (c) top-view of the substrate, and (d) 400 nm-thick $BaSi_2$.

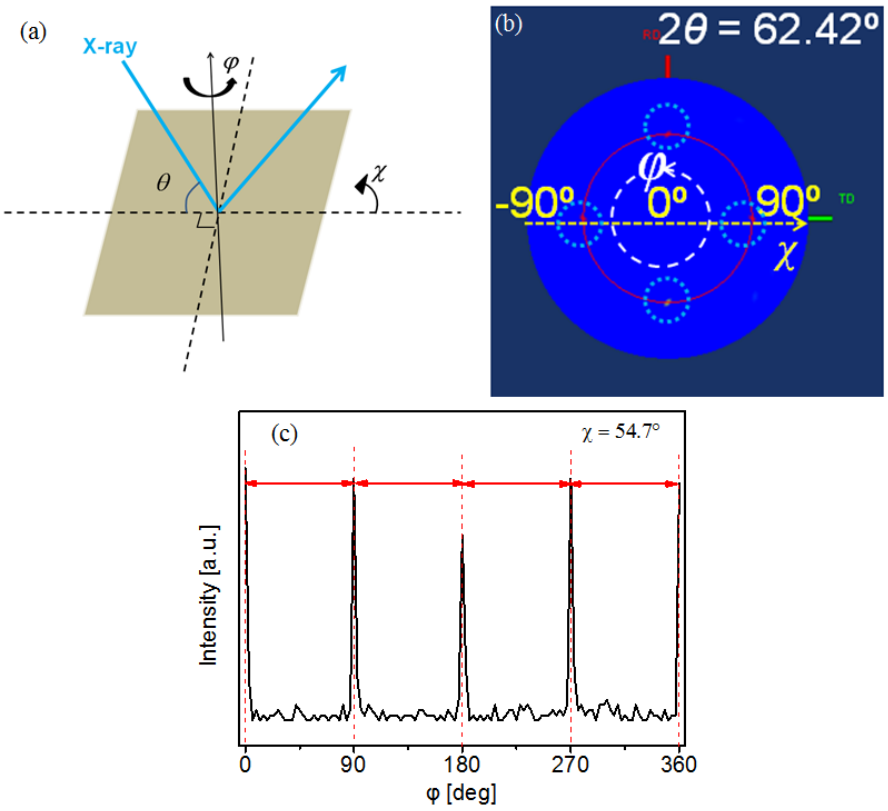

Fig. 3.3 (a) Schematic diagram of pole-figure XRD measurement. (b) Pole-figure XRD pattern of sample D1 using $BaSi_2$(600) diffraction with 2θ = 62.42 º. (c) φ-Scan XRD pattern with χ = 54.7°.

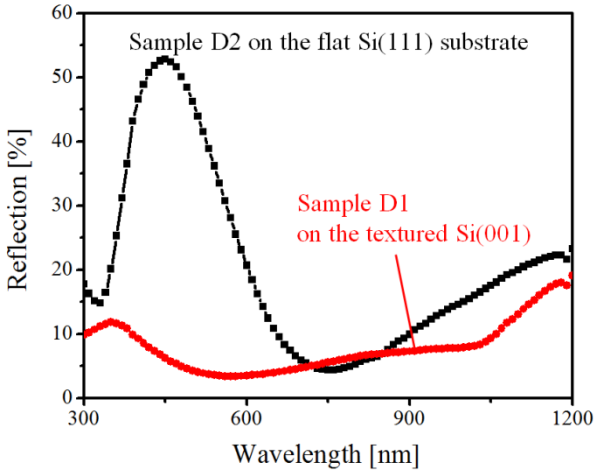

Fig. 3.4 Reflectance spectra of sample D1 (400 nm-thick undoped-$BaSi_2$ on the textured Si(001) substrate) and of sample D2 (400 nm-thick undoped-$BaSi_2$ on the flat Si(111) substrate).

Before going into the solar cells, we investigated the strain induced in the p-$BaSi_2$ layers with different d values prepared under the same growth condition with (T_B, T_S) set at (1230 ℃, 600 ℃). Fig. 3.5(a) shows the θ-2θ scan XRD patterns obtained at χ = 54.7 º. It is hard to observe any diffraction peaks of $BaSi_2$ at d = 20 nm; however, diffraction peaks of only (100)-oriented $BaSi_2$ planes, such as (200), (400), and (600) planes were obtained when d was 50 nm and above, suggesting the successful growth of highly a-axis-oriented $BaSi_2$ epitaxial films. By using these three peaks in each sample, the a-axis lattice constants were calculated. Fig. 3.5(b) is the normalized strain $\Delta a/a$ using sample D2 with the largest d. For comparison, the values of $\Delta a/a$ for $BaSi_2$ on a flat substrate were plotted. As the value of d increased from 50 to 100 nm, a decreases by approximately 0.3%, followed by a slight decrease up to d = 400 nm. This indicated that $BaSi_2$ was under compressive strain along the a axis when d < 100 nm, and the critical thickness over which $BaSi_2$ became relaxed was approximately 100 nm. Interestingly, the critical thickness increases from approximately 50 nm for $BaSi_2$ on a flat Si(111) to approximately 100 nm for $BaSi_2$ on the textured substrate. We speculate that the elastic strain energy containing in $BaSi_2$ film on the textured substrate was smaller than that on a flat substrate because the domain size of the $BaSi_2$ was limited to the area of each {111} facet. Further studies are required to gain a greater understanding of this phenomenon.

The surface morphology of a 50 nm-thick B-doped p-$BaSi_2$ on the textured Si(001) substrate, sample E2, was observed using SEM at different magnifications, as shown in Figs 3.6. The surfaces of $BaSi_2$, both on the {111} facets and on the ridgelines of the pyramids, were rough (Fig. 3.6(a)), while the magnified image (Fig. 3.6(b)) showed that $BaSi_2$ had layered growth on the facets.

A BF cross-sectional TEM image of sample E2 with a d value of 50 nm is shown in Fig. 3.7(a). Selected area electron diffraction (SAED) pattern obtained around the $BaSi_2$/Si interface area, as indicated by the red dash circle in Fig. 3.7(a), is shown in Fig. 3.7(b). The electron beam was incident along Si[1−10]. The (100)-oriented diffraction spots of $BaSi_2$, including (200), (400), and (600), were aligned with the (111)-oriented diffraction spots of Si, which indicated that the a-axis of the p-$BaSi_2$ was grown epitaxially on the {111} facet of the Si. A high-resolution TEM image near the $BaSi_2$/Si interface showed that the $BaSi_2$ film was oriented well and had formed uniformly on the Si substrate with a sharp interface (Fig. 3.7(c)). However, several steps were observed at the positions marked by the white arrows in Fig. 3.7(d) with a step height in the Si facet of approximately 6 nm. A magnified TEM image around this step is shown in Fig. 3.7(e). Defects at the steps, shown by dash red circle in Fig. 3.7(e), were observed, which may form defective centers for minority carriers. Improved etching techniques will be necessary to avoid these step structures.

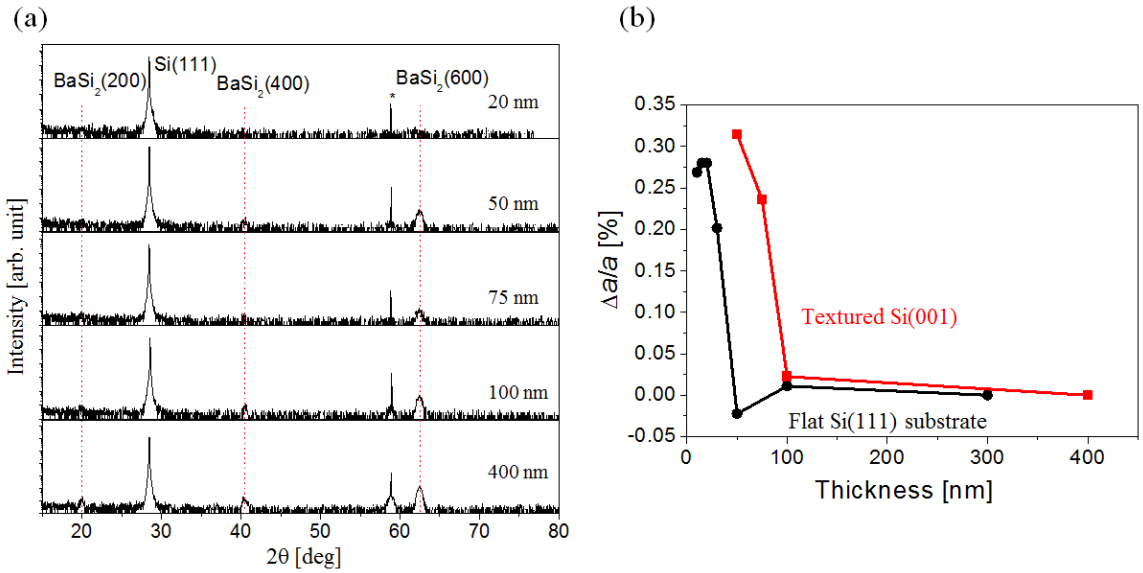

Fig. 3.5 (a) θ-2θ scan XRD spectra of B-doped p-$BaSi_2$ films with d values from 20 to 400 nm. (*) represent the diffraction peak attributed from Si substrate. (b) Normalized strain ($\Delta a/a$) as a function of d for the B-doped p-$BaSi_2$ layer on the textured Si(001) and flat Si(111) substrates.

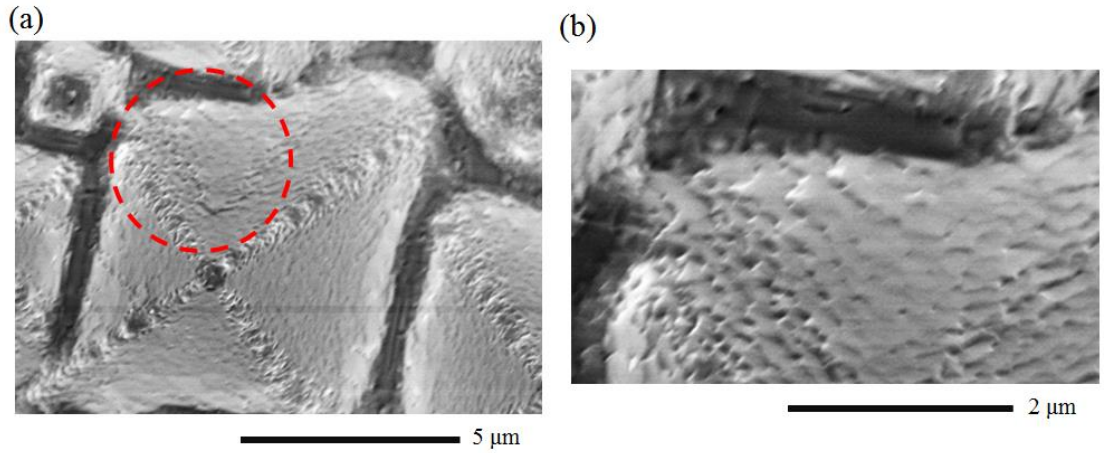

Fig. 3.6 SEM surface images of (a) 50 nm-thick B-doped p-$BaSi_2$ on the textured substrate, sample E2, and (b) a magnified image of the area marked by the red dash circle in (a).

J–*V* curves and internal quantum efficiency (*IQE*) spectra for samples E1–E6, F1–F5, and G1–G5 with different d values are shown in Figs. 3.8(a)–3.8(f). Their values of p were found to be 2.0×10^{18}, 4.6×10^{18}, and 3.6×10^{18} cm^{-3}, respectively. The best properties for each solar cell are summarized in Table 3.2. p-$BaSi_2$ (20 nm)/n-Si solar cells that were fabricated on a flat n-Si (111) substrate with an η of 9.9% [74] are shown for comparison. To accurately obtain the reverse-bias saturation current density (J_0), the shunt resistance (R_{SH}), the series resistance (R_S), and the ideality factor (γ) of the diode, we adopted a technique described in the literature.[120] Using the photodiode equation, these parameters can be given as

$$\frac{dV}{dJ} = SR_S + \frac{\gamma k_B T}{q}\left[\frac{1-(SR_{SH})^{-1}\,dV/dJ}{J + J_{SC} - (SR_{SH})^{-1}V}\right]. \tag{3.1}$$

where S is the device area, k_B is the Boltzmann constant, T is the absolute temperature, and q is the elemental charge. We can see from Figs. 3.8(a) and 3.8(b) that as the d increases from 20 to 125 nm, the solar cell

performance initially improved and then degraded with a significant decrease in J_{SC} from 28.4 to 18.8 mA/cm^2. The value of p was 2.0×10^{18} cm^{-3} in samples E1–E6. Thus, the J_{SC} reached a maximum at d = 50 nm and then decreased. The *IQE* spectra shown in Fig. 3.8(b) confirmed this.

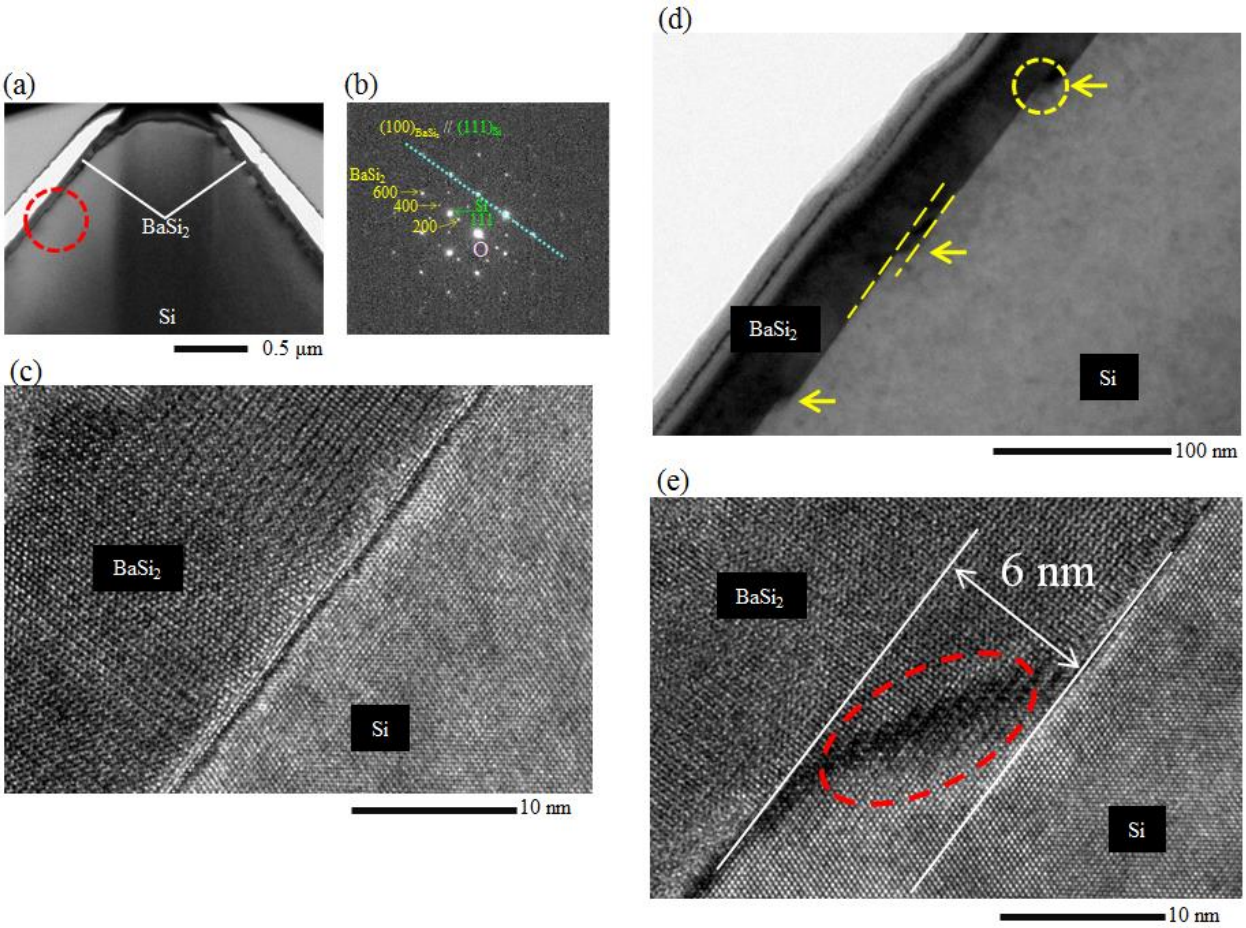

Fig. 3.7 (a) BF TEM cross sections of sample E2 near the top of the Si pyramid. (b) SAED pattern near the p-$BaSi_2$/Si interface area indicated by the red dash circle in (a). (c) High-resolution TEM image near the p-$BaSi_2$/Si interface. (d) BF TEM cross section of a step with a height of approximately 6 nm, as indicated by yellow arrows. (e) High-resolution TEM image of the area marked by a yellow dash circle in (d).

The contribution of photogenerated carriers in the p-$BaSi_2$ layer became smaller as d increased, especially in the short wavelength range. Similar results were observed for samples F1–F5 (Fig. 3.8(d)) and G1–G5 (Fig. 3.8 (f)), which indicated that as d increased, the photogenerated minority carriers (electrons) within the p-$BaSi_2$ layer were not able to efficiently reach the junction before recombination. Hence, a lower p in the p-$BaSi_2$ layer increased the contribution of p-$BaSi_2$ to the photocurrent. The value of p in samples F1–F5 was 4.6×10^{18} cm^{-3}. As d increased the η increased to a maximum of 2.7% at d = 125 nm (Fig. 3.8(c) and (d)). The *IQE* spectrum of the 75 nm-thick sample had the largest *IQE* over the whole wavelength range. Sample G1–G5 ($p = 3.6 \times 10^{18}$ cm^{-3}) exhibited a maximum η of 4.6% at d = 75 nm (Fig. 3.8(e) and (f)). Although the reflectance for the $BaSi_2$ film on the textured substrate was smaller (Fig. 3.4), the highest J_{SC} was limited to 28.5 mA/cm^2 in samples G1–G5. This value was significantly lower than that obtained for the p-$BaSi_2$/n-Si solar cells fabricated on the flat Si(111) substrate (35.2 mA/cm^2).[74] This result suggested that the minority-carrier diffusion length within the p-$BaSi_2$ and/or textured n-Si(001) had degraded. Furthermore, the values of V_{OC} in all these samples were approximately half of those observed for the devices fabricated on the flat substrate, which indicating that

the $BaSi_2$/Si interfaces was defective. We speculate that $BaSi_2$ grown around the ridgelines of each Si pyramid (Fig. 3.2(c)) and around the Si steps on the {111} facets (Fig. 3.7(e)) might be the cause of the lower J_{SC} and V_{OC} parameters. Hence, improvements in η are probable through optimization of the Si surface treatment and growth conditions of the $BaSi_2$ layer.

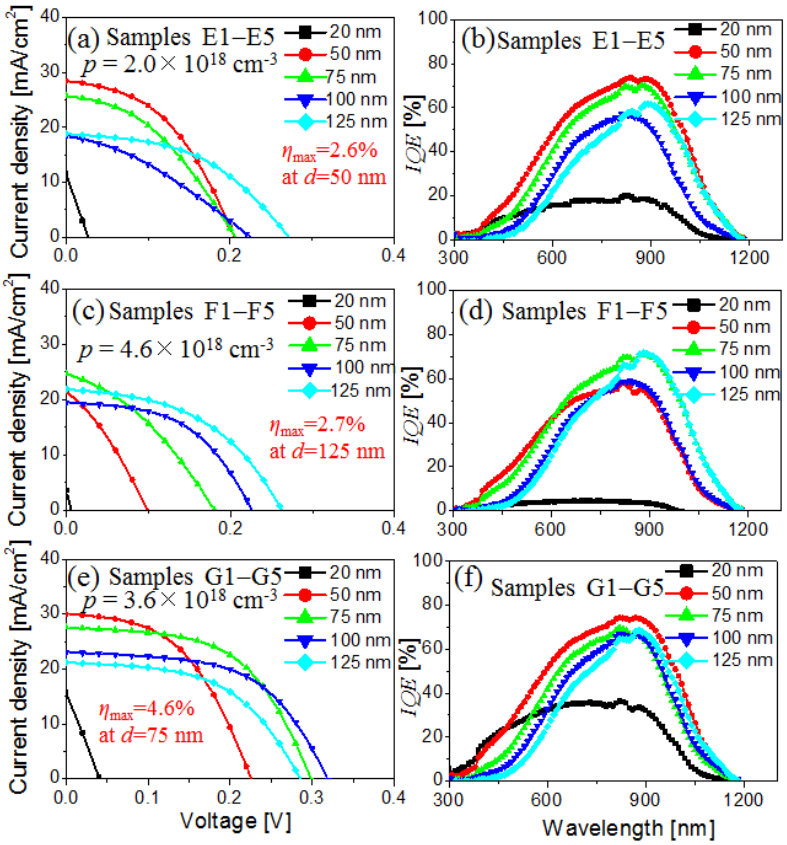

Fig. 3.8 *J–V* curves under AM1.5G illumination and *IQE* spectra of samples E1–E6 ((a) and (b)), samples F1–F5 ((c) and (d)), and samples G1–G5 ((e) and (f)).

Table 3.2 Solar cell properties of the best solar cell in each set of temperature are specified. For comparison, those of p-$BaSi_2$/n-Si solar cells on a flat Si(111) are shown.

Sample	d [nm]	J_{SC} [mA/cm^2]	V_{OC} [V]	FF [%]	η [%]	R_S [Ω]	R_{SH} [Ω]	γ	J_0 [mA/cm^2]
E2	50	28.5	0.20	44.3	2.6	209	30476	1.16	2.42×10^{-4}
F5	125	21.8	0.26	46.4	2.7	256	43182	2.65	3.15×10^{-3}
G3	75	27.6	0.30	54.9	4.6	208	61839	1.23	1.68×10^{-5}
Reference [74]	20	35.2	0.47	60.0	9.9	128	10046	1.17	1.49×10^{-5}

3.4 Conclusion

In this chapter, we successfully fabricated $BaSi_2$ films on the textured Si(001) substrate with {111} facets.

Epitaxial growth of the $BaSi_2$ layers was confirmed using XRD and TEM. The critical thickness of $BaSi_2$ was approximately 100 nm, which is much larger than that for $BaSi_2$ on a flat Si(111) substrate (50 nm). The reflectance of $BaSi_2$ on the textured substrate was lower than that on the flat substrate, which indicated that light-trapping took place. p-$BaSi_2$/n-Si solar cells with d values between 20 and 125 nm and p values between 2.0×10^{18} and 4.6×10^{18} cm^{-3} were fabricated. A maximum η of 4.6% was observed at d = 75 nm.

Chapter 4 p-$BaSi_2$/n-Si solar cells on flat n-Si(001) substrate

4.1 Background

We have reported the utilization of B-doped p-$BaSi_2$ as an emitter layer in p-$BaSi_2$/n-Si heterojunction solar cells, and achieved η of 9.9% and 4.6% on a flat n-Si(111) substrate and a textured n-Si(001) substrate, respectively.[74,77,78,121] The 9.9% is the highest η ever recorded for solar cells fabricated with semiconducting silicides. And we have found that η was improved significantly by capping the p-$BaSi_2$ surface with an approximately a 3 nm-thick a-Si layer. These findings led to the recent success of $BaSi_2$ homojunction solar cells.[76] $BaSi_2$ containing solar cells are usually fabricated on Si(111) surfaces, even though the production of Si(001) substrates is far more abundant. Si(111) substrates are used because $BaSi_2$ epitaxial films on Si(111) have exhibited large τ of ~10 μs, a large L of ~10 μm, and inactive GBs.[48,50,51] $BaSi_2$ that is *a*-axis-oriented can be grown epitaxially on both Si(111) and Si(001) surfaces, although there is a significant lattice mismatch of approximately 1 and 12% between them, respectively.[61,122] However, the density of interface states at SiO_2/Si(001) surface is one order of magnitude smaller than that at SiO_2/Si(111), which makes Si(001) substrate more favorable for device fabrication. And as we discussed in chapter 2 that $BaSi_2$ films possess better transport properties than that on Si(111). Recent achievements in $BaSi_2$ on Si(001) such as large photoresponsivity and p-$BaSi_2$/n-Si solar cells have also renewed interest in $BaSi_2$ on Si(001).[69,123,124] As reported previously, the activation rate of B atoms strongly depends on T_B for B-doped p-$BaSi_2$ and affects the performance of p-$BaSi_2$/n-Si(111) solar cells. So in this chapter, to explore the potential of Si(001) substrates for p-$BaSi_2$/n-Si heterojunction and $BaSi_2$ homojunction solar cells, we fabricated p-$BaSi_2$ films with different p and d on flat Si(001) substrates to form p-$BaSi_2$/n-Si heterojunction solar cells.

4.2 Experiments

In this experiment, a CZ n-Si(001) substrate (ρ = 1–10 Ωcm) was used. In order to check the effect of p on the performances of p-$BaSi_2$/n-Si heterojunction solar cells, T_B was set at 1110 ℃ (samples H1–H6, $p = 2.1 \times 10^{17}$ cm^{-3}), 1170 ℃ (samples I1–I7, $p = 1.1 \times 10^{18}$ cm^{-3}), and 1230 ℃ (samples J1–J8, $p = 4.6 \times 10^{18}$ cm^{-3}). After that, a 3 nm-thick a-Si capping layer was prepared at T_S = 180 ℃ over the $BaSi_2$ layers for all the samples to prevent oxidation of $BaSi_2$. The detailed parameters are shown in Table 4.1.

The crystalline quality of the samples was characterized using RHEED and XRD. The out-of-plane and in-plane XRD measurements gave the *a*, *b*, and *c*-axis lattice constants (*a*, *b*, and *c*) using the Nelson-Riely relationship.[119] Sample I7 was used as a reference. Raman spectra were measured with a laser Raman spectrometer (JASCO, NRS-5100) with a frequency doubled Nd:YAG laser (532 nm). Surface morphologies were investigated using atomic force microscopy (AFM; Shimadzu SPM-9600). For optical characterization, the details have been specified in chapter 3.

Table 4.1 Growth conditions of samples H, I, and J.

Sample No.	Substrate	RDE			MBE					
		T_{sub} [°C]	R_{Ba} [nm/min]	Time [min]	T_{sub} [°C]	R_{Ba} [nm/min]	R_{Si} [nm/min]	T_B [°C]	Time [min]	Thickness [nm]
H1	CZ n-Si(001) ρ = 1–10 Ωcm	580	1	5	600	2.2	0.9	1100	30	30
H2									40	40
H3									50	50
H4									60	60
H5									70	70
H6									80	80
I1								1170	20	20
I2									30	30
I3									35	35
I4									40	40
I5									50	50
I6									60	60
I7									300	440
J1								1230	12	12
J2									20	20
J3									25	25
J4									30	30
J5									35	35
J6									40	40
J7									50	50
J8									60	60

4.3 Results and discussions

Figure 4.1 shows the θ-2θ XRD patterns, taken for samples H2, I4, and J6, for which d values were typically 40 nm. Their RHEED patterns of p-$BaSi_2$ films, observed along the Si[1-10] azimuth on Si(001) are also presented. Intense (100)-oriented diffraction peaks in the XRD patterns and sharp streaky RHEED patterns can be observed from the figure. These results indicate the epitaxial growth of B-doped $BaSi_2$ films Si(001) substrates. Similar a-axis-oriented $BaSi_2$ films were obtained for all the samples regardless of T_B.

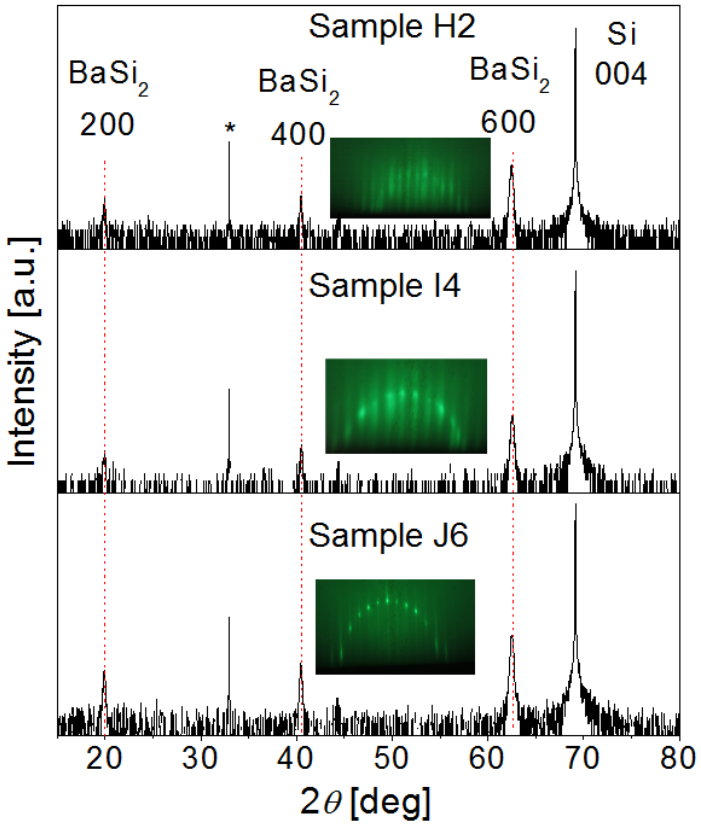

Fig. 4.1 θ–2θ XRD results of typical 40 nm-thick samples H2, I4, and J6. RHEED patterns are inserted, observed along Si [1-10]. (*) represent the diffraction peak attributed from Si substrate.

The *J*–*V* curves under AM1.5G illumination and *EQE* spectra of samples H, I, and J with different values of *d* are shown in Figs. 4.2(a)–(f). Their values of *p* were found to be 2.1×10^{17}, 1.1×10^{18}, and 4.6×10^{18} cm^{-3}, respectively. Solar cell behavior was observed for the devices fabricated on the Si(001) substrates in spite of the large lattice mismatch (~12%). The valence and conduction band offsets at the $BaSi_2$/Si interface, which is approximately 0.6 and 0.8 eV, respectively, promote the separation of photogenerated electrons and holes, as well as those in n-Si.[77] Equivalent data for p-$BaSi_2$/n-Si solar cells fabricated on Si(111) is shown in Figs. 4.2(g) and 4.2(h).[78] We can see from Figs. 4.2(a) that as the *d* increases from 30 to 80 nm, the solar cell performance initially improved and then degraded with significant decrease both in J_{SC} from 28.4 to 18.8 mA/cm^2 and V_{OC} from 0.18 to 0.36 V. The value of *p* was 2.1×10^{17} cm^{-3} in samples H. Thus, the J_{SC} reached a maximum at d = 50 nm and then decreased. The *EQE* spectra shown in Fig. 4.2(b) confirmed this. When T_B was increased to 1170 °C, with $p = 1.1 \times 10^{18}$ cm^{-3}, the solar cell performance of the devices (samples I) changed depending on the value of *d*, with the largest η (9.8%) being obtained for sample I4 (d = 40 nm). This device exhibited a J_{SC} of 37.0 mA/cm^2, a V_{OC} of 0.44 V, and a *FF* of 59.7%. The *J*-*V* curves (Fig. 4.2(c)) showed that the η improved for larger values of *d* initially, and then decreased because of a significant decrease in the J_{SC}. In addition, the V_{OC} almost saturated when $d > 30$ nm. The optimum *d* value for the p-$BaSi_2$/n-Si(111) solar cell was 20 nm (Fig. 4.2(g)). The contribution of photogenerated carriers in the p-$BaSi_2$ layer decreased, especially in the short wavelength range, with increasing values of *d* (Figs. 4.2(d) and 4.2(h)). This indicated that it was difficult for the photogenerated minority carriers (electrons) in the p-$BaSi_2$ layer to reach the junction before recombination as *d* increased. The same phenomenon was observed from Fig. 4.2(f) as well. This is attributed to a reduced *L* in the p-$BaSi_2$ films. Figure 4.3(a) presents the *EQE* spectra of p-$BaSi_2$/n-Si samples at d = 50 nm. Because α reaches 4×10^5 cm^{-1} at a wavelength of 500 nm in $BaSi_2$, a large fraction

of photons (>85%) at this wavelength are absorbed as they travel as far as 50 nm ($1/\alpha \times 2$ = 50 nm) through the p-$BaSi_2$ layer. The *EQE* values for sample on Si(001) are smaller than those on Si(111) especially in the short wavelength range, meaning that the L of the p-$BaSi_2$ on Si(001) is smaller than that on Si(111). We have already measured L values of undoped $BaSi_2$ films on Si(111) and Si(001) by an electron-beam-induced-current (EBIC) technique, and they are 10 and 1.5 μm, respectively.[125] This difference in L comes from inactive GBs of $BaSi_2$ on Si(111).[47] Although we have not evaluated L values of p-$BaSi_2$ films by EBIC, it is reasonable to consider that they are smaller for p-$BaSi_2$ on Si(001) than those on Si(111). Figure 4.3(b) shows the schematics of the band alignment of the diode simulated by automat for simulation of heterostructures (AFORS-HET).[126] The band bending occurs in the region close to the interface under illumination, marked by broken circles, and acts to disturb the transport of photogenerated electrons in the p-$BaSi_2$ to the n-Si region and photogenerated holes in the n-Si to the p-$BaSi_2$ region. This is caused by a small built-in potential of the diode (~ 0.2 V) because of a small electron affinity of $BaSi_2$ (3.2 eV).[83] Since such a band bending may limit the η of a p-$BaSi_2$/n-Si solar cell, we need to work on $BaSi_2$ homojunction solar cells to achieve much a higher η.

To accurately determine the parameters of each samples, we adopted Eq. 3.1. The solar cell properties for each solar cell are summarized in Table 4.2. For samples H, maximum η (6.2%) was obtained at 60 nm (sample H4). This value was smaller than that of samples I and J. This is due to the small B activation ratio in the $BaSi_2$ films with T_B = 1100 °C. Samples I and J have similar tendency as d increased. So we focused on samples I because an η of 9.8% was obtained for sample I4. The J_0 of samples I decreased from 0.20 mA/cm^2 at d = 20 nm to 9.04×10^{-6} mA/cm^2 at d = 40 nm, which was comparable to the J_0 obtained for the p-$BaSi_2$/n-Si solar cell fabricated on Si(111) ($J_0 = 1.39 \times 10^{-5}$ mA/cm^2) with the highest η.[78] This result highlights the promise of $BaSi_2$ solar cells fabricated on Si(001) substrates. The decrease in the η at low values of d (20 and 30 nm) was primarily caused by small *FF*s because of large R_S and small R_{SH}.

To understand this decreased η at low d we examined the surface morphologies (5 μm × 5 μm) and cross-sectional profiles of p-$BaSi_2$ layers using AFM for samples I with d = 20, 40, and 60 nm, as shown in Fig. 4.4. These morphologies were examined before the deposition of the ITO surface electrode. The sample with d = 20 nm exhibited GBs with gaps with depths of approximately 14 nm (Fig. 4.4), showing that the entire Si surface was not covered by the film. The small R_{SH} calculated for this film likely originated from current leakage paths introduced as a consequence of direct contact between the ITO and the n-Si(001) substrate. At d = 40 and 60 nm, the n-Si(001) substrate was entirely covered with p-$BaSi_2$, resulting in the smaller J_0 and larger R_{SH} values. These results clearly demonstrated that contact of ITO and p-$BaSi_2$ and contact of p-$BaSi_2$ and n-Si have significant impacts on the values of R_{SH} and J_0. Conversely, a d of 20 nm was sufficient to cover the entire n-Si(111) surface, while d = 10 nm was not enough.

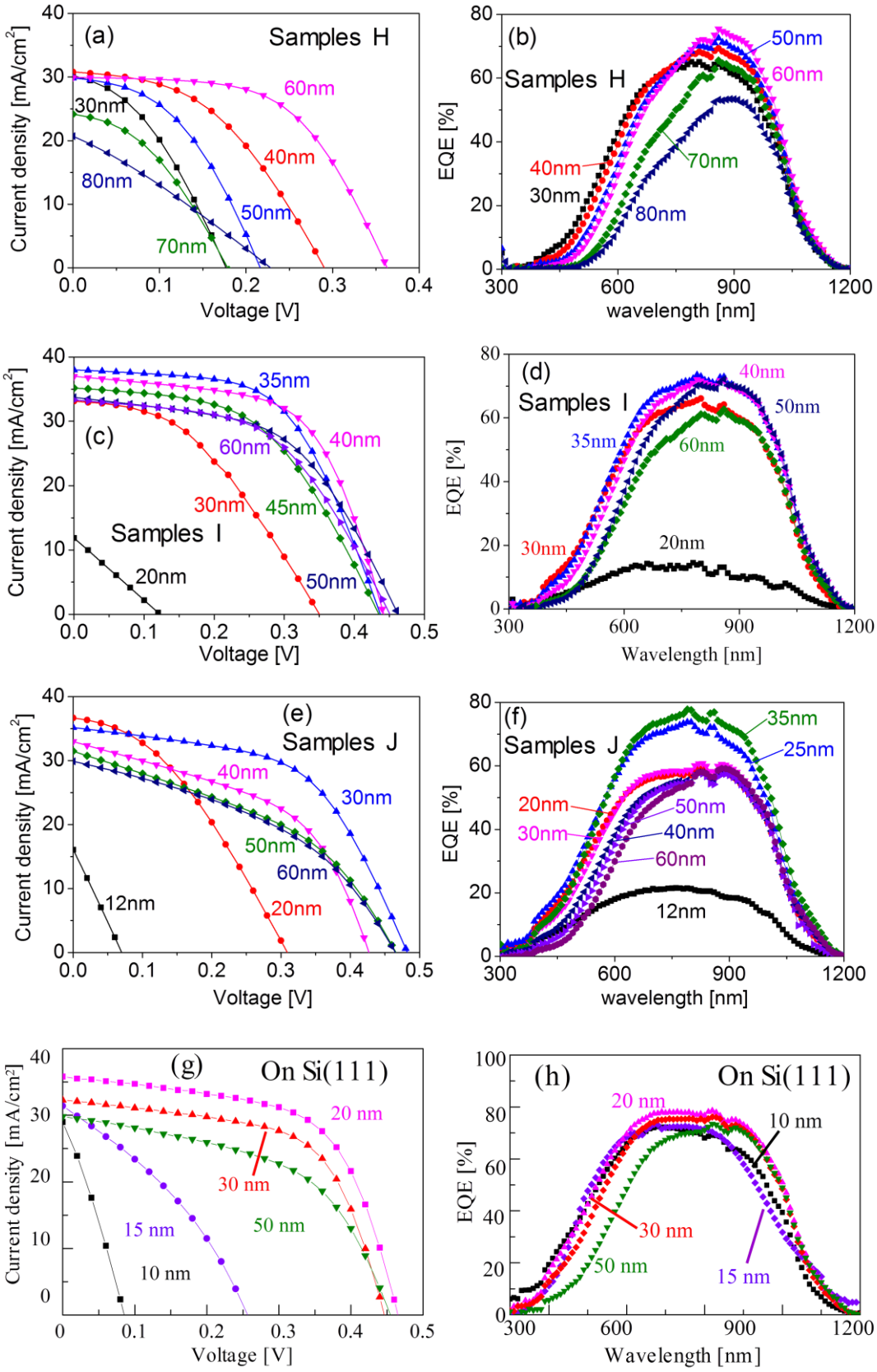

Fig. 4.2 *J-V* curves and *EQE* spectra of the samples H ((a) and (b), respectively), samples I ((c) and (d), respectively), samples J ((e) and (f), respectively), and p-$BaSi_2$/n-Si solar cells on Si(111) substrates ((g) and (h), respectively).

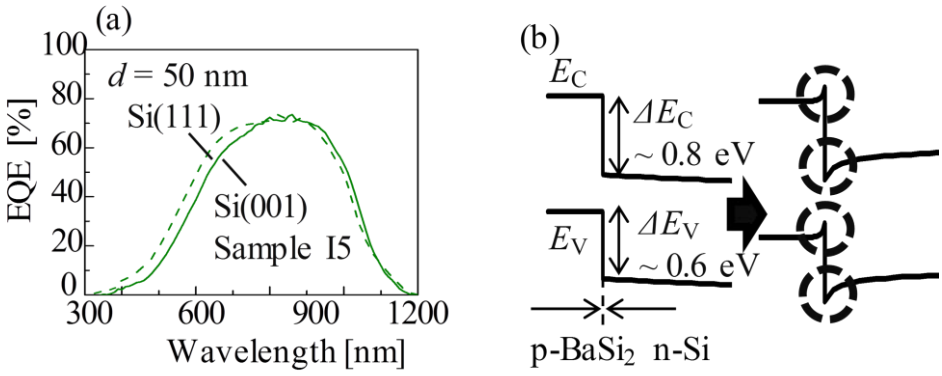

Fig. 4.3 (a) *EQE* spectra of the p-$BaSi_2$/n-Si solar cells on Si(001) and Si(111) substrates at d =50 nm in Fig. 4.2(d) and 4.2(h). (b) Schematics of calculated band alignments of a p-$BaSi_2$ (50 nm)/n-Si solar cell during short-circuit condition (left) and open-circuit condition (right) by AFORS-HET.

Table 4.2 Solar cell properties of the p-$BaSi_2$/n-Si solar cell for samples H, I, J, and those on Si(111).

Sample	p [cm^{-3}]	d [nm]	J_{SC} [mA/cm^2]	V_{OC} [V]	FF [%]	η [%]	R_S [Ω]	R_{SH} [Ω]	γ	J_0 [mA/cm^2]
H1	2.1×10^{17}	30	30.2	0.18	37.7	2.0	283	20414	1.40	1.65×10^{-3}
H2		40	30.8	0.29	44.7	4.0	327	82719	1.32	3.72×10^{-5}
H3		50	29.8	0.22	43.3	2.8	212	37031	1.59	4.2×10^{-4}
H4		60	29.9	0.36	56.7	6.2	285	113739	1.39	1.06×10^{-5}
H5		70	24.2	0.18	39.3	1.7	347	106157	1.12	4.60×10^{-4}
H6		80	20.7	0.23	28.3	1.3	890	57328	1.03	3.40×10^{-4}
I1	1.1×10^{18}	20	11.85	0.12	25	0.4	1247	1385	0.89	0.2045
I2		30	33.2	0.35	39.8	4.6	420	15801	1.36	1.83×10^{-4}
I3		35	37.98	0.44	57.0	9.5	289	34244	1.73	1.58×10^{-5}
I4		40	37.01	0.44	59.7	9.8	207	14778	1.67	9.04×10^{-6}
I5		50	33.14	0.46	53.9	8.28	379	13288	1.80	1.64×10^{-5}
I6		60	33.3	0.45	51.8	7.79	393	17450	1.96	3.61×10^{-5}
J1	4.6×10^{18}	12	16.1	0.07	25.1	0.3	312	582	0.85	2.1×10^{-4}
J2		20	36.7	0.31	37.3	4.2	424	50351	1.25	2.95×10^{-5}
J3		25	38.34	0.43	51.1	8.4	221	10615	1.69	5.08×10^{-6}
J4		30	35.2	0.48	54.3	9.2	210	11126	1.86	2.23×10^{-6}
J5		35	38.27	0.46	46.3	8.3	336	5541	1.52	3.06×10^{-6}
J6		40	33.0	0.43	47.9	6.8	217	4664	1.96	3.96×10^{-5}
J7		50	31.5	0.47	41.1	6.0	395	4197	1.82	1.45×10^{-5}
J8		60	29.9	0.47	41.7	5.8	427	9284	1.86	1.62×10^{-5}
Reference [78]	2.0×10^{18}	10	28.9	0.09	0.29	0.7	154	2900	1.63	9.65
		15	32.8	0.35	0.51	5.9	264	17471	2.0	1.28×10^{-1}
		20	35.8	0.47	0.6	9.9	163	17717	1.11	1.39×10^{-5}
		30	32.3	0.45	0.6	8.7	159	13523	1.38	3.55×10^{-4}
		50	29.8	0.45	0.51	7	314	11394	1.31	9.12×10^{-4}

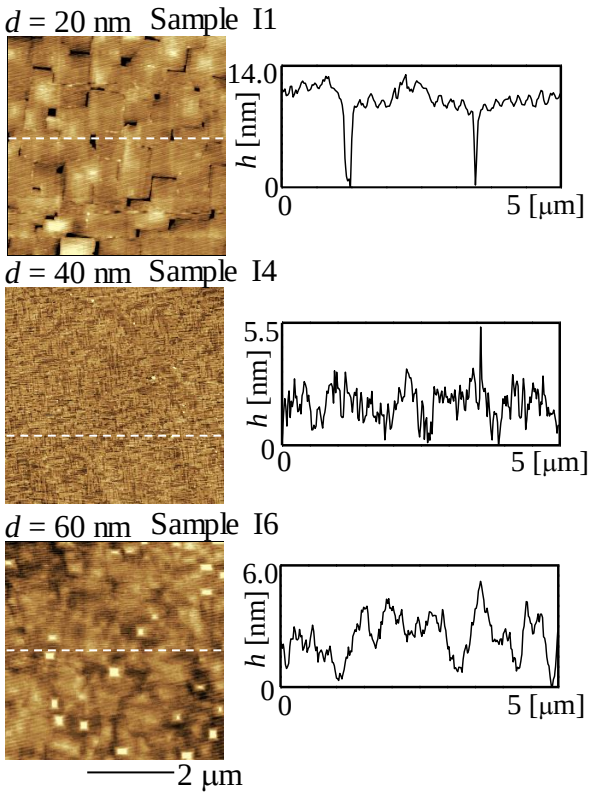

Fig. 4.4 AFM images (5 μm × 5 μm) and cross-sectional profiles (along the white line) of p-$BaSi_2$ layers from samples I1 (20 nm), I4 (40 nm), and I6 (60 nm).

The strains ($\Delta a/a$, $\Delta b/b$, and $\Delta c/c$), normalized using those of a reference sample with d = 440 nm, as functions of d on the Si(001) substrate are shown in Fig. 4.5(a). The equivalent graphs obtained on Si(111) substrates are presented in Fig. 4.5(b).[83] Surprisingly, the values of $\Delta a/a$, $\Delta b/b$, and $\Delta c/c$ were all negative when d was equal to or smaller than 60 nm. Their magnitude decreased monotonically and approached 0, which indicated that the $BaSi_2$ films were under compressive strain. In contrast, $\Delta a/a$ on the Si(111) substrate was positive and the dependence of the strain on d was more complicated (Fig. 4.5(b)). It is plausible that these differences in strain caused the different thicknesses of the p-$BaSi_2$ layer required to cover the entire n-Si surface when comparing Si(111) and Si(001) substrates. Raman spectra of the p-$BaSi_2$ films on the Si(001) substrate with different d values are shown in Fig. 4.5(c). Five Raman peaks were observed at wavenumbers below 500 cm^{-1},[104] denoted by F_g, E_g, $E_g + F_g$, F_g, and A_g, in addition to an intense peak (520.2 cm^{-1}) caused by the transverse optical phonon of Si (Si_{TO}) from the substrate. The Raman peaks F_g, E_g, and A_g originated from tetrahedral Si with T_h symmetry in the lattice of $BaSi_2$.[127] The peak positions in the Raman spectra as functions of d are shown in Fig. 4.5(d). As d increased, all peaks shifted to a smaller wavenumbers, which indicated that the films were under compressive stress in the in-plane direction.[128] This compressive stress was consistent with the strains ($\Delta b/b < 0$ and $\Delta c/c < 0$) when considering the elastic stiffness constants of $BaSi_2$ using the elastic stress-strain relationship described by M. Grundmann.[129] As the Si p state appears dominant in the valence band maximum of $BaSi_2$ in both theory [42,43,130]and experiment,[131] it is possible that the stress introduced in the tetrahedral Si within the lattice modified the band structure of $BaSi_2$, leading to differences in its optical properties. Although further studies are required to verify the relationship between the induced stress and optical properties of $BaSi_2$, this work shows that Si(001) substrates are useful for $BaSi_2$ solar cells.

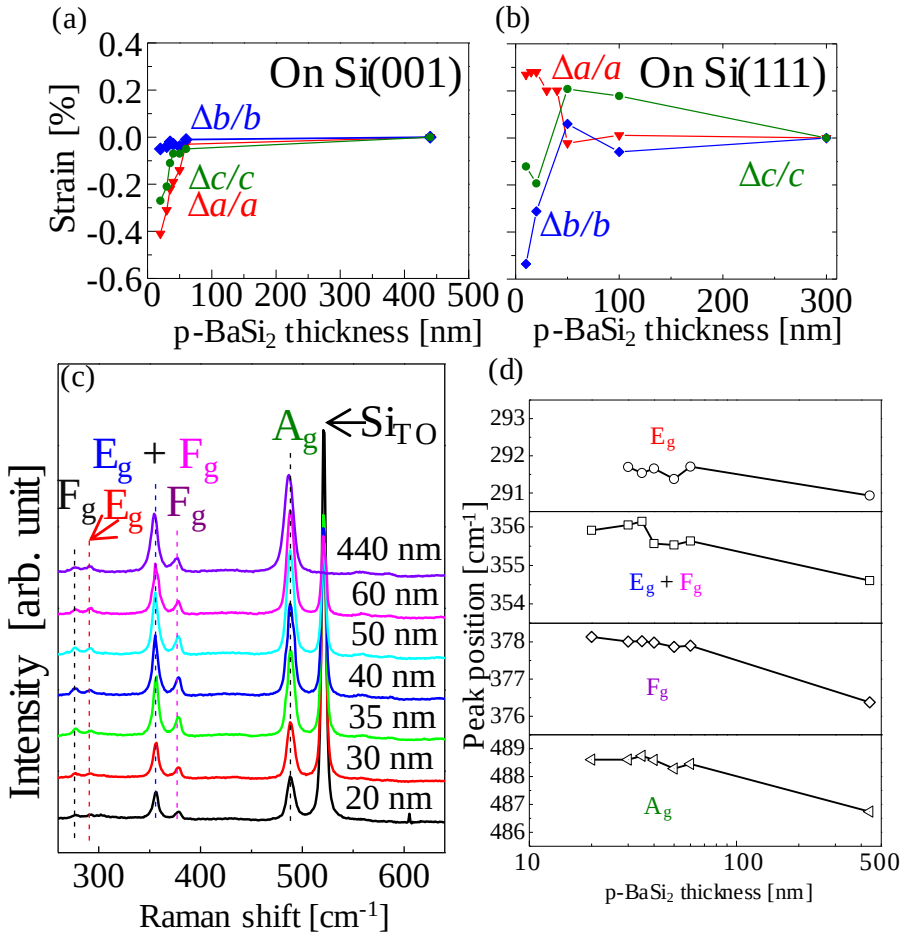

Fig. 4.5 Normalized strains ($\Delta a/a$, $\Delta b/b$, and $\Delta c/c$) as functions of p-$BaSi_2$ thickness grown on (a) Si(001) (samples I) and (b) Si(111).[83] (c) Raman spectra of samples I. (d) Raman peak positions as functions of thickness for the p-$BaSi_2$ films.

4.4 Conclusion

In this chapter, we fabricated B-doped p-$BaSi_2$/n-Si heterojunction solar cells on Si(001) substrates with different p-$BaSi_2$ layer thicknesses. We then examined the influence of the p-$BaSi_2$ layer thickness and p on the solar cells properties. The p-$BaSi_2$ films were found to be under compressive strain in the normal direction and compressive stress in the in-plane direction when $d < 60$ nm. The η reached a maximum value of 9.8% with a J_{SC} of 37.0 mA/cm^2, a V_{OC} of 0.44V, and a FF of 59.7% with a thickness of 40 nm and a p of 1.1×10^{18} cm^{-3} for p-$BaSi_2$. These values were comparable to those obtained for devices fabricated on Si(111), indicating that Si(001) substrates can also be used for $BaSi_2$ solar cells.

Chapter 5 Characterization of $BaSi_2$ films on a p^+-$BaSi_2$/p^+-Si tunnel junction

5.1 Background

In chapter 4, we demonstrated the potential of $BaSi_2$ films for solar cell applications. One of the critical steps in the fabrication of $BaSi_2$ films on Si is to produce an electrical contact between the Si and $BaSi_2$. There are large conduction and valence band discontinuities at the $BaSi_2$/Si heterointerface, due to the much smaller electron affinity of $BaSi_2$ (3.2 eV) compared to that of Si.[73] Therefore, even when light is incident on the $BaSi_2$/Si structure, and photoexcited carriers are generated in the $BaSi_2$ layer, they will be blocked at the $BaSi_2$/Si interface, thereby significantly decreasing the photocurrent. There are some investigations on employing a TJ to overcome this problem.[79,132] Saito *et al.* used an Sb-doped n^+-$BaSi_2$/p^+-Si TJ to serve $BaSi_2$ epitaxial films, and a current density of 21.9 A/cm^2 was achieved at 0.5 V.[80] Du *et al.* fabricated 400 nm-thick undoped-$BaSi_2$ epitaxial layers on a n^+-$BaSi_2$/p^+-Si TJ, and an *IQE* exceeding 70% at 1.55 eV were achieved.[82] The most proper dopant to form n^+-$BaSi_2$ is Sb, however, the diffusion of Sb atoms within $BaSi_2$ films may decrease their crystal qualities and affect the transport of carriers.[133] Our final goal is the fabrication of high-η $BaSi_2$/c-Si tandem solar cells. In this chapter, prior to the formation of a $BaSi_2$/c-Si tandem solar cell, we aimed to form a p^+-$BaSi_2$/p^+-Si TJ, which is necessary to make the electrical contact between $BaSi_2$ and c-Si solar cells sufficiently small.

5.2 Experiments

The solar cell characteristics and key parameters such as band alignment, *J-V* characteristics and suitable thickness of each layer were determined using the AFORS-HET simulation. To make a p^+-$BaSi_2$/p^+-Si TJ, *p* values should be set to exceed the effective density of states in the valence band for $BaSi_2$ (2.0×10^{19} cm^{-3}) and Si (1.04×10^{19} cm^{-3}). First, we fabricated B-doped p-Si layers, named K1–K6, as details specified in Table 5.1. The *p* values were confirmed by Hall measurement. After confirming the growth condition of p^+-Si, we formed the TJ on two different substrates with ρ values of 2–5 Ωcm and 0.07 Ωcm, named L1 and L2, respectively, as list in Table 5.2, and checked their TJ properties by *J–V* characteristics. Afterwards, $BaSi_2$ films were grown on the TJ, and the crystalline quality, surface morphology and photoresponse spectra were measured. Table 5.3 shows the growth conditions of samples M1 and M2. For AFM measurement, optical and electrical characterization, the details have been specified in Chapter 3.

Table 5.1 Growth conditions of samples K1–K6.

Sample	Substrate	MBE				
		T_{sub} [°C]	R_{Si} [nm/min]	T_B [°C]	Time [min]	Thickness [nm]
K1	FZ n-Si(001) ρ > 1000 Ωcm	400	0.9	1300	120	98
K2		450				111
K3		500				111
K4		550				99
K5		600				112
K6		700				98

Table 5.2 Growth conditions of samples L1 and L2.

Sample	Substrate	MBE (p^+-Si)				
		T_{sub} [°C]	R_{Si} [nm/min]	T_B [°C]	Time [min]	Thickness [nm]
L1	CZ p-Si(001) ρ = 2–5 Ωcm	500	0.9	1300	48	40
L2	CZ p-Si(001) ρ = 0.07 Ωcm					

RDE			MBE (p^+-$BaSi_2$)						a-Si capping layer [nm]
T_{sub} [°C]	R_{Ba} [nm/min]	Time [min]	T_{sub} [°C]	R_{Si} [nm/min]	R_{Ba} [nm/min]	T_B [°C]	Time [min]	Thickness [nm]	
580	1	5	650	0.9	2.56	1300	7	10	3

Table 5.3 Growth conditions of samples M1 and M2.

Sample	Substrate	MBE (p^+-Si)					RDE		
		T_{sub} [°C]	R_{Si} [nm/min]	T_B [°C]	Time [min]	Thickness [nm]	T_{sub} [°C]	R_{Ba} [nm/min]	Time [min]
M1	CZ p-Si(001) ρ = 2–5 Ωcm	500	0.9	1300	48	40	580	1	5
M2	CZ p-Si(001) ρ = 0.07 Ωcm								

MBE (p^+-$BaSi_2$)						MBE (p-$BaSi_2$)					
T_{sub} [°C]	R_{Si} [nm/min]	R_{Ba} [nm/min]	T_B [°C]	Time [min]	Thickness [nm]	T_{sub} [°C]	R_{Si} [nm/min]	R_{Ba} [nm/min]	T_B [°C]	Time [min]	Thickness [nm]
650	0.9	2.56	1300	7	10	600	0.9	2.2	1200	300	500

MBE (n- $BaSi_2$)						a-Si capping layer [nm]
T_{sub} [°C]	R_{Si} [nm/min]	R_{Ba} [nm/min]	T_{Sb} [°C]	Time [min]	Thickness [nm]	
500	0.9	2.2	350	1	10	3

5.3 Results and discussions

First we did some work on simulation. Figures 5.1(a) and 5.1(b) show the schematic diagram and the band alignment of an optimized n-$BaSi_2$(10 nm, $n = 2 \times 10^{19}$ cm^{-3})/p-$BaSi_2$(500 nm, $p = 1 \times 10^{17}$ cm^{-3})/p^+-$BaSi_2$(10 nm, $p = 2 \times 10^{19}$ cm^{-3})/p^+-Si (40 nm, $p = 4.3 \times 10^{19}$ cm^{-3})/p-Si(500 μm, ρ = 2–5 Ωcm) solar cell, respectively. From Fig. 5.1(b), the electron-hole pairs generate in the absorber p-$BaSi_2$ region, afterwards, electrons transport toward the n-$BaSi_2$ side by the build-in electric field and holes transport to the p-Si side across the p^+-$BaSi_2$/p^+-Si TJ, leading to the operation of the solar cell.

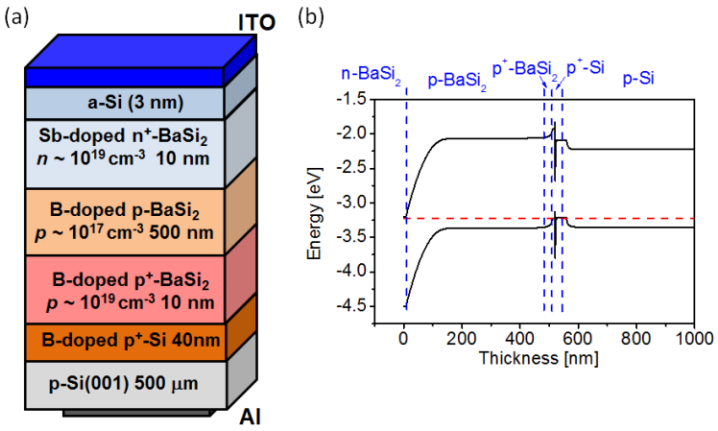

Fig. 5.1 (a) Schematic diagram and (b) band alignment of $BaSi_2$ films on a p^+-$BaSi_2$/ p^+-Si TJ.

Figure 5.2 shows the simulated *J-V* characteristics of the optimized solar cell in the dark and under standard AM1.5G illumination. Good rectifying properties were achieved and an η of 16.5% was obtained with a V_{OC} of 0.76 V, J_{SC} of 25.8 mA/cm^2 and *FF* of 83.9%.

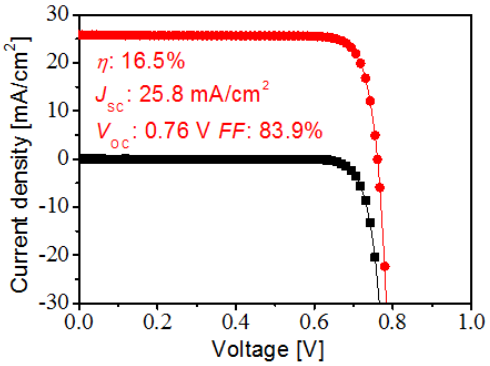

Fig. 5.2 *J-V* characteristics of the optimal solar cell in the dark (black) and under standard AM1.5G illumination (red).

Figures 5.3(a)–(f) show the RHEED patterns and surface morphologies, measured by AFM, of samples K1–K6, respectively. As we can see that when T_{sub} was 400 °C, halo RHEED pattern appeared, indicating that amorphous Si was formed at such low T_{sub}. When T_{sub} was increased to > 450 °C, streaky and/or spots in RHEED patterns were observed. For samples K5 and K6, the surfaces were quite rough from AFM results, and spots in RHEED patterns confirmed it. Such rough surfaces were not good for the subsequent growth of $BaSi_2$ epitaxial films. For samples K2 and K4, streak and spots in RHEED patterns proved that the surfaces were rougher than that of sample K3 (Fig. 5.3(c)).

Despite the surface morphology, the *p* is another key parameter that we need to consider. Figures 5.4(a) and 5.4(b) show substrate temperature dependence of (a) hole concentration and (b) hole mobility, respectively. B-doped Si layer showed n-type conductivity for sample K1 with an *n* value of 1.8×10^{16} cm^{-3} at T_{sub} = 400 °C. This was due to the inactive doping of B atoms in a-Si layer.[134] For samples K2–K6, p-type conductivity was confirmed for B-doped Si films. The *p* decreased with increasing T_{sub}. In order to form p^+-Si layer, the obtained *p* should be larger than the effective density of states in the valence band for Si (1.04×10^{19} cm^{-3}). So T_{sub} should be set below 700 °C. Associating with the RHEED and AFM results as shown in Figs. 5.3(a)–5.3(f), and sample K3 had the best surface morphology and suitable *p* values of 4.6×10^{19} cm^{-3} to serve as p^+ layer.

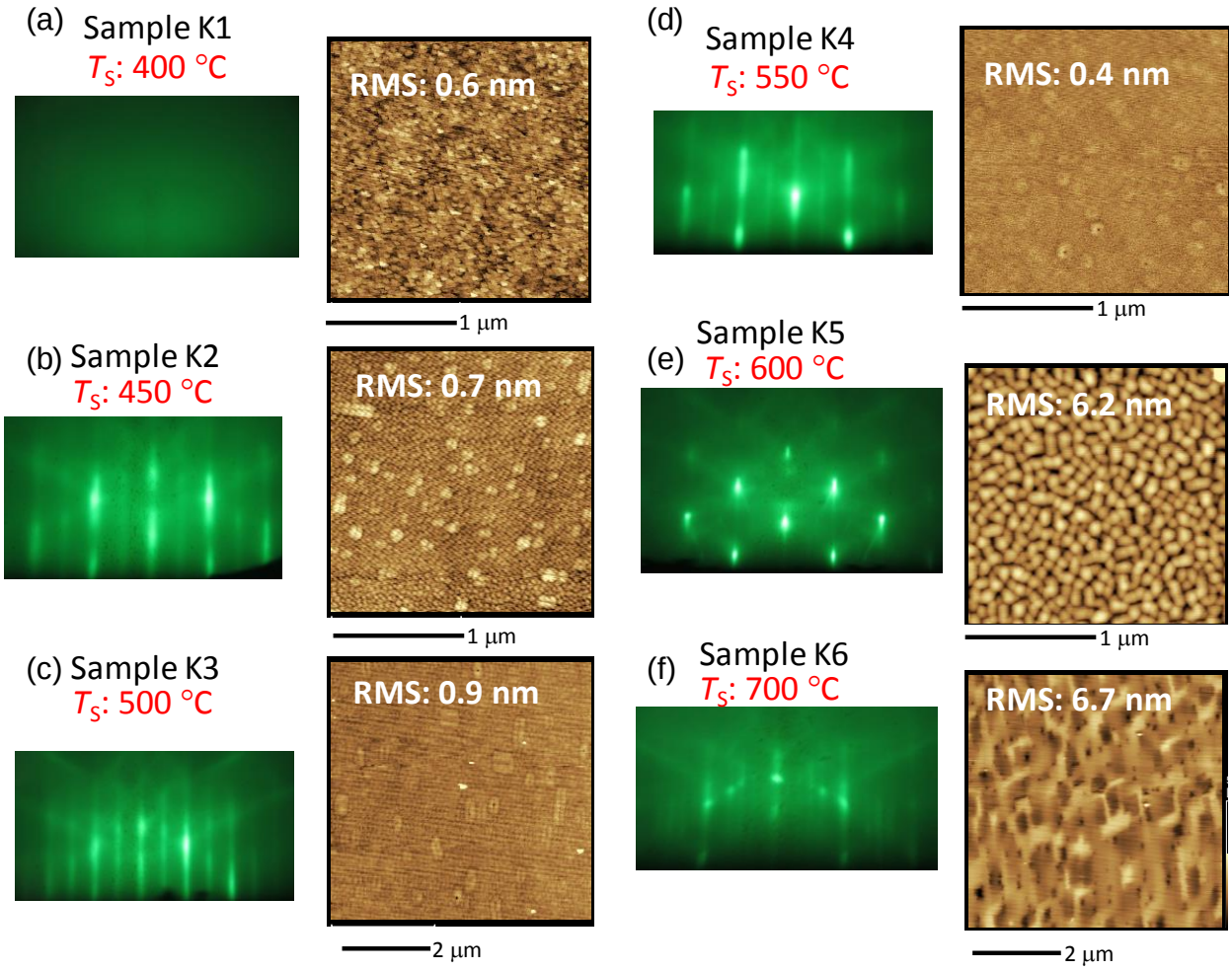

Fig. 5.3 RHEED patterns and AFM results of samples K1–K6.

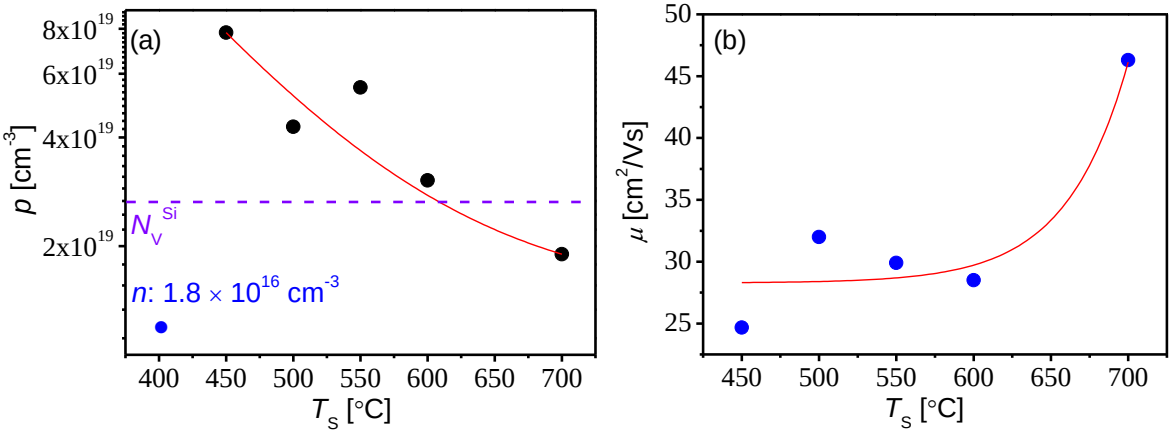

Fig. 5.4 Substrate temperature dependence of (a) hole concentration and (b) hole mobility.

After confirming the growth of p^+-Si, we next moved to the characterization of p^+-$BaSi_2$/p^+-Si TJ. Figures 5.5(a) shows the schematic diagram of *J*–*V* measurement, V_{bias} was applied to the p^+-$BaSi_2$ layer with respect to the bottom p-Si substrate. According to the AFM results shown in Fig. 5.5(b), both of the 2 samples had smooth surfaces, which were good for the subsequent growth of $BaSi_2$ epitaxial films. Figure 5.5(c) shows the

J-V characteristics of samples L1 and L2. The nearly linear behavior of samples L1 and L2, indicates that the sample works like a constant resistance under the V_{bias}. Even under a very small V_{bias}, the carriers could still tunnel through the p^+-$BaSi_2$/ p^+-Si TJ without being blocked. And the tunnel current density reached 18.3 A/cm^2 at a V_{bias} = 1.0 V for sample L2. Sufficiently small TJ resistance of 0.081 Ωcm^2 was achieved. Moreover, sample L1, grown on a medium resistive p-Si substrate, also showed sufficient small TJ resistance around 0 V.

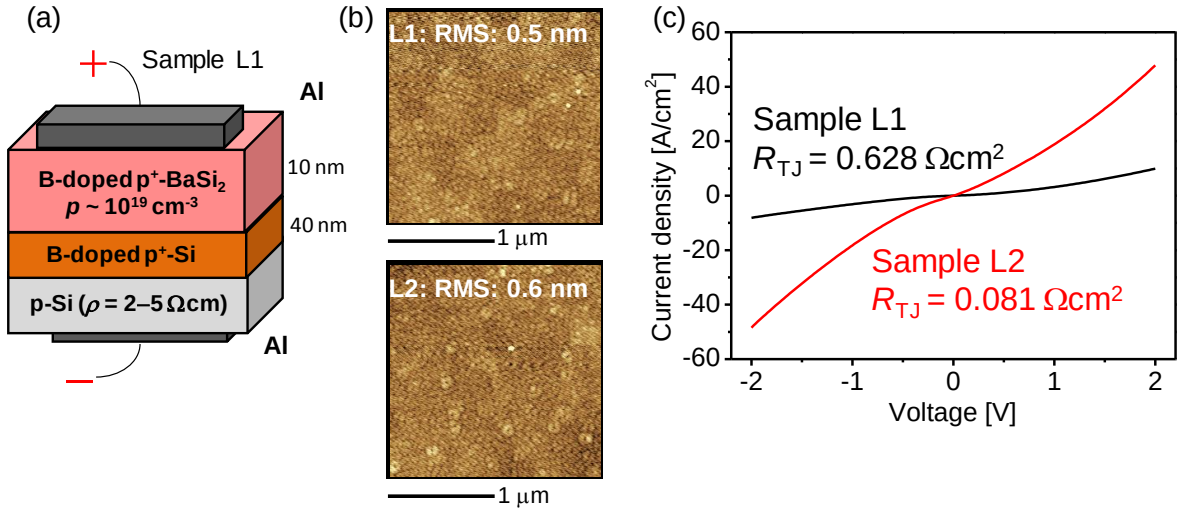

Fig 5.5 (a) Schematic diagram of *J–V* measurement for sample L1. (b) Surface morphology and (c) *J–V* characteristics of samples L1 and L2.

$BaSi_2$ films were formed on the TJ and first their crystalline quality was checked. Figures 5.6(a) and 5.6(c) show the RHEED patterns after each growth step for sample M1 and M2, respectively. With incident X-ray along Si[1-10], for sample M1, streaky patterns were observed after the growth of the top n+-$BaSi_2$ layer. However, for sample M2, RHEED patterns with spots appeared after the growth of p^+-Si and RDE process, indicating a rough surface was introduced, which was not good for subsequent growth of $BaSi_2$ epitaxial layers. And after grew a 500 nm-thick p-$BaSi_2$ absorber layer, RHEED pattern turned to be halo. From Figs. 5.6(b) and 5.6(d), both of these 2 samples have similar XRD results with *a*-axis-orientated $BaSi_2$ films, however, the intensity of *a*-axis-orientated peaks 200, 400, and 600 are much smaller for sample M2. The full width at half maxima (FWHM) values of $BaSi_2$ 600 diffraction peaks are different, those are 0.78° and 1.12° for samples M1 and M2, respectively. This means that the crystalline quality of the $BaSi_2$ films starts to deteriorate when they are grown on a low-ρ substrate. According to Yamashita *et al.*, step bunching occurred when thermal cleaning of the substrate at 900 °C was performed, to a far greater extent when a low-ρ substrate was used.[83]

Figures 5.7(a) and 5.7(b) show the surface morphologies, measured by AFM, of samples M1 and M2, respectively. Sample M1, which is formed on a medium resistive Si(001) substrate, shows smoother surface than sample M2, with a root-mean-square roughness value of 1.19 nm. Figure 5.7(c) shows the *J–V* characteristics of samples M1 and M2 under AM1.5G illumination. It is a pity that rectifying properties of these 2 samples have not been obtained, which is supposed to the diffusion of Sb atoms within $BaSi_2$ layers.[135] So we will try to inhibit the diffusion of Sb atoms in the future work.

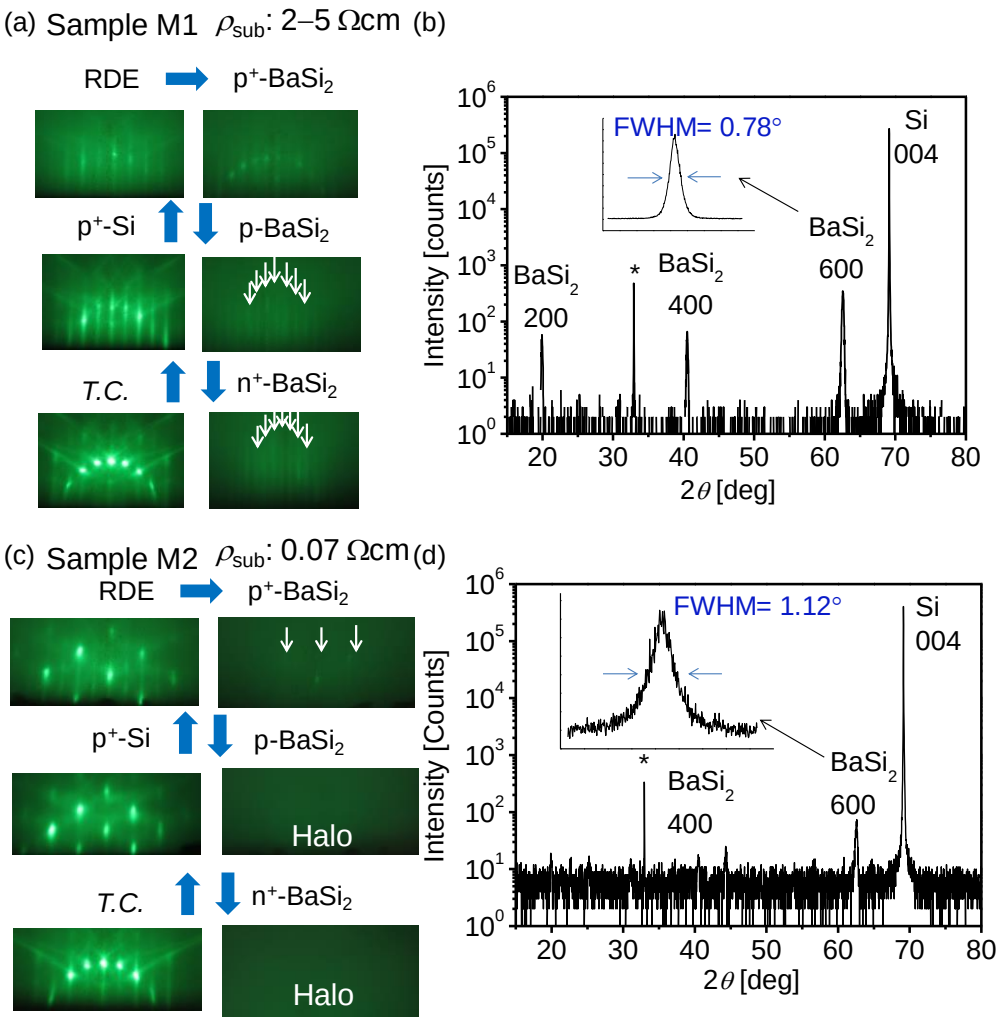

Fig 5.6 (a) and (c) RHEED patterns after each growth step of samples M1 and M2, respectively. (b) and (d) θ–2θ XRD results of sample M1 and M2, respectively. Inserted figures are the rocking-curve spectrum of $BaSi_2$ 600 peak. (*) represent the diffraction peak attributed from Si substrate.

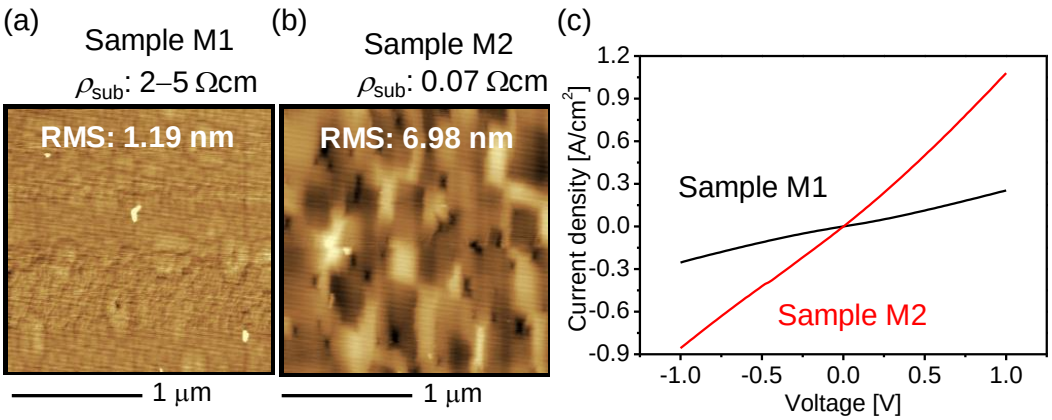

Fig. 5.7 Surface morphologies, measured by AFM, of (a) sample M1, and (b) sample M2. (c) J–V characteristics of samples M1 and M2 under AM1.5G illumination.

Even though we have not obtained the rectifying properties, we can still explore the potential of $BaSi_2$

for solar cell applications by measuring the photoresponsivity. Figures 5.8(a) and 5.8(b) show the photoresponsivity under various forward and reverse V_{bias} for samples M1 and M2. The direction of the current flow changed between the reverse and forward bias conditions. Light absorption produces electron-hole pairs that are separated by the electric field between the electrodes, which leads to current flow in the external circuit as the photoexcited carriers drift before recombination. Photocurrents were increased at around 1000 nm, corresponding to the absorption edge of $BaSi_2$. The photoresponsivity reached 0.35 A/W at 850 nm at V_{bias} = 1.0 V, corresponding to an *EQE* value of 54% for sample M1. Sample M2 shows worse photoresponsivity than sample M1, which is supposed due to the larger defect state originated from thermal cleaning.[83]

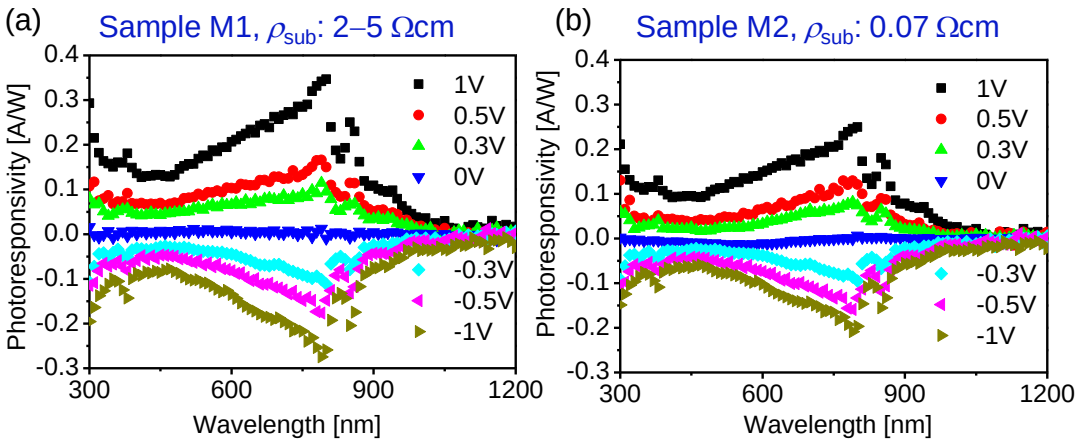

Fig. 5.8 Photoresponse properties of samples (a) M1 and (b) M2 under bias voltages.

5.4 Conclusion

In this chapter, an efficiency of 16.5% was obtained by simulating using AFORS-HET, with a 0.5 μm-thick $BaSi_2$ absorber layer on a p^+-$BaSi_2$/p^+-Si tunnel junction. The tunnel properties of the p^+-$BaSi_2$/p^+-Si junction were confirmed, and the tunnel current density reached 18.3 A/cm^2 at a V_{bias} = 1.0 V, indicating a sufficient tunnel resistance. Large photoresponsivity reaching 0.35 A/W at 850 nm at V_{bias} = 1.0 V, which corresponds to an *EQE* value of 54%, showing great promise of $BaSi_2$ on TJ for use in $BaSi_2$-homojunction and Si-based tandem solar cells.

Chapter 6 Simulation of $BaSi_2$-based homojunction and tandem solar cells

6.1 Background

The unique feature of $BaSi_2$ is that large α and L can be utilized simultaneously, indicating great potential of $BaSi_2$ as a light absorber layer for thin-film solar cell applications.[136] The η approached 10% without any special treatment for passivation in p-$BaSi_2$/n-Si heterojunction solar cells formed on both Si(111) and Si(001) substrates.[74,77,137] This value is the highest ever reported for solar cells fabricated with semiconducting silicide. Furthermore, several $BaSi_2$-based solar cells have been proposed; those are $BaSi_2$ nanowires, back-contacted $BaSi_2$, and perovskite/$BaSi_2$ dual-junction solar cells.[138-140] The carrier conductivity type and concentration of $BaSi_2$ can be effectively controlled by impurity doping, in particular, the electron and hole concentrations can reach ~10^{20} cm^{-3} through Sb and B doping, respectively.[54,60,72] Such high electron and hole density ensure that they can work as electron and hole transport layers in a homojunction solar cell, respectively. Recently, the operation of a $BaSi_2$ homojunction solar cell has been firstly demonstrated that the photo-generated carriers in the $BaSi_2$ layer can be separated by the build-in electric field in the homojunction diode.[76] However, the band offsets at the p^+-$BaSi_2$/p^+-Si interface hindered the transport of photo-generated carriers, resulting in a comparatively low η. This problem can be solved by optimizing the tunnel effect of the p^+-$BaSi_2$/p^+-Si diode in the near future. Another way to realize high-η is to form a tandem solar cell, where a wide E_g absorber layer for the top-cell is a necessity. $BaSi_2$ can be grown epitaxially on Si substrate;[63,64] its E_g can be increased to 2.0 eV by partly substituting Si with isoelectric C.[46] Therefore, $BaSi_2$ is a material of choice aiming for high-η tandem solar cells in a BaC_XSi_{2-X}/c-Si tandem-structure solar cell.

The most widely used free of charge softwares for solar cells are PC-1D, SCAPS-1D, wxAMPS, and AFORS-HET. PC1D is a computer program written for IBM-compatible personal computers that solves the fully coupled nonlinear equations for the quasi-one-dimensional transport of electrons and holes in crystalline semiconductor devices, with emphasis on photovoltaic devices.[141] It is designed for Si PVs and most widely used for its simple processes and calculation speed. SCAPS-1D is a one dimensional solar cell simulation program developed at the Department of Electronics and Information Systems (ELIS) of the University of Gent, Belgium. This original program is developed for cell structures of the CIS and the CdTe family, considering ion injection conditions which are not uniform distributed.[142] Kim *et al.* succeeded in simulating of CIGS/c-Si tandem solar cells using SCAPS-1D.[143] The wxAMPS program is a 1D solar cell simulation program designed at the University of Illinois at Urbana Champaign, in collaboration with Nankai University of China. It follows the physical principle of AMPS, adds the portion of tunneling currents, improves convergence and speed, and provides an improved visualization.[144] It is originally designed for Si PVs with considering the effect of tails states, defects and etc. AFORS-HET is a numerical simulation tool, which allows to model homo- as well as heterojunction devices.[126] And it is reported to be able for the simulation of perovskite/c-Si tandem solar cells.[145] The above mentioned 4 softwares are useful, however, they all address individual solar cell viewpoints, without providing a complete coverage of the complex combination of phenomena that actually take place. And we found that simulating $BaSi_2$-based tandem solar cell is not appropriate using these softwares. So in this chapter, a commercial software, that is Silvaco-Atlas, has been used.

6.2 Introduction to Silvaco-Atlas

Silvaco-Atlas software is a device simulator that performs DC, AC, and transient analysis for silicon, binary, ternary, and quaternary material-based devices. It enables the characterization and optimization of semiconductor devices for a wide range of technologies. Device simulation helps us understand and depict the physical processes and make reliable predictions of the device behavior. 2D device simulations with properly selected calibrated models and a very well-defined appropriate mesh structure are very useful for predictive parametric analysis of novel device structures. 2D modeling and simulation processes help us to obtain a better understanding of the properties and behavior of new and current devices. This helps provide improved reliability and scalability, while also helping to increase development speed and reduce risks and uncertainties.[146] Unlike the four solar cell simulation models mentioned above, which are based on a combination of discrete electrical components, this novel model extracts the electrical characteristics of a solar cell based on virtual fabrication of its physical structure, allowing for direct manipulation of materials, dimensions, and dopings. Atlas provides a comprehensive set of physical models as shown in Fig. 6.1. Based on these physical models, it is best used with the technology-based computer aided design tool (TCAD) tools. These include DeckBuild, TonyPlot, DevEdit, MaskViews, and Optimizer. DeckBuild provides an interactive run time environment. TonyPlot supplies scientific visualization capabilities. DevEdit is an interactive tool for structure and mesh specification and refinement. MaskViews is an IC Layout Editor. The Optimizer supports black box optimization across multiple simulators. Silvaco-Atlas receives input files through DeckBuild. The code entered in the input file calls Atlas to run with the following command: **go atlas**. Following that command, the input file needs to follow a pattern. The command groups are listed in Fig. 6.2. Atlas follows the following format for statements and parameters:

<STATEMENT> <PARAMETER>=<VALUE>

The following line of code serves as an example:

DOPING REGION=1 UNIFORM N.TYPE CONC=2e19

The statement is DOPING. The parameters are REGION, UNIFORM, N.TYPE, and CONCENTRATION. The input codes for simulating $BaSi_2$-based solar cells are displayed in Appendix A.

- DC, AC small-signal, and full time-dependency.
- Drift-diffusion transport models.
- Energy balance and Hydrodynamic transport models.
- Lattice heating and heatsinks.
- Graded and abrupt heterojunctions.
- Optoelectronic interactions with general ray tracing.
- Amorphous and polycrystalline materials.
- General circuit environments.
- Stimulated emission and radiation
- Fermi-Dirac and Boltzmann statistics.
- Advanced mobility models.
- Heavy doping effects.
- Full acceptor and donor trap dynamics
- Ohmic, Schottky, and insulating contacts.
- SRH, radiative, Auger, and surface recombination.
- Impact ionization (local and non-local).
- Floating gates.
- Band-to-band and Fowler-Nordheim tunneling.
- Hot carrier injection.
- Quantum transport models
- Thermionic emission currents.

Fig. 6.1 Silvaco-Atlas physical models

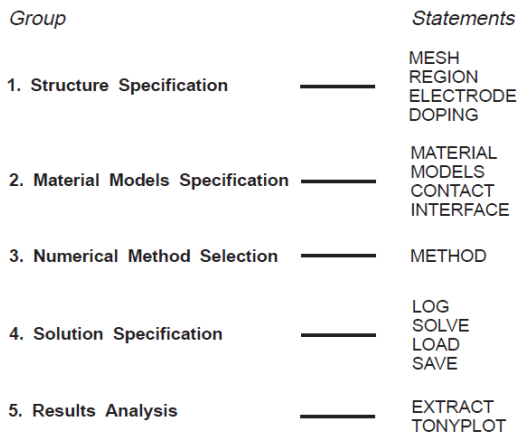

Fig. 6.2 Atlas command groups and primary statements

In 2008, Baudrit *et al.* succeeded in simulating a Dual-Junction (DJ) GaInP/GaAs solar cell for the first time, including a complete TJ model and the resonant cavity effect occurring in the bottom cell. They demonstrated that solar cells simulation using Silvaco-Atlas software is possible and can be predictive for single junction solar cells as well as for DJ solar cells with assuming a non-local band to band transition.[147] One year later, Tsutagawa *et al.* reported a triple junction InGaP/GaAS/Ge solar cell with a 36.2% efficiency using Silvaco-Atlas modeling and simulation. And a new method was introduced, that was defining a lumped resistance between the top and bottom cells, so that current can flow through without significant limitation.[148] In 2015, Elbar *et al.* presented numerical simulations to analyze the performance of a DJ CGS/CIGS tandem solar cell. They considered the thickness of the top-cell as a key parameter to further improve the performance of the CGS/CIGS tandem cell. With fixed thickness of the bottom-cell at 3.5 μm, maximization of the CGS/CIGS tandem cell efficiency of 26.21% was achieved at an optimal thickness of the top-cell of 0.19 μm. Thickness dependent top-cell light absorption was essentially behind such CGS/CIGS tandem cell photovoltaic behavior.[149] So Silvaco-Atlas is a powerful software for simulating $BaSi_2$ homojunction and tandem solar cells. In this chapter, we first go for the structure design for $BaSi_2$ homojunction solar cells, and then move to the optimization of $BaSi_2$/Si DJ solar cells by adjusting the *d* of top-cell $BaSi_2$ absorber layer.

6.3 Simulation method

Silvaco Atlas presents solar cell performance according to Poisson's equation, electrons and holes continuity equations through a 2-D grid by considering a wide variety of semiconductor physics models for drift-diffusion transport, Shockley-Read-Hall (SRH) recombination, Auger recombination, carrier concentration dependent mobility (CONMOB), carrier generation, Fermi-Dirac statistics, tunneling effect, etc.[146,149,150] The accuracy of the material parameters defined in the solar cell model such as E_g, n, p, carrier mobility (μ_n and μ_p), permittivity, affinity, carrier lifetime (τ_n and τ_p), and effective density of states in the conduction and valence bands (N_C and N_V), determines the accuracy of the simulated results. In this study, SRH recombination, which is the main recombination mechanism in $BaSi_2$,[51] as well as the Fermi-Dirac statistics were taken into consideration. The values of carrier mobility and carrier lifetime were specified for each $BaSi_2$ layer according to the experimental values.[151,152] Regarding the carrier mobility of silicon, default values which were embedded in the CONMOB model in the software, were used. The input parameters for simulation are given in Table 6.1.[42,44,73,151] One of the most important parameters for advanced solar cell modeling is the optical properties containing refractive index *n'* and extinction coefficient *k* against

wavelength, which decide the transmission and attenuation of light passing through the semiconductor. The *n'* and *k* values of $BaSi_2$ were extracted from the experimental results as shown in Fig. 6.3(a),[44,140] where *k* is calculated from the relationship $\alpha = 4\pi k/\lambda$. There is, however, no experimental data on the α of BaC_xSi_{2-x} absorber layers ($E_{g,top}$ = 1.4, 1.5, 1.6, and 1.7 eV). In this paper, we therefore assume them from those of $BaSi_2$ by shifting the energy by an increment of E_g. The obtained α values are shown in Fig. 6.3(b).

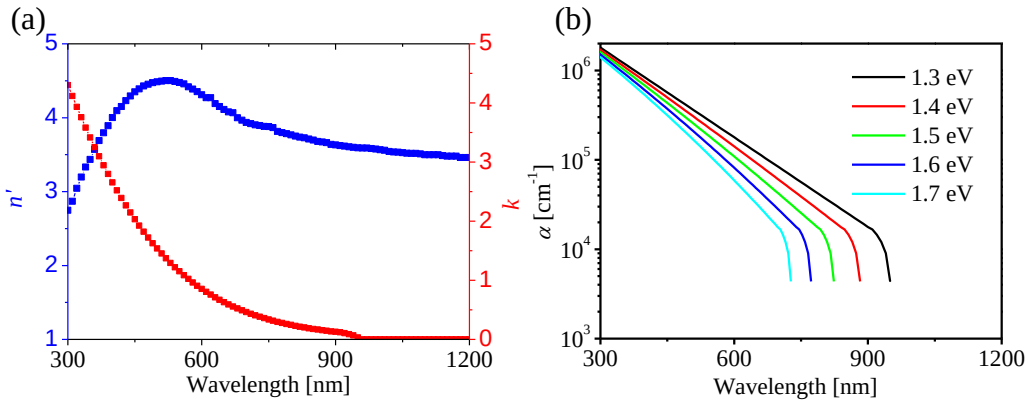

Fig. 6.3 (a) The *n'* and *k* values of $BaSi_2$ against wavelength. (b) α of BaC_xSi_{2-x} ($E_{g,top}$ = 1.4, 1.5, 1.6, and 1.7 eV) against wavelength.

Table 6.1 Input parameters for simulation.

Material	n^+-$BaSi_2$	p-$BaSi_2$	p^+-$BaSi_2$	p^+-$BaSi_2$ Tunnel	n^+-Si Tunnel	n^+-Si	p-Si	p^+-Si
d [nm]	20	variable	20	15	15	100	2e5	1e3
E_g [eV]	1.3	1.3	1.3	1.3	1.1	1.1	1.1	1.1
n [cm^{-3}]	1e20	–	–	–	1e20	1e19	–	–
p [cm^{-3}]	–	1e17	1e20	2e20	–	–	7e16	1e19
Permittivity	14.0	14.0	14.0	14.0	11.7	11.7	11.7	11.7
Affinity [eV]	3.2	3.2	3.2	3.2	4.05	4.05	4.05	4.05
N_C [cm^{-3}]	2.6e19	2.6e19	2.6e19	2.6e19	2.8e19	2.8e19	2.8e19	2.8e19
N_V [cm^{-3}]	2.0e19	2.0e19	2.0e19	2.0e19	1.0e19	1.0e19	1.0e19	1.0e19
τ_n [μs]	3	8	2	Lumped resistance		Default values		
τ_p [μs]	3	8	2					
μ_n [cm^2/Vs]	500	850	600					
μ_p [cm^2/Vs]	20	100	30					

Due to the structure of practical $BaSi_2$ homojunction solar cell,[76] a solar cell in the p-i-n architecture was proposed. Figure 6.4 displays the schematic diagram of a $BaSi_2$/c-Si tandem solar cell, consisting of an n^+pp^+-$BaSi_2$ homojunction top-cell and a c-Si bottom-cell. The *d* of heavily doped n^+- and p^+-$BaSi_2$ layers were set to be 20 nm, which is the minimum *d* required to sufficiently cover the whole surface by experiment.[78] The *d* of lightly doped p-$BaSi_2$ absorber layer ($p = 5\times10^{17}$ cm^{-3}) was set a value between 0.2 and 10 μm to examine its effect on solar cell performance. Meanwhile, the c-Si bottom-cell was simulated with insignificant difference from those obtained from Ref. [153]. When stacking the top $BaSi_2$ solar cell with a bottom c-Si solar cell, a lumped resistance was defined for the tunnel junction so that the current can flow within the tandem

solar cell without significant limitation.[149] We also assumed no optical loss or electrical loss at every interface throughout the device. The simulation was performed under 1 sun of standard AM1.5G spectrum. A wide variety of outputs such as *J–V* characteristics, *EQE* spectrum, photogeneration rate, and potential across the device, were available using Silvaco Atlas simulation package. By changing the *d* of the top p-$BaSi_2$ absorber layer, the current matching point between the two cells was examined.

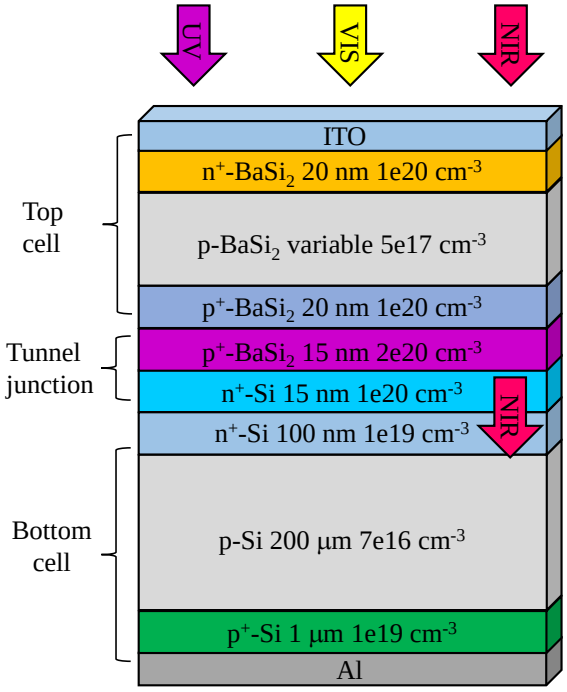

Fig. 6.4 Schematic diagram of a $BaSi_2$/c-Si tandem solar cell consisting of an n^+pp^+-$BaSi_2$ top-cell and a c-Si bottom-cell.

6.4 Results and discussion

6.4.1 Top-cell simulation

In order to form the homojunction solar cell, we placed high-*n* and -*p* $BaSi_2$ layers at opposite sides of low-*p* $BaSi_2$ absorber layer as electron and hole transport layers, respectively, so that photogenerated electron-hole pairs can be extracted.[76] The structure is shown in Fig. 6.5. After assuming the structure, parameters of each layer are also be specified in Table 6.1.

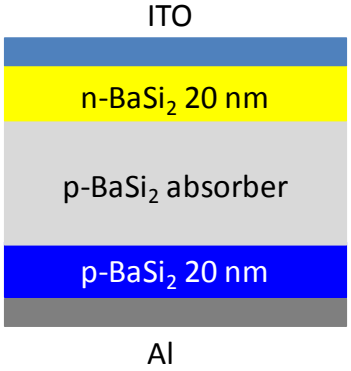

Fig. 6.5 Structure of the $BaSi_2$ homojunction solar cell.

Figures 6.6(a) and 6.6(b) show the simulated results of short-circuit current density J_{SC}, η, V_{OC}, and fill factor *FF* against the *d* of p-$BaSi_2$ absorber layer. All these values initially increased with *d*, and then almost saturated at $d \geq 2$ μm. This is due to the large α of $BaSi_2$ that only a 2 μm-thick film can effectively absorb visible light according to Beer-Lambert law.[154] Figures 6.6(c) and 6.6(d) show the *J*–*V* curves and *EQE* spectrum of a 2 μm-thick $BaSi_2$ solar cell with an η of 23.3%, J_{SC} of 30.3 mA/cm^2, V_{OC} of 0.88 V, and *FF* of 86.9%. The attenuation of *EQE* in the short wavelength range was attributed to the large *n'* thus reflectance, which can be greatly reduced by adopting a pyramid-like textured structure.[155] The comparison of simulated $BaSi_2$ homojunction solar cell with state-of-the-art single junction solar cells is shown in Table 6.2. The simulated $BaSi_2$ homojunction solar cell provided higher η compared with CIGS and CdTe solar cells due to the high J_{SC} and *FF*. The V_{OC} loss was 32%, which was smaller than CIGS (34%) and CdTe (38%) solar cells, but larger than perovskite (22%) solar cells. Such a loss was caused by the recombination of minority carriers in $BaSi_2$. Supplying atomic H during the growth of $BaSi_2$ films to increase a minority-carrier lifetime can help to overcome this problem.[156] So further study can be conducted to reduce the reflectance and increase the minority-carrier lifetime towards higher η. Thus, it is safe to state that $BaSi_2$ is promising for thin-film solar cell applications.

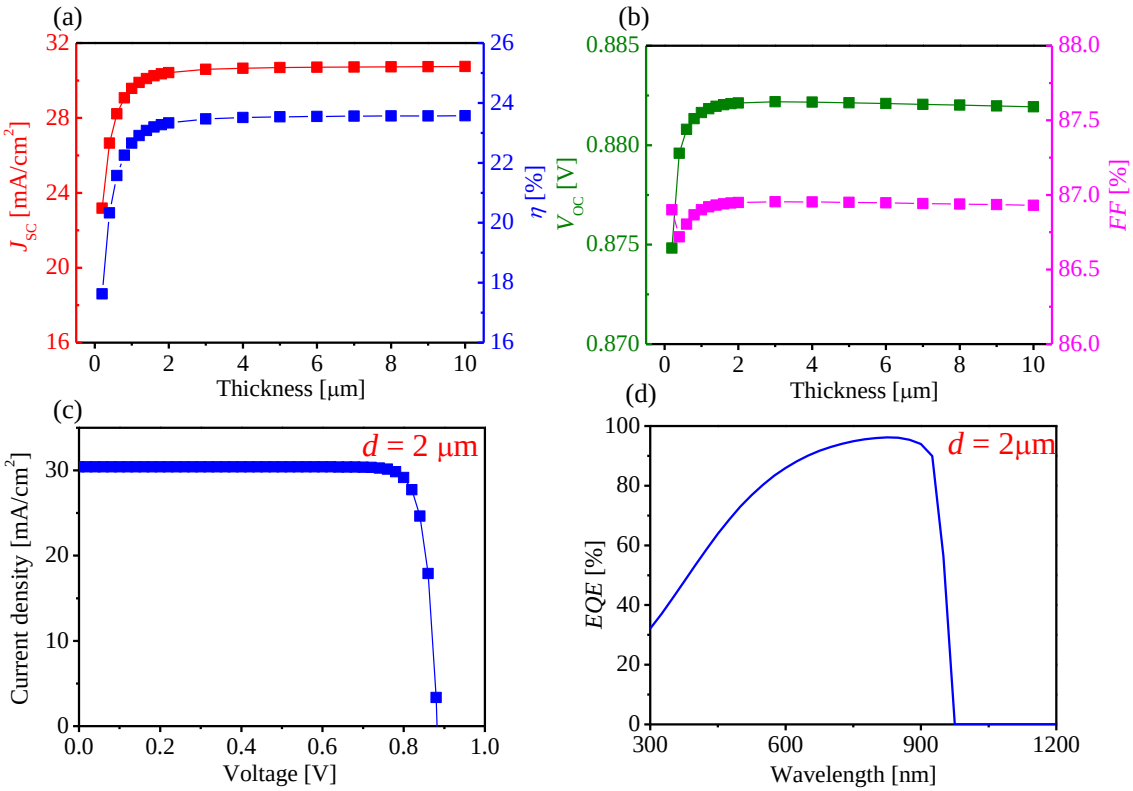

Fig. 6.6 (a) J_{SC} and η; (b) V_{OC} and *FF* of $BaSi_2$ solar cells against the *d* of p-$BaSi_2$ light absorber layer. (c) *J*–*V* curves and (d) *EQE* spectrum of a $BaSi_2$ homojunction solar cell with a 2 μm-thick absorber layer.

The J_{SC}, η, and V_{OC} against *d* of BaC_xSi_{2-x} solar cells ($E_{g,top}$ = 1.4, 1.5, 1.6, and 1.7 eV) are shown in Figs. 6.7(a)–6.7(c). The J_{SC} and η increase with *d* of absorber layer, indicating that incomplete light absorption occurs when *d* of BaC_xSi_{2-x} is less than 2 μm. The V_{OC} remains almost unchanged as the *d* of absorber layer increases. This is due to the assumption that the *d* of BaC_xSi_{2-x} absorber does not affect any of recombination mechanisms or interfaces. As a consequence, the BaC_xSi_{2-x} solar cells with thinner *d* retain the device behavior compared to the cells with $d \geq 2$ μm. Due to the fact that $BaSi_2$ as well as BaC_xSi_{2-x} have quite large α, the thinning of top-cell is essential to ensure the current matching condition when stacked with the bottom c-Si

solar cell. Figure 6.7(d) shows the *EQE* spectra of 2 μm-thick BaC_xSi_{2-x} solar cells for various values of $E_{g,top}$ in the range 1.4–1.7 eV. There is no significant change of *EQE* in the short wavelength range. Only the cutoff wavelength of the *EQE* spectra shifted to a short wavelength range in accordance with the increase of $E_{g,top}$.

Table 6.2 Comparison of simulated $BaSi_2$ solar cell with state-of-the-art single junction solar cells.

Material	η [%]	J_{SC} [mA/cm^2]	V_{OC} [V]	*FF* [%]	E_g [eV]	*d* [μm]	Reference
Si(HJ-IBC)	26.7	42.6	0.783	84.9	1.12	165	[9]
GaAs	27.6	29.6	1.107	84.1	1.43	~2	[157]
CIGS	22.9	38.5	0.746	79.7	1.13	2~3	[22]
CdTe	22.1	30.2	0.876	79.4	1.43	3~5	[14]
Perovskite	22.7	24.9	1.144	79.6	1.47	~0.5	[158]
$BaSi_2$ (simulation)	23.3	30.3	0.88	86.9	1.30	2	This work

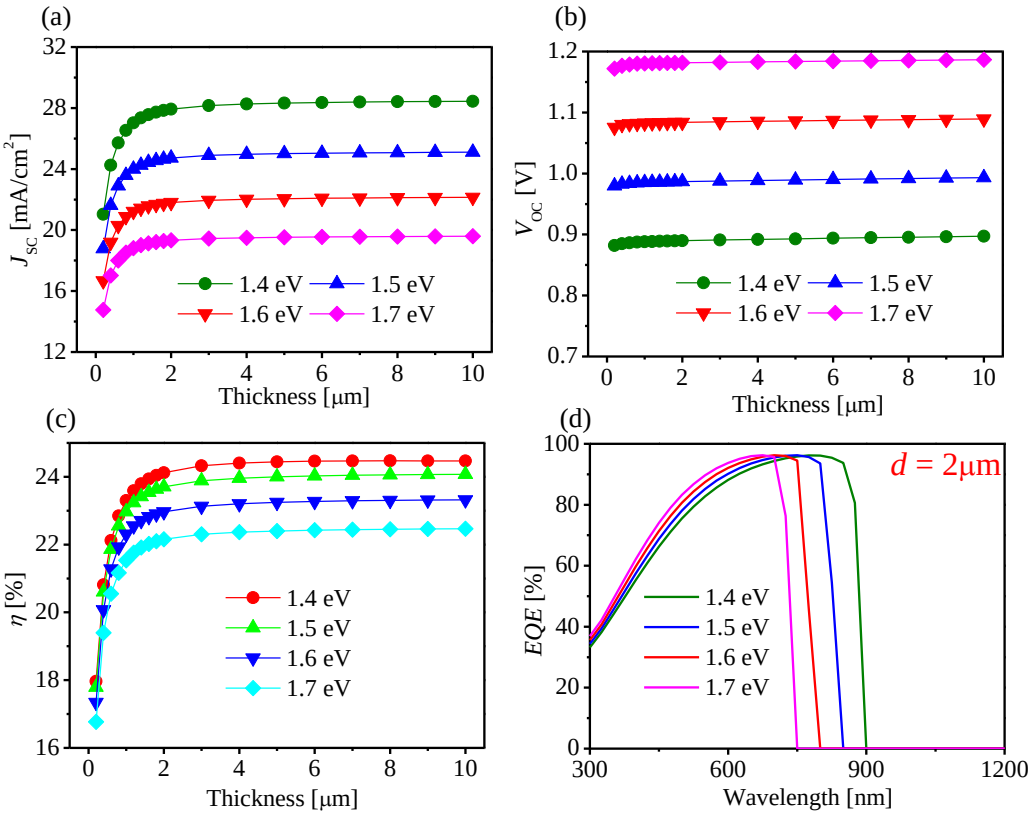

Fig. 6.7 (a) J_{SC}; (b) V_{OC}; (c) η of BaC_xSi_{2-x} ($E_{g,top}$ = 1.4, 1.5, 1.6, and 1.7 eV) solar cells against the *d* of absorber layer. (d) *EQE* spectra of the BaC_xSi_{2-x} solar cells with a 2 μm-thick absorber layer.

6.4.2 Bottom-cell simulation

The bottom c-Si solar cell with a typical performance was used in the tandem solar cell. The structure is shown in Fig. 6.8(a). This simulation is modeled after the example of a high-η c-Si solar cell, which shows an η of 19.3% with J_{SC} = 34.0 mA/cm^2, V_{OC} = 0.67 V, and FF = 84.0%.[153] Basically, the parameters, carrier mobility and carrier lifetime, used to simulate a c-Si solar cell are based on default values embedded in the Silvaco Atlas. CONMOB statement enables the concentration dependent mobility model in the simulation. It is a table consisting of doping versus mobility for Si. Fig. 6.8(b) presents the simulated J–V curve of the c-Si solar cell, which exhibits an η of 18.9% with J_{SC} = 34.0 mA/cm^2, V_{OC} = 0.66 V, and FF = 83.7%, indicating insignificant simulation difference between ours and Ref. [153].

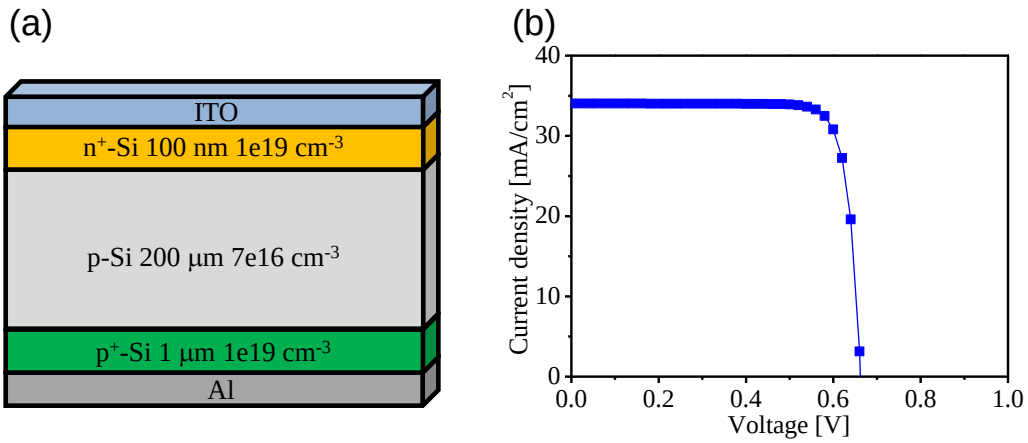

Fig. 6.8 (a) The structure and (b) simulated J–V curve of the c-Si solar cell.

6.4.3 Tandem-cell simulation

The current of a tandem solar cell is determined by a lower current flowing through either a top-cell or a bottom-cell. One important thing when stacking two solar cells is to assume the current matching condition, so that the current loss can be controlled as small as possible. A wide $E_{g,top}$ absorber layer is necessary in the top-cell so that near-infrared and part of visible light can pass through the top-cell and be absorbed by the bottom-cell. Here we adopted BaC_xSi_{2-x} solar cells with $E_{g,top}$ = 1.6 and 1.7 eV as a top cell. In the present work, the d of the top absorber layer was varied from 50 nm to 1 μm, while the bottom c-Si remained the same. Fig. 6.9(a) and 6.9(b) show the J_{SC} values of the top and bottom-cells versus d of BaC_xSi_{2-x} absorb layer ($E_{g,top}$ = 1.6 and 1.7 eV) in the top-cell, where significant d dependences are shown for both values of $E_{g,top}$. As d increases, the J_{SC} of a top-cell increases and J_{SC} of a bottom-cell decreases accordingly. This is simply owing to the fact that the thicker the top-cell became the more photos were absorbed in the top-cell, leaving less light transmitted to the bottom-cell. The current matching point J_{SC} = 17.4 mA/cm^2 was fulfilled at d = 215 nm for BaC_xSi_{2-x} absorb layer with $E_{g,top}$ = 1.6 eV. In the same way, the current matching condition was confirmed at d = 500 nm with J_{SC} = 17.6 mA/cm^2 for BaC_xSi_{2-x} with $E_{g,top}$ = 1.7 eV. As shown in Figs. 6.9(c) and 6.9(d), the η of the tandem solar cells reach a maximum at the current matching point. Under such current matching conditions, the performance of BaC_xSi_{2-x}/c-Si tandem solar cells was simulated. The J–V curves of tandem-, top- and bottom-cells are plotted in Figs. 6.9(e) and 6.9(f) for the top-cell with $E_{g,top}$ = 1.6 and 1.7 eV, respectively. The J_{SC} of the tandem-, top- and bottom-cells are equal to the maximum of 17.6 mA/cm^2 with an V_{OC} = 1.94 eV and η = 30.3% for the tandem cell with a E_g = 1.7 eV top-cell. The values of V_{OC} = 1.94 eV and η = 30.3% are equal to the sum of those of the top-cell (V_{OC} = 1.27 eV and η = 20.4%) and bottom-cell (V_{OC} = 0.67 eV and η = 9.9%), indicating almost no energy loss. The EQE of both top- and bottom-cells under the current matching point are shown in Figs. 6.9(g) and 6.9(h). The EQE of the bottom c-Si cell exceeds 80% at a

wavelength around 900 nm.

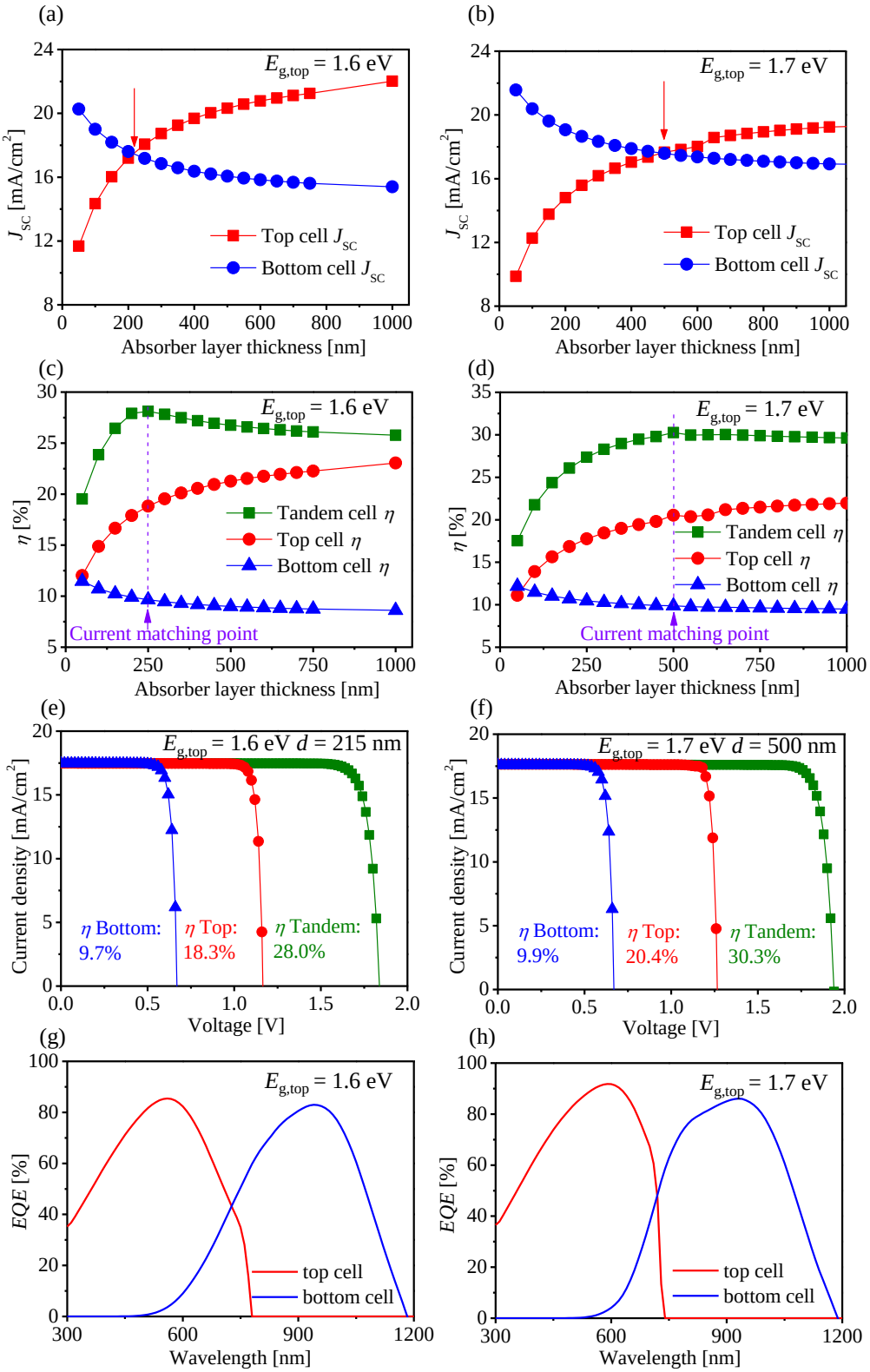

Fig. 6.9 J_{SC} of top- and bottom-cells against d of top-cell absorber layer (a) $E_{g,top}$ = 1.6 eV; (b) $E_{g,top}$ = 1.7 eV. η of tandem-, top-, and bottom-cells against d of top-cell absorber layer (c) $E_{g,top}$ = 1.6 eV; (d) $E_{g,top}$ = 1.7 eV. J–V curves of tandem-, top-, and bottom-cells at current matching point (e) $E_{g,top}$ = 1.6 eV; (f) $E_{g,top}$ = 1.7 eV. EQE spectra of top- and bottom-cell (g) $E_{g,top}$ = 1.6 eV; (h) $E_{g,top}$ = 1.7 eV.

Figure 6.10(a) shows the structure of the highest-η (30.3%) tandem solar cell generated by Silvaco Atlas. As the bottom c-Si solar cell has a much larger d than the top-cell, the expanded view of red dash area in Fig. 6.10(a) is shown in Fig. 6.10(b). Figure 6.10(c) displays the potential distribution developed throughout the tandem solar cell. Due to the presence of built-in potential at the tunnel junction, it shows a higher potential in this region and the potential goes on lowering as we move in both directions from the tunnel junction. The photogeneration rate in each layer is shown in Fig. 6.10(d). The photogeneration rate indicates the number of photons generated across the layers of the cell under sunlight, and the graph shows that the top BaC_xSi_{2-x} solar cell has a higher rate of photogeneration than that of the bottom-Si solar cell. In the tunnel junction region, recombination of photogenerated carriers occurs. Due to this recombination, a low photogeneration rate is observed.

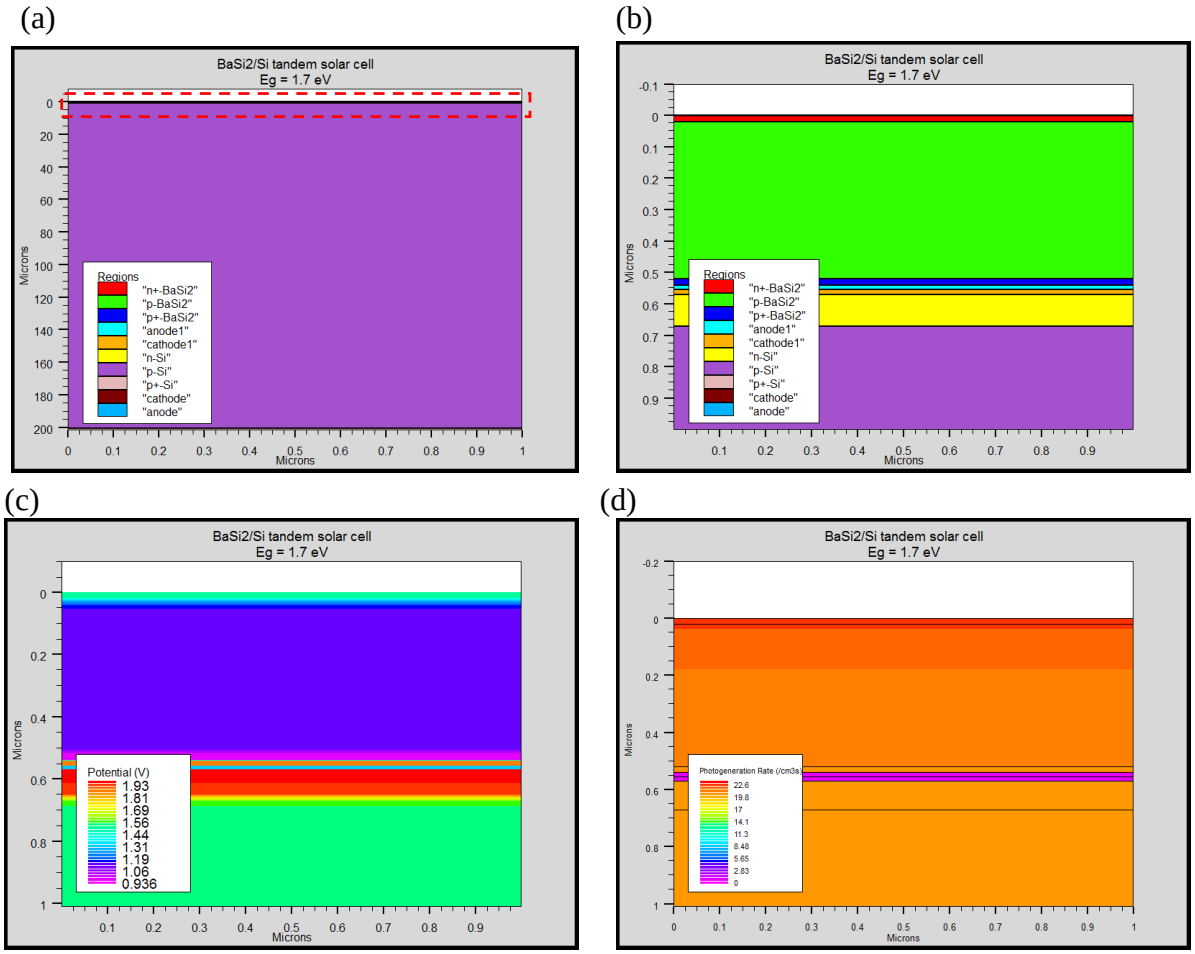

Fig. 6.10 (a) Structure of the tandem solar cell generated by Silvaco Atlas. (b) Expanded view of red dash area in (a). (c) Potential distribution and (d) photogeneration rate developed in the tandem solar cell with expanded top view.

Table 6.3 summaries a comparison of simulated BaC_xSi_{2-x}/c-Si tandem solar cell with other practical state-of-the-art dual-junction solar cells. Our simulated tandem solar cell shows great properties with a large η and V_{OC}. As $BaSi_2$ can be grown epitaxially on a Si substrate with very good crystal quality,[53,83] and a good tunnel effect associated with a small tunnel resistance can be achieved based on a $BaSi_2$/c-Si tunnel junction,[80,82] a high-η tandem solar cell can be expected with a thin top BaC_xSi_{2-x} solar cell.

Table 6.3 Comparison of simulated BaC_xSi_{2-x}/c-Si solar cell with state-of-the-art dual junction solar cells.

Material	η [%]	J_{SC} [mA/cm^2]	V_{OC} [V]	FF [%]	Reference
a-Si:H/nc-Si:H	12.7	13.5	1.342	70.2	[159]
$Al_{0.15}Ga_{0.85}As$/c-Si	21.2	23.6	1.57	77.2	[160]
Perovskite/CIGS	22.4	17.3	1.77	73.1	[161]
Perovskite/c-Si	23.6	18.1	1.65	79.0	[162]
BaC_xSi_{2-x}/c-Si (simulation)	30.3	17.6	1.94	88.4	This work

6.5 Conclusion

In this chapter, design and simulation of $BaSi_2$ homojunction and BaC_xSi_{2-x}/c-si tandem solar cells were performed using Silvaco Atlas simulation package. With input the optical and electrical parameters, an efficiency of 23.3% under AM1.5G 1 sun illumination for an n^+pp^+-$BaSi_2$ homojunction solar cell was obtained with only a 2 μm-thick absorber layer. This result is comparable to other state-of-the-art single junction solar cells. When stacking a 1.7-eV-E_g BaC_xSi_{2-x} top-cell with a c-Si bottom-cell for a tandem solar cell, the current matching point was found with J_{SC} = 17.6 mA/cm^2 at d = 500 nm for top absorber layer. At this point, the η reached a maximum value of 30.3% with an V_{OC} = 1.94 V. On the basis of these promising results, we can state that $BaSi_2$ may be a very good candidate to be used in thin-film and tandem solar cell applications in recent future.

Chapter 7 Summaries

The works in this thesis can be summarized as follows:

Electron and hole mobilities versus temperature in $BaSi_2$ have been systematically studied both experimentally and theoretically. The experiments were performed with undoped 250 nm-thick $BaSi_2$ polycrystalline films grown by molecular beam epitaxy. The grain size of films ranged from 0.2 to 5 μm with the n of 5.0×10^{15} cm^{-3}. To investigate the hole mobility, B-doped p-$BaSi_2$ films with various dopant concentrations were fabricated and studied. The experimental temperature dependence of the electron mobility in the range of 160 – 300 K was found to have a maximum of 1230 $cm^2/V{\cdot}s$ at 218 K, while at RT it dropped down to 816 $cm^2/V{\cdot}s$. We demonstrate that the temperature dependence of the electron mobility cannot be adequately reproduced by involving standard scattering mechanisms. A modified approach accounting for the grained nature of the films has been proposed for the correct description of the mobility behavior. The highest hole mobility in p-$BaSi_2$ films reaching ~ 80 or 200 $cm^2/V{\cdot}s$ (for the films grown on (111) or (001) Si substrates, respectively) at RT is about an order or four times of magnitude smaller than that in n-$BaSi_2$ films. Such a great difference we ascribe to the specific features of electron-phonon and hole-phonon coupling in $BaSi_2$. For device applications, where higher hole mobility values are desirable, we can suggest using $BaSi_2$ grown on Si(100) substrates rather than Si(111) ones.

After explaining the transport properties of $BaSi_2$ films, we started to form p-$BaSi_2$/n-Si solar cells on Si(001) substrates. First, we used a textured Si(001) substrates which consisted of {111} facets. The light-trapping effect of these films and their performance when incorporated into solar cells were measured. X-ray diffraction and reflectivity measurements showed that the $BaSi_2$ films were grown epitaxially on the textured Si(001) substrate and confirmed the light-trapping effect. p-$BaSi_2$/n-Si solar cells were fabricated with varying $BaSi_2$ layer thickness and with hole concentrations in the range between 2.0×10^{18} and 4.6×10^{18} cm^{-3}. These cells exhibited a maximum energy conversion efficiency of 4.6% with an V_{OC} of 0.30 V and a short-circuit current density of 27.6 mA/cm^2 when the p-$BaSi_2$ layer was 75 nm-thick. The film grown around the ridge lines of each Si pyramid and the Si steps on the {111} facets resulted in the lower J_{SC} and V_{OC} parameters.

Owing to the existence of defects at the interface of p-$BaSi_2$ and textured Si(001), we then moved to form p-$BaSi_2$/n-Si solar cells on a flat n-Si(001) substrates. The influence of the $BaSi_2$ thickness and hole concentration on the solar cells properties were examined. The η reached a maximum value of 9.8% with a J_{SC} of 37.0 mA/cm^2, a V_{OC} of 0.44V, and a FF of 59.7% with a thickness of 40 nm and a hole concentration of 1.1×10^{18} cm^{-3} for p-$BaSi_2$. These values were comparable to those obtained for devices fabricated on Si(111), indicating that Si(001) substrates can also be used for $BaSi_2$ solar cells.

Our goal is the fabrication of high-η $BaSi_2$/c-Si tandem solar cells. Prior to the formation of a $BaSi_2$/c-Si tandem solar cell, we aimed to form a p^+-$BaSi_2$/p^+-Si TJ, which is necessary to make the electrical contact between $BaSi_2$ and c-Si solar cells sufficiently small. The tunnel properties of the p^+-$BaSi_2$/p^+-Si junction were confirmed, and the tunnel current density reached 18.3 A/cm^2 at a V_{bias} = 1.0 V, indicating a sufficient tunnel resistance. Large photoresponsivity reaching 0.35 A/W at 850 nm at V_{bias}=1V, which corresponds to an EQE value of 54%, showing great promise of $BaSi_2$ on TJ for use in $BaSi_2$-homojunction and Si-based tandem solar cells.

Simulation on $BaSi_2$ homojunction and BaC_xSi_{2-x}/c-Si tandem solar cells have been done to check their performance so as to help us understand and depict the physical processes and make reliable predictions of the device behavior. By using experimentally obtained optical and electrical parameters, an η of 23.3% under AM1.5G 1 sun illumination for an n^+pp^+-$BaSi_2$ homojunction solar cell was obtained with only a 2 μm-thick absorber layer. This result is comparable to other state-of-the-art single junction solar cells. When stacking a 1.7-eV-E_g BaC_xSi_{2-x} top-cell with a c-Si bottom-cell for a tandem solar cell, the current matching point was found with J_{SC} = 17.6 mA/cm^2 at d = 500 nm for top absorber layer. At this point, the η reached a maximum value of 30.3% with an V_{OC} = 1.94 V. On the basis of these promising results, we can state that $BaSi_2$ may be a very good candidate to be used in thin-film and tandem solar cell applications in recent future.

Appendix A. Input codes for simulating $BaSi_2$-based solar cells

1. Example Silvaco Atlas code for finding η for a $BaSi_2$ homojunction solar cell

```
go atlas

#top n+-BaSi2
set top1thick=0.02
set top1con=1e20

#top p-BaSi2
set top2thick=0.2
set top2con=5e17

#top p+-BaSi2
set top3thick=0.02
set top3con=1e20

set topcellthick=$top1thick+$top2thick+$top3thick

#mesh auto
mesh auto
x.mesh loc=0.0 spac=0.1
x.mesh loc=1.0 spac=0.1

#mesh.y
y.mesh loc=0.0 spac=0.1
y.mesh loc=$top1thick spac=0.1*$top1thick
y.mesh loc=$top1thick+$top2thick spac=0.1*$top2thick
y.mesh loc=$topcellthick spac=0.1*$top3thick

#regions
region number=1 name="n+-BaSi2" user.material=BaSi2 y.min=0 y.max=$top1thick
region number=2 name="p-BaSi2" user.material=BaSi2 y.min=$top1thick y.max=$top1thick+$top2thick
region number=3 name="p+-BaSi2" user.material=BaSi2 y.min=$top1thick+$top2thick y.max=$topcellthick

#electrode
electrode num=1 name=cathode top material=ito
electrode num=2 name=anode bottom material=Aluminum

#doping
doping region=1 uniform n.type conc=$top1con
doping region=2 uniform p.type conc=$top2con
doping region=3 uniform p.type conc=$top3con
```

```
#material
material material=BaSi2 user.group=semiconductor user.default=silicon index.file=BaSi13.nk
material material=BaSi2 EG300=1.3 PERMITTIVITY=14 AFFINITY=3.2 NC300=2.6e19 NV300=2.0e19
material material=Aluminum sopra=Al.nk
material region=1 MUN=500 MUP=20 taun0=3e-6 taup0=3e-6
material region=2 MUN=850 MUP=100 taun0=8e-6 taup0=8e-6
material region=3 MUN=600 MUP=30 taun0=2e-6 taup0=2e-6

save outfile=basi2homo1_1.str

#model
model srh fermi conmob temp=300 print

#method
method newton maxtraps=10 dvmax=0.1
output con.band val.band

beam number=1 x.orig=0.5 y.orig=-0.02 angle=90 power.file=am15.spec back.refl wavel.start=0.28 wavel.end=4
wavel.num=2002
solve init
solve previous
solve b1=1e-2
solve b1=1e-1
solve b1=1e0

log outfile=basi2homo1_1.log
solve vanode=0.0 name=anode vstep=0.02 vfinal=1.0
log off

extract init infile="basi2homo1_1.log"
extract name="Isc" y.val from curve(v."anode", i."cathode") where x.val=0.0
extract name="JscmAcm2" $Isc*1e08*1e03
extract name="Voc" x.val from curve(v."anode", i."cathode") where y.val=0.0
extract name="Pm" max(curve(v."anode", (v."anode" * i."cathode")))
extract name="Vm" x.val from curve(v."anode", (v."anode"*i."cathode") ) \
      where y.val=$"Pm"
extract name="Im" $"Pm"/$"Vm"
extract name="FF" $"Pm"/($"Isc"*$"Voc")*100
extract name="EFF" (1e8*$Pm/0.1)*100
extract name="iv" curve(v."anode", (i."cathode"*1e11)) outf="basi2homo1_2.log"

quit
```

2. Example Silvaco Atlas code for finding *EQE* for a $BaSi_2$ homojunction solar cell

```
# Mesh, region, doping, material properties, method, and models statements all appear before this point

beam number=1 x.orig=0.5 y.orig=-0.02 angle=90 back.refl
solve init
solve previous
solve b1=1e-2
solve b1=1e-1

log outfile=BaSi13_EQE_1.log
solve b1=1e-1 beam=1 lambda=0.3 wstep=0.01 wfinal=1.2
log off

extract init infile="BaSi13_EQE_1.log"
extract name="EQE" curve(elect."optical wavelength", (-i."anode")/(elect."source photo current")) outf="BaSi13_EQE_2.log"
extract name="IQE" curve(elect."optical wavelength", (-i."anode")/(elect."available photo current")) outf="BaSi13_EQE_3.log"

tonyplot BaSi13_EQE_2.log

quit
```

3. Example Silvaco Atlas code for finding η for a $BaSi_2$/c-Si tandem solar cell

```
go atlas

#top n+-BaSi2
set top1thick=0.02
set top1con=1e20

#top p-BaSi2
set top2thick=0.5
set top2con=5e17

#top p+-BaSi2
set top3thick=0.02
set top3con=1e20

#tunnel p+-BaSi2
set tun1topthick=0.015
set tun1topcon=1e20

#tunnel n+-Si
set tun1botthick=0.015
```

```
set tun1botcon=1e20

#bot n+-Si
set bot1thick=0.1
set bot1con=1e20

#bot p-Si
set bot2thick=200
set bot2con=7e17

#bot p+-Si
set bot3thick=1
set bot3con=1e20

set topcellthick=$top1thick+$top2thick+$top3thick

set tunthick=$tun1topthick+$tun1botthick

set totcellthick=$topcellthick+$tunthick+$bot1thick+$bot2thick+$bot3thick

#mesh auto
mesh auto
x.mesh loc=0.0 spac=0.1
x.mesh loc=1.0 spac=0.1

#mesh.y
y.mesh loc=0.0 spac=0.1
y.mesh loc=$top1thick spac=0.1*$top1thick
y.mesh loc=$top1thick+$top2thick spac=0.1*$top2thick
y.mesh loc=$topcellthick spac=0.1*$top3thick
y.mesh loc=$topcellthick+$tun1topthick spac=$tun1topthick/15
y.mesh loc=$topcellthick+$tun1topthick+$tun1botthick spac=$tun1botthick/15
y.mesh loc=$topcellthick+$tunthick+$bot1thick spac=0.1*$bot1thick
y.mesh loc=$topcellthick+$tunthick+$bot1thick+$bot2thick spac=0.1*$bot2thick
y.mesh loc=$totcellthick spac=0.1*$bot3thick

#regions
region number=1 name="n+-BaSi2" user.material=BaSi2 y.min=0 y.max=$top1thick
region number=2 name="p-BaSi2" user.material=BaSi2 y.min=$top1thick y.max=$top1thick+$top2thick
region number=3 name="p+-BaSi2" user.material=BaSi2 y.min=$top1thick+$top2thick y.max=$topcellthick
region number=4 name=anode1 user.material=BaSi2 y.min=$topcellthick y.max=$topcellthick+$tun1topthick
region number=5 name=cathode1 material=Silicon y.min=$topcellthick+$tun1topthick
y.max=$topcellthick+$tun1topthick+$tun1botthick
region number=6 name="n-Si" material=Silicon y.min=$topcellthick+$tunthick
y.max=$topcellthick+$tunthick+$bot1thick
```

```
region number=7 name="p-Si" material=Silicon y.min=$topcellthick+$tunthick+$bot1thick y.max=$topcellthick+$tunthick+$bot1thick+$bot2thick
region number=8 name="p+-Si" material=Silicon y.min=$topcellthick+$tunthick+$bot1thick+$bot2thick y.max=$totcellthick

#electrode
electrode num=1 name=cathode top material=ITO
electrode num=2 name=anode1 material=BaSi2 y.min=$topcellthick y.max=$topcellthick+$tun1topthick
electrode num=3 name=cathode1 material=Silicon y.min=$topcellthick+$tun1topthick y.max=$topcellthick+$tun1topthick+$tun1botthick
electrode num=4 name=anode bottom material=Aluminum

#contact
contact name=anode1 resist=5E16
contact name=cathode1 resist=5E16

#doping
doping region=1 uniform n.type conc=$top1con
doping region=2 uniform p.type conc=$top2con
doping region=3 uniform p.type conc=$top3con
doping region=4 uniform p.type conc=$tun1topcon
doping region=5 uniform n.type conc=$tun1botcon
doping region=6 uniform n.type conc=$bot1con
doping region=7 uniform p.type conc=$bot2con
doping region=8 uniform p.type conc=$bot3con

#material
material material=BaSi2 user.group=semiconductor user.default=silicon index.file=BaSi17.nk EG300=1.7 PERMITTIVITY=14 AFFINITY=3.2 NC300=2.6e19 NV300=2.0e19
material material=silicon EG300=1.12 PERMITTIVITY=11.7 AFFINITY=4.05 NC300=2.80e19 NV300=1.04e19 sopra=Si111.nk
material material=Aluminum sopra=Al.nk
material region=1 MUN=500 MUP=20 taun0=3e-6 taup0=3e-6
material region=2 MUN=850 MUP=100 taun0=8e-6 taup0=8e-6
material region=3 MUN=600 MUP=30 taun0=2e-6 taup0=2e-6

#model
model srh fermi conmob temp=300 print

#method
method newton maxtraps=10 dvmax=0.1
output con.band val.band

beam number=1 x.orig=0.5 y.orig=-0.02 angle=90 power.file=am15.spec back.refl wavel.start=0.28 wavel.end=4 wavel.num=2002
```

```
solve init
solve previous
solve b1=1e-2
solve b1=1e-1
solve b1=1e0

log outfile=basi17tandem_10_tot_1.log
solve vanode=0.0 name=anode vstep=0.02 vfinal=2.0
log off

extract init infile="basi17tandem_10_tot_1.log"
extract name="Isc" y.val from curve(v."anode", i."cathode") where x.val=0.0
extract name="JscmAcm2" $Isc*1e08*1e03
extract name="Voc" x.val from curve(v."anode", i."cathode") where y.val=0.0
extract name="Pm" max(curve(v."anode", (v."anode" * i."cathode")))
extract name="Vm" x.val from curve(v."anode", (v."anode"*i."cathode") ) \
      where y.val=$"Pm"
extract name="Im" $"Pm"/$"Vm"
extract name="FF" $"Pm"/($"Isc"*$"Voc")*100
extract name="EFF" (1e8*$Pm/0.1)*100
extract name="iv" curve(v."anode", (i."cathode"*1e11)) outf="basi17tandem_10_tot_2.log"

quit
```

4. Example Silvaco Atlas code for finding *EQE* for a $BaSi_2$/c-Si tandem solar cell

```
# Mesh, region, doping, material properties, method, and models statements all appear before this point

# EQE of top cell
beam num=1 x.orig=0.5 y.orig=-0.02 angle=90 back.refl

beam num=2 x.orig=0.5 y.orig=-0.02 angle=90 wavelength=0.9 back.refl

solve init

solve b2=1e-2
solve b2=1e-1
solve b2=1e0
log outfile=tmp1.log
solve b2=1e1
extract init inf="tmp1.log"
extract name="ISi" max(abs(i."anode"))

log off
```

```
solve b1=1e-2
log outfile=BaSi17tandem_top*EQE*_1.log
solve b1=1e-1 beam=1 lambda=0.3 wstep=0.01 wfinal=1.2

log off

extract init infile="BaSi17tandem_top*EQE*_1.log"
extract name="BaSi17tandem_top*EQE*_2.log" curve(elect."optical wavelength", (-i."anode"-$ISi)/(elect."source photo current")) outfile="BaSi17tandem_top*EQE*_2.log"

# *EQE* of bottom cell
beam num=3 x.orig=0.5 y.orig=-0.02 angle=90 back.refl

beam num=4 x.orig=0.5 y.orig=-0.02 angle=90 wavelength=0.65 back.refl

solve init

solve b4=1e-2
solve b4=1e-1
solve b4=1e0
log outfile=bottmp1.log
solve b4=1e1
extract init inf="bottmp1.log"
extract name="IBaSi2" max(abs(i."anode"))

log off

solve b3=1e-2
log outfile=BaSi17tandem_bot*EQE*_1.log
solve b3=1e-1 beam=3 lambda=0.3 wstep=0.01 wfinal=1.2

log off

extract init infile="BaSi17tandem_bot*EQE*_1.log"
extract name="BaSi17tandem_bot*EQE*_2.log" curve(elect."optical wavelength", (-i."anode"-$IBaSi2)/(elect."source photo current")) outfile="BaSi17tandem_bot*EQE*_2.log"

quit
```

Appendix B. Correspondence table between sample number and sample name.

Sample No.	Name	Sample No.	Name
A	Ref. [92] (Morita)	H3	TG25
B1	ME03 (Emha)	H4	TG26
B2	ME04 (Emha)	H5	TG27
B3	BD10 (Takeuchi)	H6	TG28
B4	BD11 (Takeuchi)	I1	TG15
B5	BD06 (Takeuchi)	I2	TG16
C1	TG06	I3	TG20
C2	TG04	I4	TG17
C3	TG05	I5	TG18
C4	TG03	I6	TG19
C5	TG02	I7	TG05
D1	DT05	J1	TG07
D2	OJ01 (Takabe)	J2	TG08
E1	DT08	J3	TG09
E2	DT10	J4	TG10
E3	DT11	J5	TG11
E4	DT32	J6	TG12
E5	DT33	J7	TG13
E6	DT29	J8	TG14
F1	DT26	K1	KG14
F2	DT31	K2	KG16
F3	DT28	K3	KG13
F4	DT30	K4	KG15
F5	DT22	K5	KG11
G1	DT19	K6	KG12
G2	DT20	L1	KG19
G3	DT21	L2	KG26
G4	DT23	M1	KG22
H1	TG23	M2	KG42
H2	TG24		

References

[1] R. Perez and M. Perez, IEA SHC Solar Update (2009).

[2] APS News, American Physical Society **18** (2009) 4.

[3] Renewables 2018 Global Status Report, REN21 (2018).

[4] S. Philipps, Photovoltaics Report, Fraunhofer ISE (2018).

[5] M. A. M. Al-Alwani, A. B. Mohamad, N. A. Ludin, A. A. H. Kadhum, and K. Sopian, Renew. Sust. Energ. Rev. **65** (2016) 183.

[6] P. K. Nayak, G. Garcia-Belmonte, A. Kahn, J. Bisquert, and D. Cahen, Energy Environ. Sci. **5** (2012) 6022.

[7] W. Shockley and H. J. Queisser, J. Appl. Phys. **32** (1961) 510.

[8] M. A. Green and M. J. Keevers, Prog. Photovolt: Res. Appl. **3** (1995) 189.

[9] K. Yoshikawa, H. Kawasaki, W. Yoshida, T. Irie, K. Konishi, K. Nakano, T. Uto, D. Adachi, M. Kanematsu, H. Uzu, and K. Yamamoto, Nat. Energy **2** (2017) 17032.

[10] A. Polman, M. Knight, E. C. Garnett, B. Ehrler, and W. C. Sinke, Science **352** (2016) aad4424.

[11] K. L. Chopra, P. D. Paulson, and V. Dutta, Prog. Photovolt: Res. Appl. **12** (2004) 69.

[12] B. D and R. H, in 1972 9th IEEE Photovoltaic Specialists Conference (PVSC), 1972, p. 129.

[13] First Solar Press Release, First Solar Achieves yet another cell conversion efficiency world record (24 February 2016).

[14] M. A. Green, Y. Hishikawa, E. D. Dunlop, D. H. Levi, J. Hohl-Ebinger, and A. W. Y. Ho-Baillie, Prog. Photovolt: Res. Appl. **26** (2018) 427.

[15] M. Gloeckler, I. Sankin, and Z. Zhao, IEEE J. Photovolt. **3** (2013) 1389.

[16] P. D. Paulson, R. W. Birkmire, and W. N. Shafarman, J. Appl. Phys. **94** (2003) 879.

[17] A. Bosio, N. Romeo, A. Podestà, S. Mazzamuto, and V. Canevari, Cryst. Res. Technol. **40** (2005) 1048.

[18] S. Oonishi, M. Kawamura, N. Takano, D. Hashimoto, A. Yamada, and M. Konagai, Thin Solid Films **519** (2011) 7347.

[19] L. L. Kazmerski, F. R. White, and G. K. Morgan, Appl. Phys. Lett. **29** (1976) 268.

[20] T. Prabhakar and N. Jampana, Sol. Energy Mater. Sol. Cells **95** (2011) 1001.

[21] K. Ramanathan, J. Mann, S. Glynn, S. Christensen, J. Pankow, J. Li, J. Scharf, L. Mansfield, M. Contreras, and R. Noufi, in 2012 38th IEEE Photovoltaic Specialists Conference, 2012, p. 001677.

[22] T. Kato, J. Wu, Y. Hirai, H. Sugimoto, and V. Bermudez, IEEE J. Photovolt. **9** (2019) 325.

[23] T. Todorov, T. Gershon, O. Gunawan, Y. S. Lee, C. Sturdevant, L.-Y. Chang, and S. Guha, Adv. Energy Mater. **5** (2015) 1500799.

[24] C. D. Bailie, M. G. Christoforo, J. P. Mailoa, A. R. Bowring, E. L. Unger, W. H. Nguyen, J. Burschka, N. Pellet, J. Z. Lee, M. Grätzel, R. Noufi, T. Buonassisi, A. Salleo, and M. D. McGehee, Energy Environ. Sci. **8** (2015) 956.

[25] W. Wang, M. T. Winkler, O. Gunawan, T. Gokmen, T. K. Todorov, Y. Zhu, and D. B. Mitzi, Adv. Energy Mater. **4** (2013) 1301465.

[26] W. Paul and D. A. Anderson, Sol. Energy Mater. **5** (1981) 229.

[27] D. E. Carlson and C. R. Wronski, Appl. Phys. Lett. **28** (1976) 671.

[28] E. Yablonovitch and G. D. Cody, IEEE Trans. Electron Devices **29** (1982) 300.

[29] C. Algora and V. Díaz, Prog. Photovolt: Res. Appl. **8** (2000) 211.

[30] C. Algora, E. Ortiz, I. Rey-Stolle, V. Diaz, R. Pena, V. M. Andreev, V. P. Khvostikov, and V. D. Rumyantsev, IEEE Trans. Electron Devices **48** (2001) 840.

[31] X. Wang, M. R. Khan, J. L. Gray, M. A. Alam, and M. S. Lundstrom, IEEE J. Photovolt. **3** (2013) 737.

[32] D. V. Shenai-Khatkhate, R. J. Goyette, R. L. DiCarlo Jr, and G. Dripps, J. Cryst. Growth **272** (2004) 816.
[33] J. S. Manser, J. A. Christians, and P. V. Kamat, Chem. Rev. **116** (2016) 12956.
[34] S. D. Stranks, G. E. Eperon, G. Grancini, C. Menelaou, M. J. P. Alcocer, T. Leijtens, L. M. Herz, A. Petrozza, and H. J. Snaith, Science **342** (2013) 341.
[35] V. D'Innocenzo, G. Grancini, M. J. P. Alcocer, A. R. S. Kandada, S. D. Stranks, M. M. Lee, G. Lanzani, H. J. Snaith, and A. Petrozza, Nat. Commun. **5** (2014) 3586.
[36] S. Collavini, S. F. Völker, and J. L. Delgado, Angew. Chem. Int. Edit **54** (2015) 9757.
[37] A. Kojima, K. Teshima, Y. Shirai, and T. Miyasaka, J. Am. Chem. Soc. **131** (2009) 6050.
[38] J.-H. Im, C.-R. Lee, J.-W. Lee, S.-W. Park, and N.-G. Park, Nanoscale **3** (2011) 4088.
[39] W. S. Yang, B.-W. Park, E. H. Jung, N. J. Jeon, Y. C. Kim, D. U. Lee, S. S. Shin, J. Seo, E. K. Kim, J. H. Noh, and S. I. Seok, Science **356** (2017) 1376.
[40] H. J. Snaith, A. Abate, J. M. Ball, G. E. Eperon, T. Leijtens, N. K. Noel, S. D. Stranks, J. T.-W. Wang, K. Wojciechowski, and W. Zhang, J. Phys. Chem. Lett **5** (2014) 1511.
[41] A. Babayigit, A. Ethirajan, M. Muller, and B. Conings, Nat. Mater. **15** (2016) 247.
[42] D. B. Migas, V. L. Shaposhnikov, and V. E. Borisenko, Phys. Status Solidi (b) **244** (2007) 2611.
[43] M. Kumar, N. Umezawa, and M. Imai, Appl. Phys. Express **7** (2014) 071203.
[44] K. Toh, T. Saito, and T. Suemasu, Jpn. J. Appl. Phys. **50** (2011) 068001.
[45] K. Morita, M. Kobayashi, and T. Suemasu, Thin Solid Films **515** (2007) 8216.
[46] Y. Imai and A. Watanabe, Intermetallics **18** (2010) 1432.
[47] M. Baba, M. Kohyama, and T. Suemasu, J. Appl. Phys. **120** (2016) 085311.
[48] M. Baba, K. Toh, K. Toko, N. Saito, N. Yoshizawa, K. Jiptner, T. Sekiguchi, K. O. Hara, N. Usami, and T. Suemasu, J. Cryst. Growth **348** (2012) 75.
[49] M. Baba, K. Watanabe, K. O. Hara, K. Toko, T. Sekiguchi, N. Usami, and T. Suemasu, Jpn. J. Appl. Phys. **53** (2014) 078004.
[50] K. O. Hara, N. Usami, K. Nakamura, R. Takabe, M. Baba, K. Toko, and T. Suemasu, Appl. Phys. Express **6** (2013) 112302.
[51] K. O. Hara, N. Usami, K. Toh, M. Baba, K. Toko, and T. Suemasu, J. Appl. Phys. **112** (2012) 083108.
[52] Y. Imai and A. Watanabe, Intermetallics **15** (2007) 1291.
[53] R. Takabe, T. Deng, K. Kodama, Y. Yamashita, T. Sato, K. Toko, and T. Suemasu, J. Appl. Phys. **123** (2018) 045703.
[54] M. Ajmal Khan, K. O. Hara, W. Du, M. Baba, K. Nakamura, M. Suzuno, K. Toko, N. Usami, and T. Suemasu, Appl. Phys. Lett. **102** (2013) 112107.
[55] M. Takeishi, Y. Matsumoto, R. Sasaki, T. Saito, and T. Suemasu, Phys. Procedia **11** (2011) 27.
[56] M. Kobayashi, K. Morita, and T. Suemasu, Thin Solid Films **515** (2007) 8242.
[57] Z. Xu, T. Deng, R. Takabe, K. Toko, and T. Suemasu, J. Cryst. Growth **471** (2017) 37.
[58] R. Takabe, M. Baba, K. Nakamura, W. Du, M. A. Khan, S. Koike, K. Toko, K. O. Hara, N. Usami, and T. Suemasu, Phys. Status Solidi (c) **10** (2013) 1753.
[59] K. O. Hara, Y. Hoshi, N. Usami, Y. Shiraki, K. Nakamura, K. Toko, and T. Suemasu, Thin Solid Films **557** (2014) 90.
[60] M. Kobayashi, Y. Matsumoto, Y. Ichikawa, D. Tsukada, and T. Suemasu, Appl. Phys. Express **1** (2008) 051403.
[61] R. A. McKee, F. J. Walker, J. R. Conner, and R. Raj, Appl. Phys. Lett. **63** (1993) 2818.
[62] Y. Inomata, T. Nakamura, T. Suemasu, and F. Hasegawa, Jpn. J. Appl. Phys. **43** (2004) 4155.
[63] Y. Inomata, T. Nakamura, T. Suemasu, and F. Hasegawa, Jpn. J. Appl. Phys. **43** (2004) L478.

[64] K. Toh, K. O. Hara, N. Usami, N. Saito, N. Yoshizawa, K. Toko, and T. Suemasu, J. Cryst. Growth **345** (2012) 16.
[65] M. Baba, K. Toh, K. Toko, K. O. Hara, N. Usami, N. Saito, N. Yoshizawa, and T. Suemasu, J. Cryst. Growth **378** (2013) 193.
[66] T. Yoneyama, A. Okada, M. Suzuno, T. Shibutami, K. Matsumaru, N. Saito, N. Yoshizawa, K. Toko, and T. Suemasu, Thin Solid Films **534** (2013) 116.
[67] S. Matsuno, R. Takabe, S. Yokoyama, K. Toko, M. Mesuda, H. Kuramochi, and T. Suemasu, Appl. Phys. Express **11** (2018) 071401.
[68] K. Yamaya, Y. Yamaki, H. Nakanishi, and S. Chichibu, Appl. Phys. Lett. **72** (1998) 235.
[69] C. Thi Trinh, Y. Nakagawa, K. O. Hara, R. Takabe, T. Suemasu, and N. Usami, Mater. Res. Express **3** (2016) 076204.
[70] K. O. Hara, Y. Nakagawa, T. Suemasu, and N. Usami, Jpn. J. Appl. Phys. **54** (2015) 07JE02.
[71] K. O. Hara, C. T. Trinh, K. Arimoto, J. Yamanaka, K. Nakagawa, Y. Kurokawa, T. Suemasu, and N. Usami, J. Appl. Phys. **120** (2016) 045103.
[72] T. Suemasu and N. Usami, J. Phys. D: Appl. Phys. **50** (2017) 023001.
[73] T. Suemasu, K. Morita, M. Kobayashi, M. Saida, and M. Sasaki, Jpn. J. Appl. Phys. **45** (2006) L519.
[74] S. Yachi, R. Takabe, H. Takeuchi, K. Toko, and T. Suemasu, Appl. Phys. Lett. **109** (2016) 072103.
[75] W. Du, M. Baba, K. Toko, K. O. Hara, K. Watanabe, T. Sekiguchi, N. Usami, and T. Suemasu, J. Appl. Phys. **115** (2014) 223701.
[76] K. Kodama, R. Takabe, T. Deng, K. Toko, and T. Suemasu, Jpn. J. Appl. Phys. **57** (2018) 050310.
[77] D. Tsukahara, S. Yachi, H. Takeuchi, R. Takabe, W. Du, M. Baba, Y. Li, K. Toko, N. Usami, and T. Suemasu, Appl. Phys. Lett. **108** (2016) 152101.
[78] S. Yachi, R. Takabe, K. Toko, and T. Suemasu, Jpn. J. Appl. Phys. **56** (2017) 05DB03.
[79] T. Saito, Y. Matsumoto, R. Sasaki, M. Takeishi, and T. Suemasu, Jpn. J. Appl. Phys. **49** (2010) 068001.
[80] T. Saito, Y. Matsumoto, M. Suzuno, M. Takeishi, R. Sasaki, T. Suemasu, and N. Usami, Appl. Phys. Express **3** (2010) 021301.
[81] T. Suemasu, T. Saito, K. Toh, A. Okada, and M. A. Khan, Thin Solid Films **519** (2011) 8501.
[82] W. Du, M. Suzuno, M. Ajmal Khan, K. Toh, M. Baba, K. Nakamura, K. Toko, N. Usami, and T. Suemasu, Appl. Phys. Lett. **100** (2012) 152114.
[83] Y. Yamashita, S. Yachi, R. Takabe, T. Sato, M. E. Bayu, K. Toko, and T. Suemasu, Jpn. J. Appl. Phys. **57** (2018) 025501.
[84] A. L. Fripp, J. Appl. Phys. **46** (1975) 1240.
[85] J. Y. W. Seto, J. Appl. Phys. **46** (1975) 5247.
[86] G. Baccarani, B. Ricc ò, and G. Spadini, J. Appl. Phys. **49** (1978) 5565.
[87] C. M. Wolfe, G. E. Stillman, and W. T. Lindley, J. Appl. Phys. **41** (1970) 3088.
[88] M. Grundmann, in *The Physics of Semiconductors*, 3rd ed. (Springer, Berlin, Heidelberg, 2016).
[89] M. C. Bost and J. E. Mahan, J. Appl. Phys. **64** (1988) 2034.
[90] D. Leong, M. Harry, K. J. Reeson, and K. P. Homewood, Nature **387** (1997) 686.
[91] K. Takakura, H. Ohyama, K. Takarabe, T. Suemasu, and F. Hasegawa, J. Appl. Phys. **97** (2005) 093716.
[92] D. B. Migas, V. O. Bogorodz, A. V. Krivosheeva, V. L. Shaposhnikov, A. B. Filonov, and V. E. Borisenko, Jpn. J. Appl. Phys. **56** (2017) 05DA03.
[93] K. Morita, Y. Inomata, and T. Suemasu, Thin Solid Films **508** (2006) 363.
[94] M. A. Khan, K. Nakamura, W. Du, K. Toko, N. Usami, and T. Suemasu, Appl. Phys. Lett. **104** (2014) 252104.
[95] Y. Matsumoto, D. Tsukada, R. Sasaki, M. Takeishi, T. Saito, T. Suemasu, N. Usami, and M. Sasase, Jpn.

J. Appl. Phys. **49** (2010) 04DP05.
[96] B. Masakazu, N. Kotaro, D. Weijie, M. A. Khan, K. Shintaro, T. Kaoru, U. Noritaka, S. Noriyuki, Y. Noriko, and S. Takashi, Jpn. J. Appl. Phys. **51** (2012) 098003.
[97] V. E. Borisenko, in *Semiconducting Silicides*, 1st ed. (Springer Series in Materials Science, 2000).
[98] D. B. Migas, V. L. Shaposhnikov, A. B. Filonov, V. E. Borisenko, and N. N. Dorozhkin, Phys. Rev. B **77** (2008).
[99] A. B. Filonov, I. E. Tralle, D. B. Migas, V. L. Shaposhnikov, and V. E. Borisenko, Phys. Status Solidi (b) **203** (1997) 183.
[100] A. E. Krivosheev, L. I. Ivanenko, A. B. Filonov, V. L. Shaposhnikov, G. Behr, J. Schumann, and V. E. Borisenko, Semiconductors **40** (2006) 27.
[101] A. B. Filonov, A. E. Krivosheev, L. I. Ivanenko, G. Behr, J. Schumann, D. Souptel, and V. E. Borisenko, Semiconductors **39** (2005) 395.
[102] B. K. Ridley, in *Quantum Processes in Semiconductors*, 5th ed. (OUP Oxford, 2013).
[103] K. Hashimoto, K. Kurosaki, Y. Imamura, H. Muta, and S. Yamanaka, J. Appl. Phys. **102** (2007) 063703.
[104] H. Peng, C. L. Wang, J. C. Li, R. Z. Zhang, M. X. Wang, H. C. Wang, Y. Sun, and M. Sheng, Phys. Lett. A **374** (2010) 3797.
[105] N. A. Poklonski, S. A. Vyrko, V. I. Yatskevich, and A. A. Kocherzhenko, J. Appl. Phys. **93** (2003) 9749.
[106] M. Baba, S. Tsurekawa, K. Watanabe, W. Du, K. Toko, K. O. Hara, N. Usami, T. Sekiguchi, and T. Suemasu, Appl. Phys. Lett. **103** (2013) 142113.
[107] M. Kumar, N. Umezawa, W. Zhou, and M. Imai, J. Mater. Chem. A **5** (2017) 25293.
[108] V. F. Gantmakher and Y. B. Levinson, in *Carrier Scattering in Metals and Semiconductors*, 3rd ed. (North Holland, New York, 1987).
[109] D. Tsukahara, M. Baba, S. Honda, Y. Imai, K. O. Hara, N. Usami, K. Toko, J. H. Werner, and T. Suemasu, J. Appl. Phys. **116** (2014) 123709.
[110] W. Du, R. Takabe, S. Yachi, K. Toko, and T. Suemasu, Thin Solid Films **629** (2017) 17.
[111] H. F. Mataré, in *Defect Electronics in Semiconductors* (Wiley-Interscience, New York, 1971).
[112] K. Seeger, in *Semiconductor Physics*, 9th ed. (Springer, Berlin, Heidelberg, 2004).
[113] B. Dale and H. G. Rudenberg, in Proceedings of the 14th Annual Power Sources Conference, 1960.
[114] J. Müller, B. Rech, J. Springer, and M. Vanecek, Sol. Energy **77** (2004) 917.
[115] M. Despeisse, G. Bugnon, A. Feltrin, M. Stueckelberger, P. Cuony, F. Meillaud, A. Billet, and C. Ballif, Appl. Phys. Lett. **96** (2010) 073507.
[116] F. J. Haug, K. Söderström, A. Naqavi, and C. Ballif, J. Appl. Phys. **109** (2011) 084516.
[117] H. Sai, T. Matsui, T. Koida, K. Matsubara, M. Kondo, S. Sugiyama, H. Katayama, Y. Takeuchi, and I. Yoshida, Appl. Phys. Lett. **106** (2015) 213902.
[118] T. Tayagaki, D. Furuta, O. Aonuma, I. Takahashi, Y. Hoshi, Y. Kurokawa, and N. Usami, Jpn. J. Appl. Phys. **56** (2017) 04CS01.
[119] J. B. Nelson and D. P. Riley, Proc. Phys. Soc **57** (1945) 160.
[120] J. R. Sites and P. H. Mauk, Sol. Cells **27** (1989) 411.
[121] S. Yachi, R. Takabe, T. Deng, K. Toko, and T. Suemasu, Jpn. J. Appl. Phys. **57** (2018) 042301.
[122] R. A. McKee, F. J. Walker, J. R. Conner, E. D. Specht, and D. E. Zelmon, Appl. Phys. Lett. **59** (1991) 782.
[123] K. Takahashi, Y. Nakagawa, K. O. Hara, I. Takahashi, Y. Kurokawa, and N. Usami, MRS Adv. **3** (2018) 1435.
[124] K. Takahashi, Y. Nakagawa, K. O. Hara, Y. Kurokawa, and N. Usami, Jpn. J. Appl. Phys. **56** (2017) 05DB04.

[125] M. Baba, K. O. Hara, D. Tsukahara, K. Toko, N. Usami, T. Sekiguchi, and T. Suemasu, J. Appl. Phys. **116** (2014) 235301.
[126] R. Varache, C. Leendertz, M. E. Gueunier-Farret, J. Haschke, D. Muñoz, and L. Korte, Sol. Energy Mater. Sol. Cells **141** (2015) 14.
[127] Y. Terai, H. Yamaguchi, H. Tsukamoto, N. Murakoso, M. Iinuma, and T. Suemasu, Jpn. J. Appl. Phys. **56** (2017) 05DD02.
[128] L. Yang, X. Cui, J. Zhang, K. Wang, M. Shen, S. Zeng, S. A. Dayeh, L. Feng, and B. Xiang, Sci. Rep. **4** (2014) 5649.
[129] M. Grundmann, in *The Physics of Semiconductors*, 3rd ed. (Springer, Berlin, Heidelberg, 2016).
[130] Y. Imai and A. Watanabe, Intermetallics **10** (2002) 333.
[131] M. Baba, K. Ito, W. Du, T. Sanai, K. Okamoto, K. Toko, S. Ueda, Y. Imai, A. Kimura, and T. Suemasu, J. Appl. Phys. **114** (2013) 123702.
[132] W. Du, T. Saito, M. A. Khan, K. Toko, N. Usami, and T. Suemasu, Jpn. J. Appl. Phys. **51** (2012) 04DP01.
[133] N. Zhang, K. Nakamura, M. Baba, K. Toko, and T. Suemasu, Jpn. J. Appl. Phys. **53** (2014) 04ER02.
[134] G. Fuse, T. Hirao, K. Inoue, S. Takayanagi, and Y. Yaegashi, J. Appl. Phys. **53** (1982) 3650.
[135] N. Zhang, K. Nakamura, M. Baba, K. Toko, and T. Suemasu, Phys. Status Solidi (c) **10** (2013) 1762.
[136] T. Suemasu, Jpn. J. Appl. Phys. **54** (2015) 07JA01.
[137] T. Deng, T. Sato, Z. Xu, R. Takabe, S. Yachi, Y. Yamashita, K. Toko, and T. Suemasu, Appl. Phys. Express **11** (2018) 062301.
[138] A. Pokhrel, L. Samad, F. Meng, and S. Jin, Nanoscale **7** (2015) 17450.
[139] R. Vismara, O. Isabella, and M. Zeman, Opt. Express **25** (2017) A402.
[140] R. Vismara, O. Isabella, and M. Zeman, Proc. SPIE **9898** (2016) 98980J.
[141] D. A. Clugston and P. A. Basore, in 1997 26th IEEE Photovoltaic Specialists Conference, 1997, p. 207.
[142] M. Burgelman, K. Decock, S. Khelifi, and A. Abass, Thin Solid Films **535** (2013) 296.
[143] K. Kim, J. Gwak, S. K. Ahn, Y.-J. Eo, J. H. Park, J.-S. Cho, M. G. Kang, H.-E. Song, and J. H. Yun, Sol. Energy **145** (2017) 52.
[144] Y. Liu, Y. Sun, and A. Rockett, Sol. Energy Mater. Sol. Cells **98** (2012) 124.
[145] A. Nakanishi, Y. Takiguchi, and S. Miyajima, Phys. Status Solidi (a) **213** (2016) 1997.
[146] Atlas User's Manual: Device Simulation Software from Silvaco International, Version 5.26.1.R, 10 April, 2018.
[147] M. Baudrit and C. Algora, in 2008 33rd IEEE Photovoltaic Specialists Conference, 2008, p. 1.
[148] M. H. Tsutagawa and S. Michael, in 2009 34th IEEE Photovoltaic Specialists Conference, 2009, p. 001954.
[149] M. Elbar, S. Tobbeche, and A. Merazga, Sol. Energy **122** (2015) 104.
[150] S. Michael, A. D. Bates, and M. S. Green, in 2005 31st IEEE Photovoltaic Specialists Conference, 2005, p. 719.
[151] T. Deng, T. Suemasu, D. A. Shohonov, I. S. Samusevich, A. B. Filonov, D. B. Migas, and V. E. Borisenko, Thin Solid Films **661** (2018) 7.
[152] R. Takabe, K. O. Hara, M. Baba, W. Du, N. Shimada, K. Toko, N. Usami, and T. Suemasu, J. Appl. Phys. **115** (2014) 193510.
[153] Silvaco, 2018. solarex16.in: High efficiency silicon solar cell. (https://www.silvaco.com/examples/tcad/section44/example16/index.html).
[154] D. F. Swinehart, J. Chem. Educ. **39** (1962) 333.
[155] T. Deng, K. Gotoh, R. Takabe, Z. Xu, S. Yachi, Y. Yamashita, K. Toko, N. Usami, and T. Suemasu, J.

Cryst. Growth **475** (2017) 186.
[156] Z. Xu, K. Gotoh, T. Deng, T. Sato, K. Toko, U. Noritaka, and S. Takashi, in 2018 IEEE 7th World Conference on Photovoltaic Energy Conversion (WCPEC) (A Joint Conference of 45th IEEE PVSC, 28th PVSEC & 34th EU PVSEC), 2018, p. 1871.
[157] B. M. Kayes, H. Nie, R. Twist, S. G. Spruytte, F. Reinhardt, I. C. Kizilyalli, and G. S. Higashi, in 2011 37th IEEE Photovoltaic Specialists Conference, 2011, p. 000004.
[158] W. S. Yang, J. H. Noh, N. J. Jeon, Y. C. Kim, S. Ryu, J. Seo, and S. I. Seok, Science **348** (2015) 1234.
[159] T. Matsui, A. Bidiville, K. Maejima, H. Sai, T. Koida, T. Suezaki, M. Matsumoto, K. Saito, I. Yoshida, and M. Kondo, Appl. Phys. Lett. **106** (2015) 053901.
[160] M. Umeno, T. Soga, K. Baskar, and T. Jimbo, Sol. Energy Mater. Sol. Cells **50** (1998) 203.
[161] Q. Han, Y.-T. Hsieh, L. Meng, J.-L. Wu, P. Sun, E.-P. Yao, S.-Y. Chang, S.-H. Bae, T. Kato, V. Bermudez, and Y. Yang, Science **361** (2018) 904.
[162] K. A. Bush, A. F. Palmstrom, Z. J. Yu, M. Boccard, R. Cheacharoen, J. P. Mailoa, D. P. McMeekin, R. L. Z. Hoye, C. D. Bailie, T. Leijtens, I. M. Peters, M. C. Minichetti, N. Rolston, R. Prasanna, S. Sofia, D. Harwood, W. Ma, F. Moghadam, H. J. Snaith, T. Buonassisi, Z. C. Holman, S. F. Bent, and M. D. McGehee, Nat. Energy **2** (2017) 17009.

Acknowledge

Here, I want to thank many people, without whom it would be impossible for me to finish my Ph.D program.

First and foremost, I would like to gratefully appreciate my supervisor Prof. T. Suemasu, who has been a tremendous mentor for me, for his enthusiasm, patience, motivation, and broad knowledge. His advices on both research as well as life have been priceless and he always encourages me to enjoy the life in Tsukuba. As an international student, he helps me a lot not only on supporting me financially but also providing opportunities to attend international conferences. I could not have imagined having a better supervisor for my Ph.D study.

In addition to my supervisor, I would like to thank my thesis committee members, Prof. N. Sano, Prof. T. Sekiguchi, Dr. T. Sakurai and Prof. M. Imai, for letting my defense be an enjoyable moment, and for their brilliant comments and helpful suggestions.

I would also like to thank Dr. K. Toko, who is really a hardworking researcher. He is a good role model for me. Besides, I would express my appreciate to Prof. N. Usami, Dr. K. Gotoh of Nagoya University and Dr. K. O. Hara of University of Yamanashi, who helped me when I performed EBSD in Nagoya University. Thanks to Prof. H. Tadano for useful suggestions on Silvaco Atlas software.

Special thanks to Prof. Yun Gao from Hubei University for introducing me to this nice laboratory. Thank Madam E. Ito, who helps me deal with the travel expense reimbursement every time after attending domestic or international conferences.

I would like to thank the lab members; T. Gushi, T. Sato, K. Moto, H. Murata, Z. Xu, Y. Yamashita, K. Kodama, S. Matsuno, A. Anzai, T. Imajo, D. Takahara, K. Kusano, R. Sugiyama, S. Sugiyama, Y, Nakajima, T. Nishida, Louise Benincasa, S. Aoniki, M, Saito, M. Tsuji, T. Nemoto, T. Hirose, and graduated R. Takabe, Y. Li, S. Yachi, M. Emha Bayu…… I will not forget the great moment when we travelled Nikko, Mt. Fuji, and Nasu during summer seminar. Your company made my study much easier and happier.

Thanks D. Liu, Y. Wu, Z. Xu, and all my friends in Tsukuba. I am happy to clime Mt. Fuji to see sunrise and participate in Tsukuba Marathon with you.

Last but not the least, I must express my very profound gratitude to my parents. Words cannot express how grateful I am to my father and mother for all of the sacrifices they have made throughout my life.

February 2019

Tianguo Deng

Award

1. **Young Scientist Award**, 4th Asian School-Conference on Physics and Technology of Nanostructured Materials (ASCO-NANOMAT), Vladivostok, Russia, Sept. 24, 2018.

List of publications

1. **T. Deng**, T. Sato, Z. Xu, R. Takabe, S. Yachi, Y. Yamashita, K. Toko, and T. Suemasu,
"p-$BaSi_2$/n-Si heterojunction solar cells on Si(001) with conversion efficiency approaching 10%: comparison with Si(111),"
Applied Physics Express **11** (2018) 062301.

2. **T. Deng**, T. Suemasu, D. A. Shohonov, I. S. Samusevich, A. B. Filonov, D. B. Migas, and V. E. Borisenko,
"Transport properties of n- and p-type polycrystalline $BaSi_2$,"
Thin Solid Films **661** (2018) 7.

3. **T. Deng**, K. Gotoh, R. Takabe, Z. Xu, S. Yachi, Y. Yamashita, K. Toko, N. Usami, and T. Suemasu,
"Boron-doped p-$BaSi_2$/n-Si solar cells formed on textured n-Si(001) with a pyramid structure consisting of {111} facets,"
Journal of Crystal Growth **475** (2017) 186.

4. R. Takabe, **T. Deng**, K. Kodama, Y. Yamashita, T. Sato, K. Toko, and T. Suemasu,
"Impact of Ba to Si deposition rate ratios during molecular beam epitaxy on carrier concentration and spectral response of $BaSi_2$ epitaxial film,"
Journal of Applied Physics **123** (2018) 045703.

5. S. Yachi, R. Takabe, **T. Deng**, K. Toko, and T. Suemasu,
"Effect of $BaSi_2$ template growth duration on the generation of defects and performance of p-$BaSi_2$/n-Si heterojunction solar cells,"
Japanese Journal of Applied Physics **57**(2018) 042301.

6. K. Kodama, R. Takabe, **T. Deng**, K. Toko, and T. Suemasu,
"Spectroscopic evidence of photogenerated carrier separation by built-in electric field in Sb-doped n-$BaSi_2$/B-doped p-$BaSi_2$ homojunction diodes,"
Japanese Journal of Applied Physics **57** (2018) 050310**.**

7. Z. Xu, K. Gotoh, **T. Deng**, T. Sato, R. Takabe, K. Toko, N. Usami, and T. Suemasu,
"Improving the photoresponse spectra of BaSi2 layers by capping with hydrogenated amorphous Si layers prepared by radio-frequency hydrogen plasma,"
AIP Advances **8** (2018) 055306.

8. Z. Xu, **T. Deng**, R. Takabe, K. Toko, and T. Suemasu,
"Fabrication and characterizations of nitrogen-doped $BaSi_2$ epitaxial films grown by molecular beam epitaxy,"
Journal of Crystal Growth **471** (2017) 37.

List of conferences

a. International conferences

1. (**Oral**) **T. Deng**, T. Sato, Z. Xu, R. Takabe, S. Yachi, Y. Yamashita, K. Toko and T. Suemasu,
"Towards $BaSi_2$ homojunction solar cells on Si(001),"
4th International Asian School Conference on Physics and Technology of Nanostructured Materials (ASCO-NANOMAT 2018), III.24.01o, Vladivostok, Russia, Sept. 24, 2018.
Young Scientist Award.

2. (**Oral**) **T. Deng**, Z. Xu, Y. Yamashita, K. Kodama, T. Sato, K. Toko and T. Suemasu,
"Investigation of $BaSi_2$ homojunction solar cells on a p^+-$BaSi_2$/p^+-Si tunnel junction towards $BaSi_2$/Si tandem solar cells"
2018 International Conference on Solid State Devices and Materials (SSDM 2018), F-5-03, Tokyo, Japan, Sept. 12, 2018.

3. (**Poster**) **T. Deng**, T. Sato, Z. Xu, R. Takabe, S. Yachi, Y. Yamashita, K. Toko and T. Suemasu,
"Investigation of p-$BaSi_2$/n-Si heterojunction solar cells on Si(001) and comparison to those on Si(111),"
7th World Conference on Photovoltaic Energy Conversion (WCPEC-7), A7-572, Hawaii, USA, June 13 (2018).

4. (**Poster**) **T. Deng**, G. Gotoh, R. Takabe, Z. Xu, S. Yachi, Y. Yamashita, K. Toko, N. Usami and T. Suemasu,
"Investigation on boron-doped p-$BaSi_2$/n-Si hetero-junction solar cells on a textured Si(001) substrate,"
27th International Photovoltaic Science and Engineering Conference (PVSEC-27), 2TuPo.75, Shiga, Japan, Nov. 14, 2017.

b. Domestic conference

1. (**Oral**) **T. Deng**, Z. Xu, Y. Yamashita, K. Kodama,K. Toko, T. Suemasu,
"Potential of $BaSi_2$ homojunction solar cells on a p^+-$BaSi_2$/p^+-Si tunnel junction,"
第79回応用物理学会秋季学術講演会 19p-436-2, 名古屋, September 19 (2018)

2. (**Poster**) **T. Deng**, Z. Xu, Y. Yamashita, K. Kodama, K. Toko and T. Suemasu ,
"Potential of $BaSi_2$ homojunction solar cells on Si(001) substrate,"
第14回「次世代の太陽光発電システム」シンポジウム PB-37, 札幌, July 12 (2018).

3. (**Oral**) **T. Deng**, T. Sato, Z. Xu, R. Takabe, S. Yachi, Y. Yamashita, K. Toko, T. Suemasu,
"Investigation on p-$BaSi_2$/n-Si heterojunction solar cells using a Si(001) substrate,"
第65回応用物理学会春季学術講演会 19a-F202-1, 東京, March 19 (2018).

4. (**Poster**) **T. Deng**, Z. Xu, R. Takabe, S. Yachi, M. B. Emha, K. Toko, T. Suemasu,
"Carrier transport properties of boron-doped p-$BaSi_2$ on Si(111) and Si(001),"
第78回応用物理学会秋季学術講演会 7P-PB4-10, 福岡, September 7 (2017).

5. (**Oral**) **T. Deng**, G. Gotoh, R. Takabe, S. Yachi, Z. Xu, M. B. Emha, K. Toko, N. Usami, T. Suemasu,
"Boron-doped p-$BaSi_2$/n-Si solar cells formed on textured n-Si(001) with a pyramid structure consisting of (111) facets,"
第64回応用物理学会春季学術講演会 16a-B5-8 , 横浜, March 16 (2017).

6. (**Oral**) **T. Deng**, G. Gotoh, R. Takabe, S. Yachi, Z. Xu, M. B. Emha, K. Toko, N. Usami, T. Suemasu,
"Characterization of undoped-$BaSi_2$ and Boron-doped $BaSi_2$ on textured Si (001) substrate grown by molecular beam epitaxy,"
第77回応用物理学会秋季学術講演会 15a-B3-6 , 新潟, September 15 (2016).

7. (**Poster**) **T. Deng**, R. Takabe, K. Toko, N. Usami and T. Suemasu,
"Characterization of undoped-$BaSi_2$ on textured Si(001) substrate grown by molecular beam epitaxy,"
International Symposium on Optical Communications 2016, P3-31, 富士,August 8–10, 2016.